# Strongly correlated systems

by

Łukasz Cincio

**DISSERTATION**

Submitted in Partial Fulfillment

of the Requirements for the Degree of

DOCTOR OF PHILOSOPHY

in the

MARIAN SMOLUCHOWSKI INSTITUTE OF PHYSICS

of the

JAGIELLONIAN UNIVERSITY IN KRAKÓW

Dr hab. Jacek Dziarmaga, prof. UJ, Supervisor

2010

# Contents

# Acknowledgments

First and foremost, I owe my deepest gratitude to my supervisor, dr hab. Jacek Dziarmaga, prof. UJ for all the hope he has put on me throughout my PhD studies. I am very grateful for his support and assistance during my MSc and PhD studies as well as when writing this dissertation. He has taught me how good theoretical physics is done and how to appreciate and cooperate with other scientists effectively and efficiently as well as take the most of their expertise and experience. Moreover, I particularly appreciate that our relations have always been based on partnership.

I also thank prof. Guifre Vidal from the University of Queensland, Brisbane, who gave me a unique chance to work with him as well as talented and full of passion members of his group. I am honored that I have had the opportunity to learn from Guifre's broad specialist knowledge in the atmosphere of friendship and encouragement.

I would also like to acknowledge prof. Maciej Lewenstein from ICFO, Barcelona, for a possibility of visiting him and collaborating with his group twice. I could gain a lot of experience and have learnt a lot during my stays as well as in Poland, when working on our common project.

Next, I would like to thank my colleague, Marek M. Rams, member of Jacek's group, for invaluable discussions and exchange of information and materials on all the projects we have been engaged in.

Finally, I would like to express special thanks to my beloved wife – Ola, for her love, faithful support, patience and time devoted to my scientific work as well as this dissertation.

# Chapter 1

# Introduction

The so-called strongly correlated systems are one of the most interesting and at the same time most difficult phenomena to describe. Here, the interactions between individual parts of the system are of fundamental importance to the behavior of the whole system. These interactions are responsible for serious theoretical problems as well as computational obstacles in the case of most methods of description that are known at present.

In most cases, the above-mentioned interactions are strong enough to create entanglement between the parts of the system giving rise to the phenomena such as high-$T_c$ superconductors, quantum phase transitions and fractional quantum Hall effect.

Therefore, the main objective of this Dissertation involves developing and applying powerful tools with a view to examining the phenomena of strongly correlated systems.

Strongly correlated systems have been in focus of research for a long time. Due to the progress in the computer-aided numerical methods, simulations of such systems have recently become an useful technique of research. The first step in this field is due to White [36], who proposed a density matrix renormalization group algorithm (DMRG). This algorithm has been a breakthrough and become an important tool in investigating one-dimensional quantum systems.

The quantum information theory which was developing rapidly at that time gave rise to a number of tools which made it possible for effective calculations to be carried out in quantum many-body systems. This progress has facilitated the establishment of new research techniques in Quantum Physics. One of such tools has been proposed by Vidal [31, 32, 33] in his recent articles. Vidal proposes an improved version of the DMRG algorithm according to which proper decomposition into two parts of the quantum state on one-dimensional lattice is implemented.

It turns out that for a ground state of typical Hamiltonian, coefficients of this decomposition decay exponentially. This property is well satisfied outside the critical point. The exponential decay of these coefficients suggests approximate and effective description of the quantum state: in order to obtain such description, one should keep only a small number $m$ of the largest coefficients. In [4], we use this algorithm to investigate the dynamics of quantum phase transitions in one-dimensional quantum Ising model.

Algorithms of this kind are based on a certain representation of the quantum state known as matrix product state (MPS). In this method, each spin $S$ is assigned $2S + 1$

matrices of size $m \times m$. MPS can be naturally generalized to higher dimensions. The generalization of MPS to higher dimensions boils down to replace the matrices by higher dimensional tensors in order to take larger number of nearest neighbors on a lattice into account. These states can also be obtained as projected entangled pair states (PEPS). It occurs that in this representation, it is convenient to prove that every quantum state can be accurately described by way of PEPS for sufficiently large dimension $m$.

Despite undeniable benefits, MPS and its generalizations confront some technical obstacles. The time, which is required to make all calculations within these algorithms, scales polynomially in dimension $m$. In one-dimensional setting, the degree of polynomial is small enough to carry out computations for large values of $m$. However, this degree becomes large in two dimensions. As a result, the calculations may become time-consuming and it might be difficult to go to higher dimension $m$. Unfortunately, in many intriguing situations, it may turn out that large dimension $m$ is required to obtain accurate results.

A refreshingly new idea of multi-scale entanglement renormalization Ansatz (MERA), which is tailored for the description of quantum critical points, seems to be a workable and cost-effective solution to this problem [34]. Using the example of one-dimensional quantum Ising model in the critical point, it has been established that it is possible to reduce the necessary dimension $m$ by orders of magnitude without any loss of accuracy in comparison with the standard DMRG. This astonishing improvement in the performance has been achieved thanks to the proper removal (renormalization) of short-range entanglement in the system. The effectiveness of this new algorithm consists in the fact that the calculations remain polynomial in dimension $m$ and it needs emphasizing that this dimension does not have to increase along with a growth of the system size, as in the case of the DMRG algorithms.

There are many possible realizations of the geometry of MERA. Given a physical model, it is possible to select the most adequate and effective one. The geometries differ from each other in the amount of entanglement they remove and in the way the calculations scale with dimension $m$. In [15], another example of the two-dimensional geometry was introduced with the aim to solve quantum Ising model defined on large and even infinite systems.

MERA has also been applied to study the geometrically frustrated antiferromagnet. In this approach, the properties of the ground state of spin-$\frac{1}{2}$ Heisenberg model on kagome lattice are investigated in detail [17]. Special attention has to be paid to the recent applications of MERA to the fermionic systems, which play a fundamental role in our understanding of condensed matter phenomena [9]. In contrast to the Quantum Monte Carlo techniques, which break down in the fermionic models due to a negative sign problem, MERA is fully capable of describing such systems. Whereas there are fundamental physical differences between bosonic and fermionic models, there are no significant ones in the structure of MERA in both cases. Test calculations have been performed in free and interacting fermionic systems which positively verified the applicability of the new Ansatz [10].

The ability to make effective and accurate calculations at zero temperature for two-

dimensional systems is of fundamental importance for our comprehension of strongly correlated quantum systems which are defined on two-dimensional lattices. It suffices to mention possible applications of high-$T_c$ superconductors which effectively turn out to be two-dimensional, strongly correlated systems of electrons on the lattice. In order to describe the electrons, Hubbard model [19] is used, however, it has not been solved so far in spite of long-lasting and labor-intensive works on the subject. It is not even known yet, if this model predicts superconductivity.

The MERA algorithm is a new numerical approach which in the scientific community is perceived as a fascinating and crucial breakthrough in analyzing the properties of extended quantum systems. The area of its applications has been significantly extended after recognizing that this approach is free of the fermionic negative sign problem [9, 10], which is a major obstacle in other quantum-mechanical techniques.

Although the approach is relatively fresh, it brings very promising and problem-solving results which is encouraging to carry out further and in-depth research. The algorithm develops other well-known approaches in an innovative way by means of supplementing it with novel and stimulating ideas. It can be safely said that progress in works on this algorithm is a vital step towards understanding and solving problems in condensed matter physics.

This Dissertation is organized as follows. Chapter 2 provides an overview of the MERA algorithm. For simplification, the reasoning included there is carried out for one-dimensional quantum systems. The content involves an apt description of two components that the algorithm is built of: isometries and disentanglers. This description is accompanied by illustrative examples. The remaining part of the chapter is devoted to an analysis of MERA properties together with some hints on the more technical issues which stem from our experience with MERA. We conclude with providing details of the MERA optimizing procedures aimed at obtaining the ground state description which are applied in the following chapters.

In the next chapter, we show how MERA can be naturally generalized to higher dimensions. We examine one of its possible generalizations by obtaining the ground state of two-dimensional quantum Ising model on a small square lattice, but already outside the scope of exact diagonalization. We verify that surprisingly accurate results can be obtained even with the smallest non-trivial dimension $m$.

In Chapter 4, we show that the modified MERA schemes may be applied to investigate interesting physical systems. They are used to make calculations in the two-dimensional generalized quantum compass model on an infinite square lattice. We take a close look at the quantum phase transition between Ising-like ground state and anisotropic one of the generalized compass model. The MERA algorithm allows us to demonstrate that the transition under examination is of the second order and it takes place very close to the compass model where quantum fluctuations are sufficiently large to break the symmetry. The results presented in Chapters 3 and 4 are based on [5, 6].

The last Chapter develops the notion of another variation of MERA algorithm: finite-range MERA. We begin with discussing its major feature according to which finite-range

MERA is capable of addressing directly the infinite systems at low cost. Next, we discuss the possible area of implementation of an even simpler scheme, namely, finite-range MERA consisting of only one layer of tensors. After that, we provide instances of its application to two frustrated quantum systems. The material presented in this chapter is the subject of evolving research [7, 8].

# Chapter 2

# The MERA algorithm

Since the MERA algorithm is easier to describe by means of graphical representations, we begin with establishing a formal correspondence between algebraic objects and their graphical representations.

## 2.1 Tensors and their graphical representation

In this Dissertation, we consider tensors as linear mappings between two (finitely dimensional) Hilbert spaces:

$$t \colon \mathbb{V}_1 \to \mathbb{V}_2, \tag{2.1}$$

where $\mathbb{V}_1$ and $\mathbb{V}_2$ stand for tensor products of some given number of spaces $\mathbb{C}^k$:

$$\mathbb{V}_1 \;=\; \mathbb{C}^{n_1} \otimes \cdots \otimes \mathbb{C}^{n_N}, \quad \mathbb{V}_2 \;=\; \mathbb{C}^{m_1} \otimes \cdots \otimes \mathbb{C}^{m_M}. \tag{2.2}$$

We then say that tensor $t$ has $N$ input and $M$ output wires (or indices). As a linear map, $t$ is fully represented by a set of $n_1 \cdot \ldots \cdot n_N \cdot m_1 \cdot \ldots \cdot m_M$ complex numbers which can be naturally arranged into a multidimensional array:

$$t \left| i_1 \ldots i_N \right\rangle \;=\; \sum_{j_1=0}^{m_1-1} \cdots \sum_{j_M=0}^{m_M-1} t^{i_1 \ldots i_N}_{j_1 \ldots j_M} \left| j_1 \ldots j_M \right\rangle, \tag{2.3}$$

where $\{|k\rangle\}_{k=0}^{n-1}$ forms a basis of $\mathbb{C}^n$.

Because of the specific structure of spaces $\mathbb{V}_1$ and $\mathbb{V}_2$ in (2.2), there exists a useful graphical representation of tensors. Fig. 2.1(a) shows an example of such a representation for $N = 2$ and $M = 3$.

To avoid ambiguity, we set the following rule of drawing tensor representations: Upper wires correspond to spaces $\mathbb{C}^k$ in a domain whereas lower ones – to spaces in a range of a tensor. The wires are arranged in exactly the same sequence as their corresponding spaces, i.e. from left to right.

Tensors undergo all standard linear operations: addition, multiplication by scalar and composition. However, thanks to the tensorial character of spaces $\mathbb{V}_1$ and $\mathbb{V}_2$ in (2.2), we can extend the definition of composition for linear mappings and consider general tensor contractions. In general, every two wires of one or two tensors can be contracted if their corresponding Hilbert spaces have the same dimension.
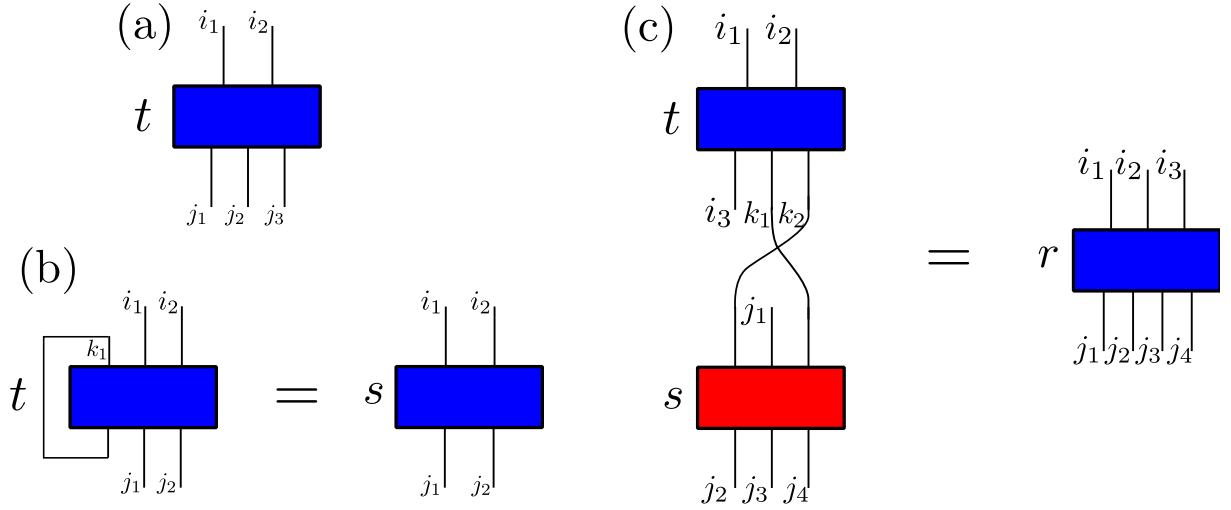
Figure 2.1: (a) Graphical representation of tensor $t\colon \mathbb{C}^{n_1} \otimes \mathbb{C}^{n_2} \to \mathbb{C}^{m_1} \otimes \mathbb{C}^{m_2} \otimes \mathbb{C}^{m_3}$. Tensor $t$ has two input and three output wires with elements: $t^{i_1 i_2}_{j_1 j_2 j_3}$. (b) Example of contraction of two wires which belong to the same tensor (partial trace). (c) General contraction of two tensors. The application of the rule of ordering wires of tensor $r$.

Fig. 2.1(b) serves as an example of contraction in a special case when both wires belong to the same tensor. In algebraic notation, this operation can be written as follows:

$$t\colon \mathbb{C}^{n_1} \otimes \mathbb{C}^{n_2} \otimes \mathbb{C}^{n_3} \to \mathbb{C}^{m_1} \otimes \mathbb{C}^{m_2} \otimes \mathbb{C}^{m_3}, \quad s\colon \mathbb{C}^{n_2} \otimes \mathbb{C}^{n_3} \to \mathbb{C}^{m_2} \otimes \mathbb{C}^{m_3}, \tag{2.4}$$

where $n_1 = m_1$. The elements of tensor $s$ read:

$$s^{i_1 i_2}_{j_1 j_2} = \sum_{k_1=0}^{n_1-1} t^{k_1 i_1 i_2}_{k_1 j_1 j_2}. \tag{2.5}$$

In literature, this operation is referred to as a partial trace.

Fig. 2.1(c) provides another instance of tensor contraction. In this case, four wires are contracted, two of them belong to tensor $t$. Note that some of the output wires of $t$ as well as input wires of $s$ are not contracted. Due to this, we set a second rule of manipulating tensor representations: All wires of tensor $t$ that are not contracted become input wires of the resulting tensor $r$. These wires are ordered in the same way as they are in the case of tensor $t$. Additionally, the input wires of $t$ are placed at the beginning. Similarly, all the remaining wires of $s$ turn into output wires of $r$ by means of the same method of ordering as input wires of $r$.

Algebraically, the contraction presented in Fig. 2.1(c) is as follows:

$$t\colon \mathbb{C}^{n_1} \otimes \mathbb{C}^{n_2} \to \mathbb{C}^{m_1} \otimes \mathbb{C}^{m_2} \otimes \mathbb{C}^{m_3}, \quad s\colon \mathbb{C}^{n'_1} \otimes \mathbb{C}^{n'_2} \otimes \mathbb{C}^{n'_3} \to \mathbb{C}^{m'_1} \otimes \mathbb{C}^{m'_2} \otimes \mathbb{C}^{m'_3},$$
$$r\colon \mathbb{C}^{n_1} \otimes \mathbb{C}^{n_2} \otimes \mathbb{C}^{m_1} \to \mathbb{C}^{n'_2} \otimes \mathbb{C}^{m'_1} \otimes \mathbb{C}^{m'_2} \otimes \mathbb{C}^{m'_3}, \tag{2.6}$$

where $n'_1 = m_3$ and $n'_3 = m_2$. The elements of tensor $r$ are such that:

$$r^{i_1 i_2 i_3}_{j_1 j_2 j_3 j_4} = \sum_{k_1=0}^{m_2-1} \sum_{k_2=0}^{m_3-1} t^{i_1 i_2}_{i_3 k_1 k_2}\, s^{k_2 j_1 k_1}_{j_2 j_3 j_4}. \tag{2.7}$$

## 2.2 Contraction of tensors – implementation details

It turns out that contraction of two tensors is the basic procedure that is constantly repeated in the MERA algorithm. That is why, from a technical point of view, it is important to implement tensor contraction as efficiently as possible.

In this section, we examine various approaches to programming contraction of tensors. Let us focus on the example provided in Fig. 2.1(c).

Firstly, the simplest approach to programming this contraction involves direct implementation of Eq. (2.7) by means of a nested loop construction. In this case, seven external loops are used to address all the elements of final tensor $r$ and two internal loops in order to perform summation over indices $k_1$ and $k_2$. Although this method is conceptually simple and easy to program, it proves to be inefficient, especially when high dimensions of individual spaces $\mathbb{C}^n$ are involved.

In the second approach, matrix multiplication is used to calculate the elements of final tensor $r$. This is carried out in three steps:

(i) Reshaping initial tensors $t$ and $s$ into matrices $M_t$ and $M_s$, respectively;

(ii) Performing matrix multiplication of $M_t$ and $M_s$ to obtain matrix $M_r$; and

(iii) Reshaping matrix $M_r$ into the final tensor $r$.

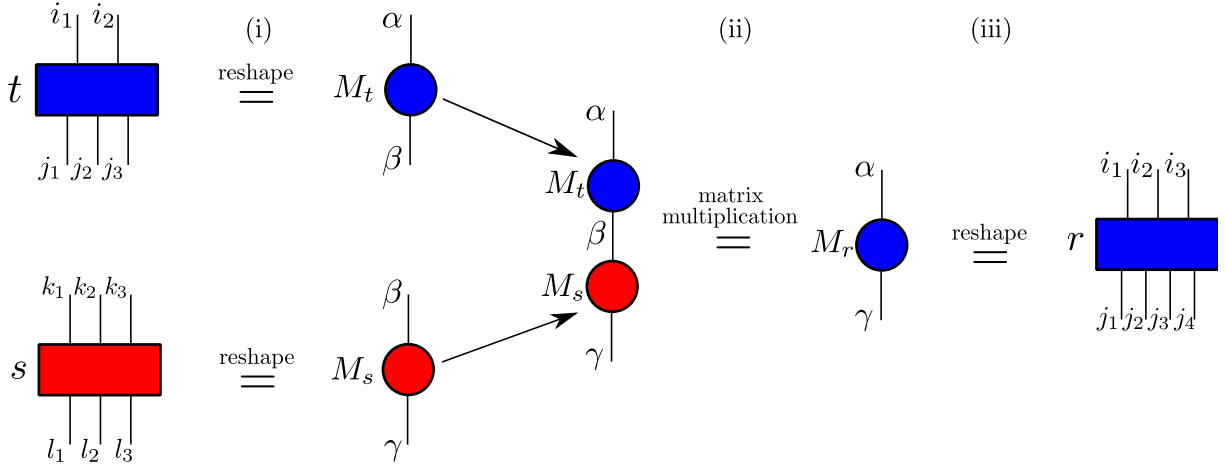This procedure is shown in Fig. 2.2.



Figure 2.2: Method of contracting tensors based on the matrix multiplication. Contraction is conducted in three steps: (i) reshaping $t$ and $s$ into $M_t$ and $M_s$, respectively, (ii) multiplication $M_r = M_t M_s$ and (iii) reshaping $M_r$ into $r$.

Let us analyze each step of this procedure in more detail.

(i) All wires of tensor $t$ that are not contracted are grouped into one index $\alpha$ of matrix $M_t$. These wires will become the input ones of the final tensor $r$. The remaining wires of $t$ will be contracted – they are grouped into one index $\beta$ of matrix $M_t$

(compare Fig. 2.2 with Fig. 2.1(c)). According to the rules of manipulating tensor representations, the construction of matrix $M_t \in \mathcal{M}(n_1 n_2 m_1, m_2 m_3)$ is as follows:

$$(M_t)^\alpha_\beta = t^{i_1 i_2}_{j_1 j_2 j_3} , \quad \text{where}$$
$$\alpha = [i_1, i_2, j_1] = i_1 + i_2 \cdot n_1 + j_1 \cdot n_1 n_2 , \tag{2.8}$$
$$\beta = [j_3, j_2] = j_3 + j_2 \cdot m_3 .$$

The construction of matrix $M_s \in \mathcal{M}(m_2 m_3, n'_2 m'_1 m'_2 m'_3)$ corresponding to tensor $s$ is performed in a similar way:

$$(M_s)^\beta_\gamma = s^{k_1 k_2 k_3}_{l_1 l_2 l_3} , \quad \text{where}$$
$$\beta = [k_1, k_3] = k_1 + (k_3 - 1) \cdot m_3 , \tag{2.9}$$
$$\gamma = [k_2, l_1, l_2, l_3] = k_2 + l_1 \cdot n'_2 + l_2 \cdot n'_2 m'_1 + l_3 \cdot n'_2 m'_1 m'_2 .$$

(ii) Matrices $M_t$ and $M_s$ are multiplied. In this step, the actual tensor contraction takes place:

$$M_r = M_t M_s . \tag{2.10}$$

(iii) Indices $\alpha$ and $\gamma$ of matrix $M_r \in \mathcal{M}(n_1 n_2 m_1, n'_2 m'_1 m'_2 m'_3)$ shown in Fig. 2.2 are ungrouped in order to form input and output wires of a final tensor $r$, respectively. Elements of tensor $r$ are restored in a following way:

$$r^{i_1 i_2 i_3}_{j_1 j_2 j_3 j_4} = (M_r)^\alpha_\gamma , \quad \text{where}$$
$$\alpha = [i_1, i_2, i_3] = i_1 + i_2 \cdot n_1 + i_3 \cdot n_1 n_2 , \tag{2.11}$$
$$\gamma = [j_1, j_2, j_3, j_4] = j_1 + j_2 \cdot n'_2 + j_3 \cdot n'_2 m'_1 + j_4 \cdot n'_2 m'_1 m'_2 .$$

In the majority of applications, a list of tensors are contracted in a sequence in such a way that a tensor, which is a result of given contraction, is immediately used in a subsequent one as an initial tensor. In this case, steps (iii) and (i) from the consecutive contractions can be merged into one step to avoid unnecessary tensor reshaping.

Contraction of tensors based on matrix multiplication proves to be more efficient than the simplest one resulting from the direct use of Eq. (2.7). The reason for this is the ability to use highly optimized libraries for matrix multiplication that considerably outperforms direct contraction based on Eq. (2.7). What is more, in this approach, it may be verified that additional reshaping steps have only small contribution to overall time that is spent on tensor contraction.

The graphical representation of tensors and their contraction allows us to almost completely resign from algebraic expressions. Sometimes, however, we use a shortened algebraic notation. By writing $ts = r$, we refer to a special case of tensor contraction in which all output wires of tensor $s$ are contracted with all input wires of $t$ without permutation of indices. In any other case, we use central dot $\cdot$ to denote tensor contraction, e.g. $\mathcal{E}_u = t_2 \cdot r_7$. Notice that the notation is ambiguos, it can be used only in situations when we are not interested in details of the contraction.

## 2.3 Basics of the MERA algorithm. Role of isometries and disentanglers

Entanglement renormalization has been developed by Vidal [34] on the basis of standard renormalization techniques proposed by Kadanov [20] and Wilson [37]. In order to understand better how Vidal's idea of disentanglers contributes to the previous proposal, let us first examine the standard renormalization procedure in the language of isometric tensors.

### 2.3.1 Isometries

The method of renormalization group is established on the idea of grouping spins in larger blocks and truncating Hilbert space in which this block is described in order to eliminate all redundant degrees of freedom.

The spin grouping and Hilbert space truncation may be described by an isometric tensor $w$:

$$w \colon \mathbb{C}^m \to \mathbb{C}^{n_1} \otimes \mathbb{C}^{n_2} \ , \quad w^\dagger w = \mathbb{I}_{\mathbb{C}^m} \ , \tag{2.12}$$

where product $\mathbb{C}^{n_1} \otimes \mathbb{C}^{n_2}$ is a physical space of two particles with spins $S_1$ and $S_2$, where $n_1 = 2S_1 + 1$ and $n_2 = 2S_2 + 1$. Effective block spin $S'$ is represented in space $\mathbb{C}^m$. The graphical representation of isometry $w$ is depicted in Fig. 2.3(a).

Tensor $w^\dagger$ acts on the state of two particles and builds one effective block spin. Note that in the case of $m = n_1 n_2$, the mapping given by tensor $w^\dagger$ is exact, whereas some information about initial state may be lost when $m < n_1 n_2$.

If properly expanded on all spins of the chain, this operation causes the so-called coarse graining of the initial state (see Fig. 2.3(c)).

In this renormalization technique, the dimension $m$ of the target space of tensor $w^\dagger$ is the key parameter. On the one hand, it should be reasonably small since the cost of computation of expected values of observables scales polynomially with this dimension. On the other, it should be sufficiently large as it is desirable to have



Figure 2.3: (a) Graphical representation of isometry $w$ in Eq. (2.12). (b) Condition of isometry for tensor $w$. (c) Initial state $|\psi\rangle$ on 8 spins is coarse-grained into effective state $|\psi'\rangle$ on 4 block spins by means of the product of isometries $w_1 \otimes \cdots \otimes w_4$.

accurate description of a given state. We see, that a careful choice of tensor $w$ as well as dimension $m$ is essential.

In [36], White suggests to analyze the reduced density matrix for two spins $[s_1 s_2]$ that are going to be grouped into one block spin $s'$. The reduced density matrix is hermitian
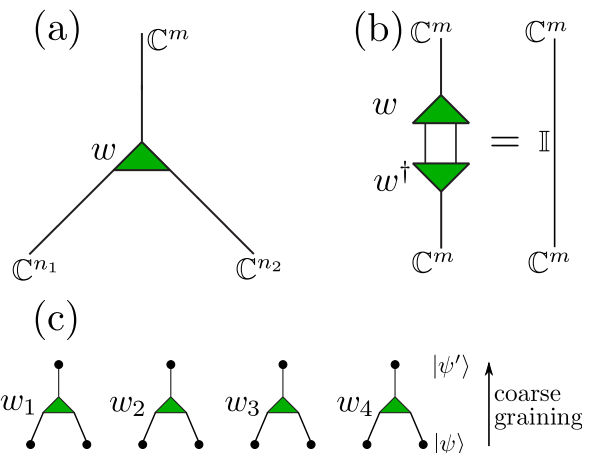
and its trace equals one, thus, it can always be written in a diagonal form with decreasing eigenvalues:

$$\rho^{[s_1 s_2]} = \sum_{i=0}^{n_1 n_2 - 1} p_i \, |\rho_i\rangle\langle\rho_i| \; , \quad \text{where}$$

(2.13)

$$1 \geq p_0 \geq p_1 \geq \cdots \geq p_{n_1 n_2 - 1} \geq 0 \quad \text{and} \sum_{i=0}^{n_1 n_2 - 1} p_i = 1 \; .$$

Following White, the optimal choice of dimension $m$ of the target space of tensor $w^\dagger$ is as follows: Let $\varepsilon \ll 1$ be an truncation error. Parameter $m$ is then the smallest number which satisfies inequality:

$$1 - \sum_{i=0}^{m-1} p_i \; \leq \; \varepsilon \; .$$

(2.14)

For every $i \in \{0, 1, \ldots, m - 1\}$, vector $w^i$ is selected so as to be the $i$-th eigenstate of reduced density matrix $\rho$:

$$w_{j_1 j_2}^i = \langle j_1 j_2 | \rho_i \rangle \; .$$

(2.15)

Intuitively, during the above-mentioned procedure, only the most important part of the description of the initial state is kept. The rest of them, redundant or unimportant degrees of freedom, are neglected.

In other words, the full space for two spins $\mathbb{C}^{n_1} \otimes \mathbb{C}^{n_2}$ is truncated in such a way that $n_1 n_2 - m$ directions which correspond to eigenvectors of $\rho^{[s_1 s_2]}$ to the smallest eigenvalues are eliminated.

Let us now consider the following example to illustrate the method of selecting tensor $w$ and dimension $m$. Suppose that the system consists of four spin-$\frac{1}{2}$ particles $[e_1 s_1 s_2 e_2]$ arranged in a chain and that, during the renormalization step, two spins $[s_1 s_2]$ are going to be grouped into one effective block spin $s'$ as shown in Fig. 2.4. The previous, general approach is thus reduced to the case: $n_1 = n_2 = 2$. Let $\rho^{[e_1 s_1 s_2 e_2]} = |\psi\rangle\langle\psi|$ be the density matrix of the system, where:

$$|\psi\rangle = \sum_{k_1, \ldots, k_4 = 0}^{1} \psi_{k_1 k_2 k_3 k_4} \, |k_1 k_2 k_3 k_4\rangle$$

(2.16)

$$= \frac{1}{3} \left( 2 \, |1001\rangle + \sqrt{2} \, |0110\rangle - \sqrt{2} \, |1100\rangle + |0100\rangle \right) \; .$$

(2.17)

At first, we calculate the reduced density matrix for subsystem $[s_1 s_2]$ and write it in the diagonal form:

$$\rho^{[s_1 s_2]} = \text{Tr}_{e_1 e_2} \left[ \rho^{[e_1 s_1 s_2 e_2]} \right] = \sum_{i=0}^{3} p_i \, |\rho_i\rangle\langle\rho_i| \; , \quad \text{where}$$

(2.18)

$p_0 = p_1 = \frac{4}{9}$, $p_2 = \frac{1}{9}$, $p_3 = 0$ and

$$|\rho_0\rangle = \frac{2}{\sqrt{6}} \, |10\rangle + \frac{1}{\sqrt{3}} \, |11\rangle, \quad |\rho_1\rangle = |00\rangle,$$

$$|\rho_2\rangle = -\frac{1}{\sqrt{3}} \, |10\rangle + \frac{2}{\sqrt{6}} \, |11\rangle, \quad |\rho_3\rangle = |01\rangle \; .$$

(2.19)

Note that one of the eigenvalues of $\rho^{[s_1 s_2]}$ is zero and, therefore, direction $|\rho_3\rangle = |01\rangle$ can be removed from space $\mathbb{C}^2 \otimes \mathbb{C}^2$ without losing any information about the state of the system.
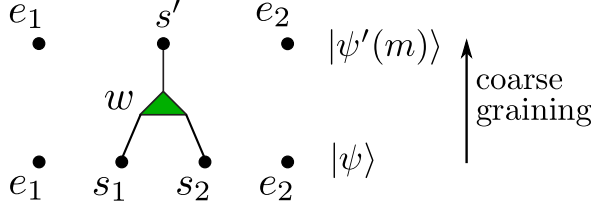


Figure 2.4: Example of coarse graining operation. State $|\psi\rangle$ is replaced with state $|\psi'(m)\rangle$. Choice of tensor $w$ and dimension $m$ is discussed in the text.

The second smallest eigenvalue of $\rho^{[s_1 s_2]}$ is $\frac{1}{9}$ and hence, in some rough approximation of the initial state, one could also eliminate direction $|\rho_2\rangle$ and choose $m = 2$. In this case, non-zero elements of tensor $w$ would be:

$$w^0_{10} = \frac{2}{\sqrt{6}} , \quad w^0_{11} = \frac{1}{\sqrt{3}} , \quad w^1_{00} = 1 . \tag{2.20}$$

In this example, an increase in dimension $m$ to 3 already gives the exact coarse graining. To achieve this, isometry $w$ needs to be extended by third vector $w^2$:

$$w^2_{10} = -\frac{1}{\sqrt{3}} , \quad w^2_{11} = \frac{2}{\sqrt{6}} . \tag{2.21}$$

During the coarse graining step, initial state $|\psi\rangle$ is replaced with the state $|\psi'(m)\rangle$ (compare with Fig. 2.4):

$$|\psi'(m)\rangle = \sum_{k_1, k_3 = 0}^{1} \sum_{k_2 = 0}^{m-1} \psi'(m)_{k_1 k_2 k_3} |k_1 k_2 k_3\rangle , \tag{2.22}$$

where:

$$\psi'(m)_{i_1 i_2 i_3} = \sum_{k_1, k_2 = 0}^{1} w^{i_2}_{k_1 k_2} \psi_{i_1 k_1 k_2 i_3} . \tag{2.23}$$

The explicit form of $|\psi'(m)\rangle$ for $m = 2$ and $m = 3$ is as follows:

$$|\psi'(m = 2)\rangle = \frac{4}{3\sqrt{6}} |000\rangle - \frac{2}{3\sqrt{3}} |100\rangle + \frac{2}{3} |111\rangle , \tag{2.24}$$

$$|\psi'(m = 3)\rangle = \frac{4}{3\sqrt{6}} |000\rangle - \frac{2}{3\sqrt{3}} |100\rangle + \frac{2}{3} |111\rangle + \frac{1}{3\sqrt{3}} |020\rangle + \frac{2}{3\sqrt{6}} |120\rangle . \tag{2.25}$$

### 2.3.2 Disentanglers

The effectiveness of the renormalization method studied in the previous section depends on the amount of entanglement between a group of spins that undergoes renormalization and the rest of the system. The more entanglement is involved, the larger space dimension $m$ has to be used in order to maintain accurate description. At the same time, large spaces negatively influence the efficiency of this algorithm which results in limiting the scope of application of this method.

In [34], Vidal proposes a variation of the standard renormalization procedure that provides a possible solution to this problem. His idea is astonishingly simple. As the entanglement poses an obstacle in truncating the space of effective spins, it is worth trying to reduce it before the actual truncation occurs. This reduction is achieved by means of carefully chosen unitary transformations that can affect the amount of entanglement between a given group of spins and the rest of the system.



Figure 2.5: (a) Disentangler $u_1$ defined in Eq. (2.26). (b) Unitary condition for tensor $u_1$. (c) Transformations $u_1$ and $u_2$ acts on the boundary of block $[s_1 s_2]$.

For simplicity reasons, let us now study this idea in detail in the special case of a one-dimensional lattice of spins (i.e. each spin has two nearest neighbors), where two spins $[s_1 s_2]$ will be grouped into one block spin at some point of the algorithm. We consider unitary operations $u_1$ and $u_2$, each of them acts on one spin in block $[s_1 s_2]$ and its nearest neighbor outside the block.
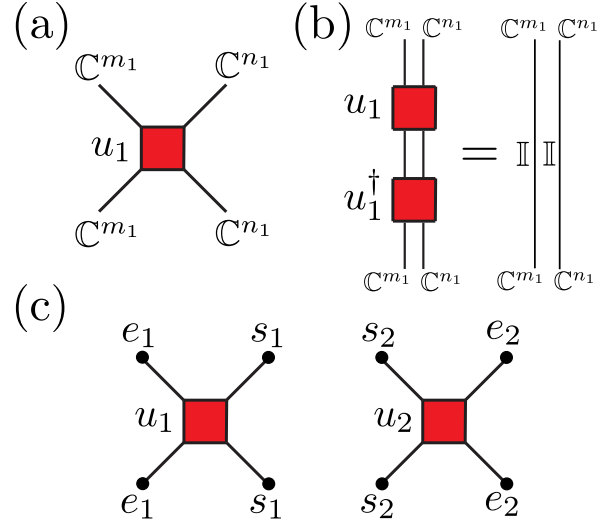
$$u_1 \colon \mathbb{C}^{m_1} \otimes \mathbb{C}^{n_1} \to \mathbb{C}^{m_1} \otimes \mathbb{C}^{n_1} \ , \quad u_1^\dagger u_1 = u_1 u_1^\dagger = \mathbb{I}_{\mathbb{C}^{m_1} \otimes \mathbb{C}^{n_1}}, \quad (2.26)$$

$$u_2 \colon \mathbb{C}^{n_2} \otimes \mathbb{C}^{m_2} \to \mathbb{C}^{n_2} \otimes \mathbb{C}^{m_2} \ , \quad u_2^\dagger u_2 = u_2 u_2^\dagger = \mathbb{I}_{\mathbb{C}^{n_2} \otimes \mathbb{C}^{m_2}} \ . \quad (2.27)$$

This situation is illustrated in Fig. 2.5.

Properly selected transformations $u_1$ and $u_2$ decrease the entanglement between block $[s_1 s_2]$ and its nearest neighbors on a lattice (spins $e_1$ and $e_2$ in Fig. 2.5(c)). As a consequence, the initial reduced density matrix for spins $[s_1 s_2]$:

$$\rho^{[s_1 s_2]} \;=\; \mathrm{Tr}_{e_1 e_2} \left[ \rho^{[e_1 s_1 s_2 e_2]} \right] \quad (2.28)$$

is replaced with $\widetilde{\rho}^{[s_1 s_2]}$ which is partially disentangled with nearest neighborhood on the lattice:

$$\widetilde{\rho}^{[s_1 s_2]} \;=\; \mathrm{Tr}_{e_1 e_2} \left[ (u_1 \otimes u_2) \rho^{[e_1 s_1 s_2 e_2]} (u_1 \otimes u_2)^\dagger \right] \ . \quad (2.29)$$

Transformations $u_1$ and $u_2$ are referred to as disentanglers because of their application – their aim is to (partially) disentangle block $[s_1 s_2]$ with the rest of the lattice.

As a result of combining the standard renormalization technique and the new idea of disentanglers, we obtain the following construction shown in Fig. 2.6. Firstly, the entanglement between block $[s_1 s_2]$ and the rest of the system is removed in order to, secondly, truncate the space $\mathbb{C}^{n_1} \otimes \mathbb{C}^{n_2}$ more effectively.

Without disentanglers, in order to achieve pre-established truncation error $\varepsilon$ while coarse-graining the block $[s_1 s_2]$, dimension $m$ is chosen based on Eqs. (2.13) and (2.14). Due to the presence of disentanglers $u_1$ and $u_2$, it is feasible to achieve the same truncation

error in a significantly smaller space of effective spin $\widetilde{s}$, i.e. writing partially disentangled state $\widetilde{\rho}^{[s_1 s_2]}$ in a diagonal form:

$$\widetilde{\rho}^{[s_1 s_2]} = \sum_{i=0}^{n_1 n_2 - 1} \widetilde{p}_i \, |\widetilde{\rho}_i\rangle\langle\widetilde{\rho}_i| \; , \quad \text{where}$$

$$1 \geq \widetilde{p}_0 \geq \widetilde{p}_1 \geq \cdots \geq \widetilde{p}_{n_1 n_2 - 1} \geq 0 \quad \text{and} \tag{2.30}$$

$$\sum_{i=0}^{n_1 n_2 - 1} \widetilde{p}_i \; = \; 1 \; ,$$

it is possible to find $\widetilde{m} < m$ that satisfies inequality:

$$1 - \sum_{i=0}^{\widetilde{m}-1} \widetilde{p}_i \; \leq \; \varepsilon \; . \tag{2.31}$$
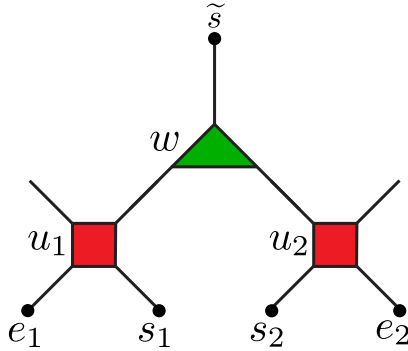


Figure 2.6: Decimation step of the new renormalization technique that is split into two steps: (i) disentangling and (ii) truncating the space.

This approach solves one of the basic problems of Wilson's renormalization which consists in that, with consecutive decimations, the dimension of constructed effective spaces grows rapidly. This feature may limit the applicability of this method only to small systems.

To demonstrate the effectiveness of disentanglers, let us now study the following example. As in the previous one, four spin-$\frac{1}{2}$ particles form the whole system $[e_1 s_1 s_2 e_2]$ and a group of two spins $[s_1 s_2]$ undergoes renormalization. This time, the state of the system is given by:

$$|\psi\rangle \; = \; \left[ \frac{1}{\sqrt{2}} (|01\rangle + |10\rangle) \right]^{\otimes 2} \; . \tag{2.32}$$

The reduced density matrix for subsystem $[s_1 s_2]$ takes the form:

$$\rho^{[s_1 s_2]} \; = \; \sum_{i=0}^{3} p_i \, |\rho_i\rangle\langle\rho_i| \; , \tag{2.33}$$

where $p_i = \frac{1}{4}$ for all $i \in \{0, 1, 2, 3\}$, which means that all directions $|\rho_i\rangle$ in the space $\mathbb{C}^2 \otimes \mathbb{C}^2$ are equally significant. This is the case of maximum amount of entanglement between group $[s_1 s_2]$ and the rest of the system. In this situation, it is not possible to truncate the space of an effective block spin without losing a considerable part of the initial state and thus, dimension $m$ needs to equal 4.

Consider now two unitary transformations $u_1 = u_2 = u$ that act on the state as shown in Fig. 2.6. Operation $u$ is selected in such a way that the state $(|01\rangle + |10\rangle)/\sqrt{2}$ is transformed into state $|00\rangle$. This can be made by the following choice of non-zero elements of $u$:

$$u_{01}^{00} \; = \; u_{10}^{00} \; = \; u_{01}^{01} \; = \; - u_{10}^{01} = \frac{1}{\sqrt{2}} \; ,$$

$$u_{00}^{10} \; = \; u_{11}^{11} \; = \; 1 \; . \tag{2.34}$$

16

Disentanglers $u$ transform $\rho^{[s_1 s_2]}$ into $\widetilde{\rho}^{[s_1 s_2]}$. Using Eq. (2.29), one obtains:

$$\widetilde{\rho}^{[s_1 s_2]} \;=\; \sum_{i=0}^{3} \widetilde{p}_i \, |\widetilde{\rho}_i\rangle\langle\widetilde{\rho}_i| \;, \tag{2.35}$$

where $\widetilde{p}_0 = 1$, $\widetilde{p}_1 = \widetilde{p}_2 = \widetilde{p}_3 = 0$ and $|\widetilde{\rho}_0\rangle = |00\rangle$. Since as many as 3 eigenvalues of $\widetilde{\rho}^{[s_1 s_2]}$ equal 0, the dimension of effective block spin $\widetilde{m}$ is trivial, i.e. $\widetilde{m} = 1$. Isometry $w$ that maps $[s_1 s_2]$ into $\widetilde{s}$ (see Fig. 2.6) is also trivial with one non-zero element: $w_{00}^0 = 1$.

The above example shows the extreme situation: proper use of disentanglers allows to decrease the dimension of an effective block spin from its maximal value $m = 4$ to minimal $\widetilde{m} = 1$.

## 2.4   MERA: Definition and properties

The construction of disentangling and truncating the Hilbert space presented in the previous section, naturally extends to larger spin chains. To this end, it suffices to provide additional layers of tensors, that is, after the first step of grouping spins into blocks, this operation is repeated for spin blocks.

Fig. 2.7 presents a network of tensors which describes a state on a chain consisting of 32 spins. Here we assume periodic boundary conditions, i.e. spins $s_2$ and $s_{32}$ are nearest neighbors of spin $s_1$ while spins $s_{31}$ and $s_1$ are nearest neighbors of $s_{32}$. For that reason, wires denoted by the same numbers on the right and left side in Fig. 2.7 are connected. Periodic boundary conditions naturally fit MERA algorithm. Although other types are also possible, they require far-reaching changes in the tensor network.
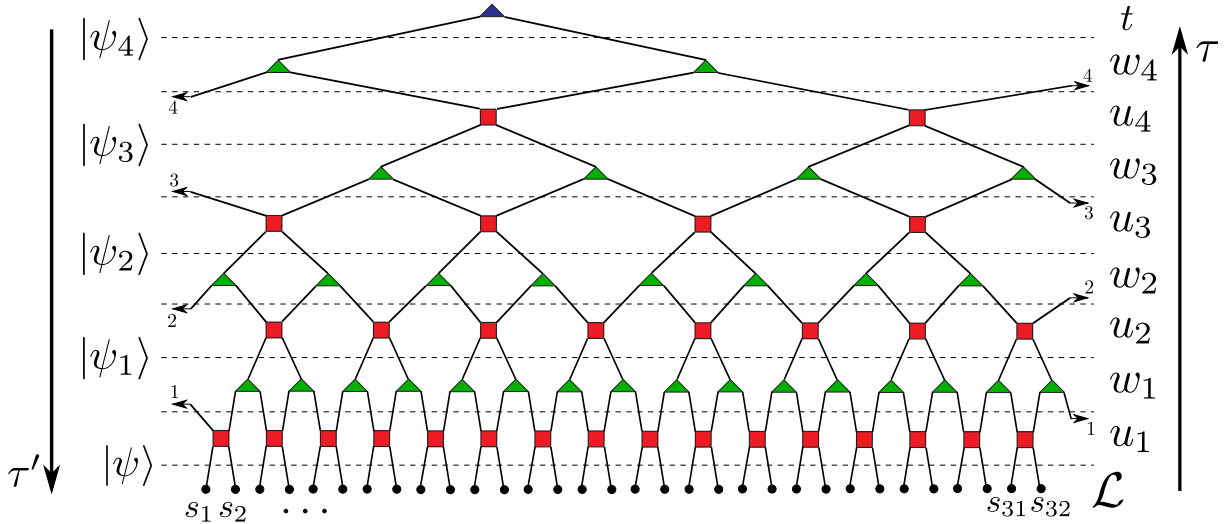


Figure 2.7: MERA for state $|\psi\rangle$ of 32 spins. Periodic boundary conditions are assumed – wires with the same numbers are connected. Arrows indicate two directions in which MERA scheme can be read: (i) as a renormalization technique: from bottom to top and (ii) as a quantum circuit: from top to bottom.

At the bottom of the network in Fig. 2.7, there is a chain $\mathcal{L}$ of 32 spins. The first layer of tensors involves disentanglers $u_1$, the following one – isometries $w_1$. These two

layers together map state $|\psi\rangle$ of 32 spins into the coarse-grained state $|\psi_1\rangle$ of 16 effective spins. The following layers carry out subsequent decimations which reduce the number of effective spins by half each time. After the last decimation, we get state $|\psi_4\rangle$ of two effective block spins which is directly specified by top tensor $t$. Top tensor is normalized as:

$$\sum_{k_1,k_2=0}^{m-1} t_{k_1 k_2} \left(t_{k_1 k_2}\right)^* = 1 . \tag{2.36}$$

The presented network of tensors $\{u_i, w_i\}_{i=1}^4$ together with top tensor $t$ are known as MERA for state $|\psi\rangle$. Although it may not be evident form Fig. 2.7, each layer does not have to involve the same tensors. For instance, the first layer of disentanglers may include 16 various tensors. It should also be noted that one can consider different dimensions of spaces in which effective block spins are described.

MERA can be seen from two different perspectives: as a renormalization algorithm and as a quantum circuit. Both of them are useful while studying MERA properties. According to the first point of view, the scheme in Fig. 2.7 is read from bottom to top. We start with a given state $|\psi\rangle$ and search for its best description in terms of tensors $\{u_i, w_i\}_{i=1}^4$ and top tensor $t$. At each layer, we choose dimensions of block spins and tensors $u_\tau$, $w_\tau$ according to the pre-established truncation error $\varepsilon$. In this approach, we obtain a sequence of coarse-grained states:

$$|\psi\rangle \equiv |\psi_0\rangle \xrightarrow{u_1^\dagger, w_1^\dagger} |\psi_1\rangle \xrightarrow{u_2^\dagger, w_2^\dagger} |\psi_2\rangle \xrightarrow{u_3^\dagger, w_3^\dagger} |\psi_3\rangle \xrightarrow{u_4^\dagger, w_4^\dagger} |\psi_4\rangle = t \tag{2.37}$$

defined on coarse-grained lattices:

$$\mathcal{L} \equiv \mathcal{L}_0 \xrightarrow{u_1^\dagger, w_1^\dagger} \mathcal{L}_1 \xrightarrow{u_2^\dagger, w_2^\dagger} \mathcal{L}_2 \xrightarrow{u_3^\dagger, w_3^\dagger} \mathcal{L}_3 \xrightarrow{u_4^\dagger, w_4^\dagger} \mathcal{L}_4 . \tag{2.38}$$

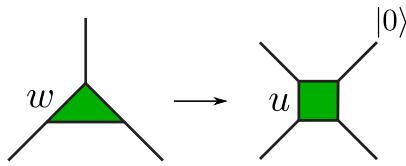Lattice $\mathcal{L}_\tau$ consists of $32 \cdot 2^{-\tau}$ effective spins.



Figure 2.8: MERA as a quantum circuit. In this approach, isometries are replaced with a unitary transformation with one input wire fixed.

In the second perspective, we treat MERA as a quantum circuit of unitary gates. This can be achieved by extending isometries $w$ to unitary transformations $u$:

$$w \colon \mathbb{C}^m \to \mathbb{C}^{n_1} \otimes \mathbb{C}^{n_2} ,$$
$$u \colon \mathbb{C}^m \otimes \mathbb{C}^{n_1 n_2/m} \to \mathbb{C}^{n_1} \otimes \mathbb{C}^{n_2} . \tag{2.39}$$

An additional input wire of tensor $u$ acts on fixed state $|0\rangle \in \mathbb{C}^{n_1 n_2/m}$ as shown in Fig. 2.8. Now, the scheme in Fig. 2.7 is read from top to bottom. Having all tensors in the network given, state $|\psi\rangle$ can be computed by means of subsequent actions of quantum gates in discrete time $\tau'$. During this process, a sequence of intermediate states $\{|\psi_{\tau'}\rangle\}_{\tau'}$ are calculated:

$$t = |\psi_4\rangle \xrightarrow{w_4, u_4} |\psi_3\rangle \xrightarrow{w_3, u_3} |\psi_2\rangle \xrightarrow{w_2, u_2} |\psi_1\rangle \xrightarrow{w_1, u_1} |\psi\rangle . \tag{2.40}$$

Apart from the similarities between Eqs. (2.37) and (2.40), one should be aware of fundamental differences between these two approaches. In the first one, state $|\psi\rangle$ is given

and MERA is constructed on this basis, while in the second one, MERA is given and state $|\psi\rangle$ is encoded.

Let us now scrutinize the MERA structure. One of its key features is the fact that the number of tensor layers scales logarithmically with the size of a lattice. In general, the number of tensors describing state $|\psi\rangle$ grows linearly with the size of the lattice. Thus, if $m$ denotes the dimension of each space in which consecutive block spins are described, then the number of parameters used to span the tensor network scales as $m^4 N$, where $N$ stands for the chain's length. Exponent 4 comes from the fact that the largest tensor in this structure – disentangler – has two input and two output wires.

Recall that in the exact standard description of the quantum state of a system of $N$ particles with spin $S$, one would need to specify $(2S+1)^N$ complex coefficients $\psi_{i_1 \dots i_N}$:

$$|\psi\rangle \;=\; \sum_{i_1,\dots,i_N=0}^{2S} \psi_{i_1 \dots i_N} |i_1 \dots i_N\rangle \; . \tag{2.41}$$

Hence, we obtain a dramatic reduction in the number of parameters. Certainly, it may turn out that in order to describe the state accurately, large dimension $m$ would be needed and the number of MERA parameters may become large. However, it occurs that in many practical applications, due to the presence of disentanglers, dimension $m$ may be very small.

The fact that MERA can reflect the symmetry of a state under description is its another asset. For instance, if the state is translationally invariant, all tensors in a given layer are identical. This brings another reduction in the number of parameters which span the tensor network: in the case of translationally invariant systems, the number of parameters which describe the state does not increase linearly with the system size, but logarithmically.

### 2.4.1 Causal cones

Another feature to consider is the locality of the tensor structure shown in Fig. 2.7. In order to explain this notion, we adopt the perspective according to which MERA is a quantum circuit, as discussed earlier. Suppose that all tensors in Fig. 2.9 are given and we aim at calculating the reduced density matrix for two neighboring spins $s$ and $r$, which are high-



Figure 2.9: Causal cone for nearest neighbor spins $s$ and $r$. Thickness of this cone is three.

lighted at the bottom of the figure. To this end, the tensors are contracted from top to bottom, as can be seen in Fig. 2.9. Note, however, that $\rho^{[sr]}$ does not depend on the whole tensor structure but only on a small part of it. In other words, only a small number of tensors is connected with spins $s$ or $r$. Remember that in the quantum circuit perspective,
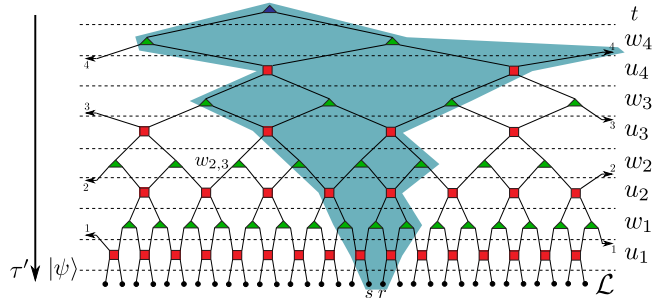
we apply gates in order defined by discrete time $\tau'$. That is, there is no need to apply, for instance, tensor $w_{2,3}$, since it influences neither $s$ nor $r$.

Tensors that contribute to $\rho^{[sr]}$ are marked in Fig. 2.9. A set of tensors which has to be taken into consideration while calculating $\rho^{[sr]}$ is called the causal cone for spins $[sr]$.

The locality feature of MERA comes from the fact that disentanglers are unitary and all isometries satisfy the condition $w_\tau^\dagger w_\tau = \mathbb{I}$. To understand it properly, let us analyze Fig. 2.10.
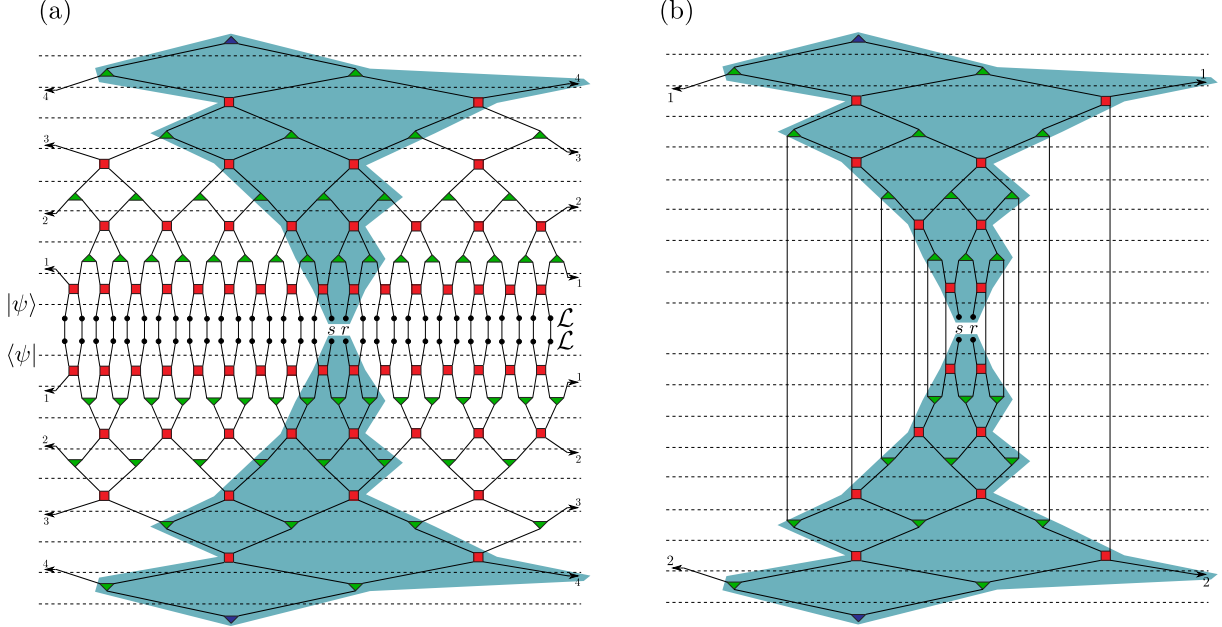


Figure 2.10: The calculation method of the reduced density matrix $\rho^{[sr]}$. (a) Upper part: MERA description of $|\psi\rangle$, lower part: MERA description of $\langle\psi|$. All sites of lattice $\mathcal{L}$ besides $[sr]$ are contracted. Rules in Fig. 2.5(b) and Fig. 2.3(b) are used to eliminate from the contraction the tensors that lie outside the causal cone. (b) Efficient contraction of the network that leads to $\rho^{[sr]}$. Cost of this calculation scales as $m^9$.

Fig. 2.10 shows the details of calculating $\rho^{[sr]}$ and clarifies the notion of causal cones. The upper part of Fig. 2.10(a) is the MERA representation of $|\psi\rangle$, whereas the lower is its Hermitian conjugate, i.e. the MERA representation of $\langle\psi|$. The reduced density matrix:

$$\rho^{[sr]} \;=\; \mathrm{Tr}_{\mathcal{L}\setminus[sr]}\, |\psi\rangle\langle\psi| \tag{2.42}$$

is calculated and, hence, all sites $\mathcal{L} \setminus [sr]$ are contracted. Multiple application of rules Fig. 2.5(b) and Fig. 2.3(b) allows us to eliminate all tensors that are outside causal cones: Firstly, tensors $u_1$ and $u_1^\dagger$ are removed by the usage of 2.5(b), then $w_1$ and $w_1^\dagger$ by 2.3(b) and so on until the remaining tensors $w_3$ and $w_3^\dagger$ are eliminated. At the end of this procedure, we obtain a simplified tensor structure illustrated ed in Fig. 2.10(b) that needs to be contracted in order to calculate $\rho^{[sr]}$.

We would like to emphasize once again that thanks to the particular tensor structure and certain conditions which are fulfilled by disentanglers and isometries, the calculation of reduced density matrices for nearest neighbors (or more general: any local observables) is efficient within the MERA algorithm. At any stage, it is not necessary to operate on a

state of the whole system $|\psi\rangle \in \left(\mathbb{C}^{2S+1}\right)^{\otimes 32}$ (in the case of an example in Fig. 2.9). This allows us to study very large systems at low cost.

There is one more feature of causal cones which deserves attention, namely, the fact that their thickness is bounded by some constant which does not depend on the lattice size but only on the geometry of a particular tensor structure, i.e. on the type of tensors used and the way they are connected. Thickness of the causal cone is measured by the total number of input wires of isometries inside the cone in a given layer. In the example presented in Fig. 2.9 thickness of the cone equals 3.

This parameter is very important because it directly translates into the complexity of the algorithm. The thicker a causal cone is, the more complex the algorithm becomes. It can be demonstrated that the cost of computation of the density matrix for nearest neighbors $\rho^{[sr]}$ scales as $m^9$ in the MERA scheme presented in Fig. 2.7 where, for the sake of simplicity, we assume that every dimension of effective spin equals $m$. A proof of this fact is provided in the next section.

### 2.4.2 Raising and lowering operations

As discussed before, MERA can be treated as a renormalization technique. Once the whole tensor structure is created, we can examine the system at different length scales. In this situation, it is possible to study how operators defined on physical lattice $\mathcal{L}$ undergo a renormalization procedure. Let us look into the case of operators $o^{[s_i s_{i+1}]}$ and $o^{[s_{i+1} s_{i+2}]}$, defined on two nearest neighbor sites. Because of the particular structure of MERA in Fig. 2.7, we may transform them either into two-site operator $o_1^{[s_i' s_{i+1}']}$ or three-site operator $o_1^{[s_i' s_{i+1}' s_{i+2}']}$ on $\mathcal{L}_1$ depending on the mutual position of operators $o^{[s_i s_{i+1}]}$, $o^{[s_{i+1} s_{i+2}]}$ and disentangler $u_1$. Figs. 2.11(a) and (b) illustrate these two cases.

Thickness of the causal cone in this MERA scheme is 3, hence, the two-site and three-site operators on lattice $\mathcal{L}_\tau$ become at most three-site ones on $\mathcal{L}_{\tau+1}$. Fig. 2.11(c) presents a general case: three-site operator on $\mathcal{L}_\tau$ is transformed by $(\tau + 1)$-th layer of disentanglers and isometries into the three-site operator on $\mathcal{L}_{\tau+1}$. The operation that transforms operator $o_\tau$ into $o_{\tau+1}$ is referred to as a raising operation $\mathfrak{R}_{\tau+1}$ of $o_\tau$:

$$o_{\tau+1} = \mathfrak{R}_{\tau+1} o_\tau . \tag{2.43}$$

In Section 4.3, we employ the technique of raising operators in order to examine correlations in the ground state of the two-dimensional orbital compass model.

The raising operation is one of the most common procedure in the MERA algorithm which is constantly repeated during its run. From a technical viewpoint, it is thus preferable to program this procedure as effectively as possible. Let us now have a closer look at the general case presented in Fig. 2.11(c). In order to calculate $o_\tau^{[s_i' s_{i+1}' s_{i+2}']}$, all 17 pairs of wires have to be contracted. Because high dimension $m$ of effective block spins is desirable, optimally, the contraction of the whole structure in Fig. 2.11(c) should scale with the lowest possible power of $m$. To simplify, we assume here that the Hilbert space of every effective spin has the same dimension $m$.
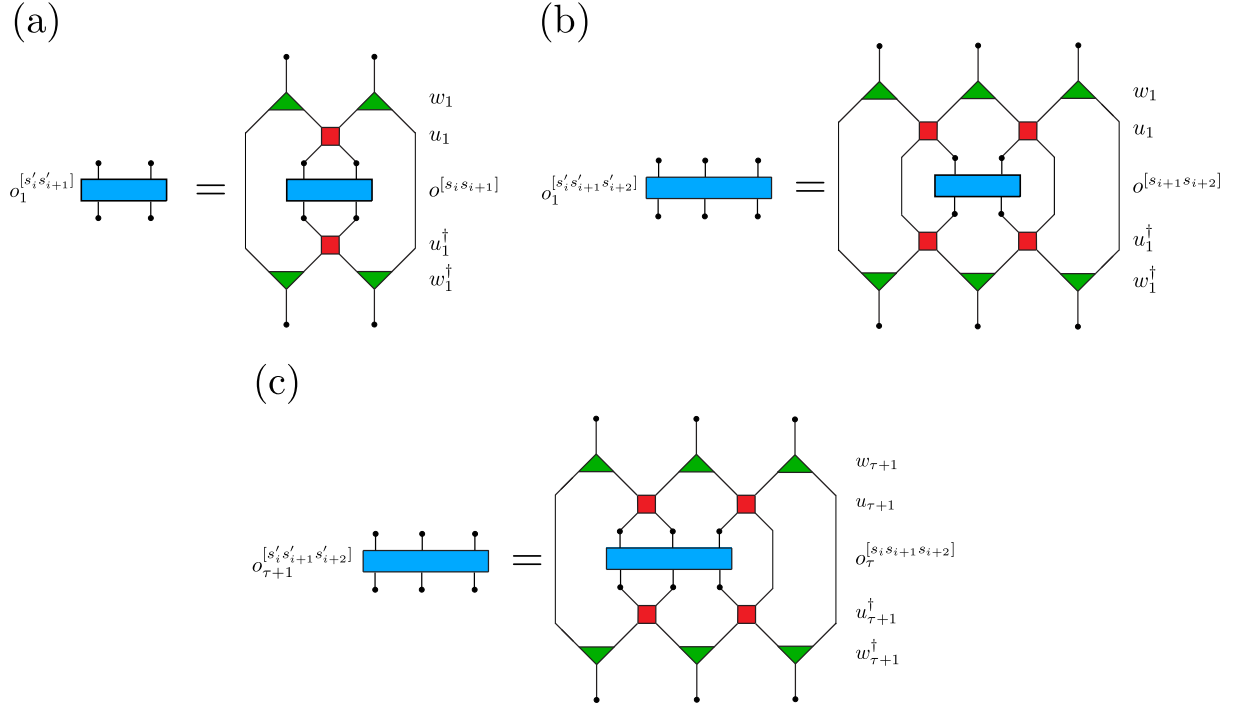
Figure 2.11: Raising operation. (a),(b) Physical, two-site operator is transformed into a two-site or three-site operator on coarse-grained lattice $\mathcal{L}_1$. (c) General case of transforming a three-site operator into three-site one.

The best strategy to contract such tensor structures is to divide the procedure into small steps and during each of them only two tensors are contracted. This strategy should be used to facilitate finding the optimal order of contracting pairs of tensors. A clear example of such an optimal choice is shown in Fig. 2.12. It can be treated as the basis for further optimization which is dealt with later on.

Thus, first of all, we divide contraction in Fig. 2.11(c) into ten steps (i) – (x), as depicted in Fig. 2.12. In each step, the black color designates a part of the contraction that has been made in previous steps. In a given step, tensors that are contracted are painted with their color which has been previously used in Fig. 2.11(c). The contractions which have to be performed at each stage are highlighted. The most expensive steps involve: (iii), (iv) and (v) – the cost of each scales as $m^9$, therefore, the contraction cost of the whole structure scales also as $m^9$.

Let us now show that there does not exist a contraction of the structure illustrated in Fig. 2.11(c) the cost of which scales as $m^8$. One of the steps of this contraction has to involve operator $o_\tau^{[s_i s_{i+1} s_{i+2}]}$ that are connected with some other parts of the structure (this may involve one tensor or a couple of them contracted in previous steps). Note that there are only two possibilities that scale as $m^8$: $o_\tau^{[s_i s_{i+1} s_{i+2}]}$ can be contracted with $u_{\tau+1}$ or with $u_{\tau+1}^\dagger$ which is placed on the left of the structure in Fig. 2.11(c). The former contraction is shown in 2.12(i), as a result, tensor $t_1$ is created. There is only one possibility of contraction involving tensor $t_1$ that scales as $m^8$ – the one with $u_{\tau+1}$. Fig. 2.12(ii) illustrates this process. This time, tensor $t_2$ is created. The cost of contracting

(i) $o_\tau^{[s_i s_{i+1} s_{i+2}]} \cdot u_{\tau+1} = t_1$
cost: $m^8$, mem.: $m^6$

(ii) $t_1 \cdot u_{\tau+1}^\dagger = t_2$
cost: $m^8$, mem.: $m^6$

(iii) $t_2 \cdot u_{\tau+1} = t_3$
cost: $m^9$, mem.: $m^8$

(iv) $t_3 \cdot w_{\tau+1} = t_4$
cost: $m^9$, mem.: $m^7$

(v) $t_4 \cdot u_{\tau+1}^\dagger = t_5$
cost: $m^9$, mem.: $m^7$

(vi) $t_5 \cdot w_{\tau+1}^\dagger = t_6$
cost: $m^8$, mem.: $m^6$

(vii) $t_6 \cdot w_{\tau+1} = t_7$
cost: $m^8$, mem.: $m^7$

(viii) $t_7 \cdot w_{\tau+1}^\dagger = t_8$
cost: $m^8$, mem.: $m^6$

(ix) $t_8 \cdot w_{\tau+1} = t_9$
cost: $m^8$, mem.: $m^7$

(x) $t_9 \cdot w_{\tau+1}^\dagger = o_{\tau+1}^{[s_i' s_{i+1}' s_{i+2}']}$
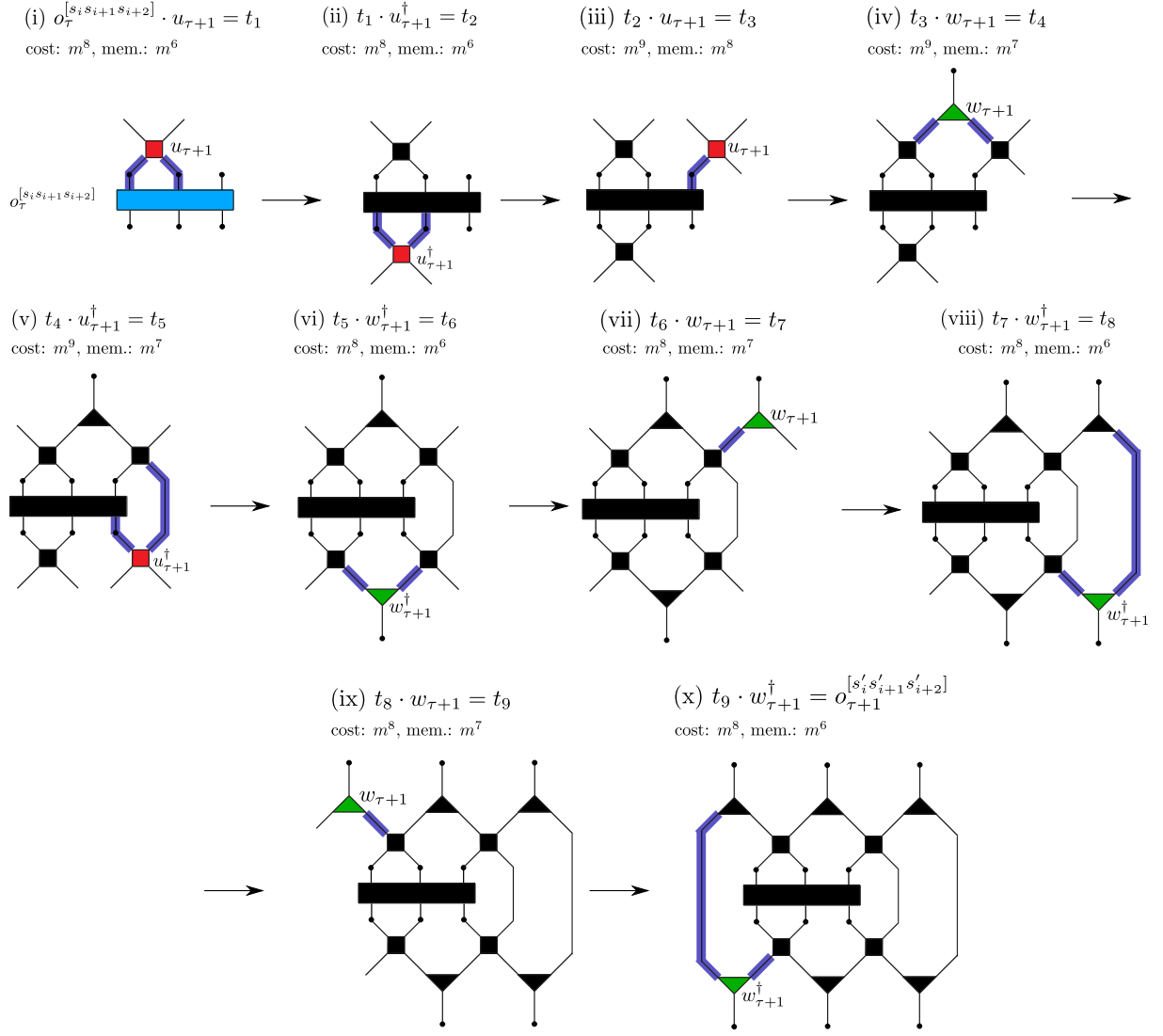cost: $m^8$, mem.: $m^6$

Figure 2.12: Optimal way of performing contraction presented in Fig. 2.11(c). The ontraction is split into ten steps (i) – (x), the cost of three of them scales as $m^9$. Intermediate results are stored in tensors $\{t_i\}_{i=1}^9$. Part of the structure painted black is contracted during previous steps. Highlighted wires designate contractions being made in a given step. The cost of contraction as well as memory used by the resulting tensor are shown in each step. Further optimization of this procedure is discussed in the text. For shorter description, here, the central dot $\cdot$ denotes tensor contraction.

$t_2$ with any other part of the remaining structure scales at least as $m^9$ with only one exception: contraction of $t_2$ with a previously created pair consisting of $w_{\tau+1}$ and $w_{\tau+1}^\dagger$ scales as $m^8$. Note, however, that such a contraction does not provide a solution, because after this process, we are still left with a tensor with six wires as before. This shows that during the contraction of the structure in Fig. 2.11(c), there has to be at least one step that scales as $m^9$.

As mentioned before, Fig. 2.12 provides a simple example of an efficient method of contracting a large tensor structure. The calculation within this procedure scale with the lowest possible power of $m$, still, some further optimizations are feasible. The procedure

involves three steps that scale as $m^9$. This can be reduced to two steps by means of the following method. Tensors $u_{\tau+1}$ and $w_{\tau+1}$ that are used in steps (iii) and (iv) can be contracted earlier, as a side calculation: $u_{\tau+1} \cdot w_{\tau+1} = z_1$ with cost $m^6$. Supplementary tensor $z_1$ is now used to skip step (iii) in Fig. 2.12 by means of contraction: $t_2 \cdot z_1 = t_4$. This method not only reduces the number of steps that scale as $m^9$, but moreover, it decreases the amount of memory required to perform calculations from $m^8$ to $m^7$.

By analogy, we can revise steps (v) and (vi) by introducing tensor $z_2$: $u^\dagger_{\tau+1} \cdot w^\dagger_{\tau+1} = z_2$, calculated with cost $m^6$. This is how it is possible to omit the construction of tensor $t_5$ by the use of $t_4 \cdot z_2 = t_6$ with cost $m^9$. As a consequence, one step which scales as $m^8$ is replaced with another one – $m^6$.

Further optimizations (which are yet less significant) are achieved by a partial contraction of isometries. Due to this, steps (vii) and (ix) can be skipped.

A special case of the raising operator concerns Hamiltonians defined on $\mathcal{L}$. Since the thickness of causal cone of the studied MERA scheme is 3, it is natural to restrict our analysis to Hamiltonians that describe interactions between nearest neighbors and next nearest neighbors:

$$\mathcal{H} = \sum_{s_i \in \mathcal{L}} h^{[s_i s_{i+1} s_{i+2}]} . \tag{2.44}$$

Each term in the above sum undergoes renormalization in structurally the same way as shown in Fig. 2.11(c). Note that renormalized three-body Hamiltonian $h_1^{[s'_i s'_{i+1} s'_{i+2}]}$ is a sum of two contributions. Thus, Hamiltonian $\mathcal{H}_1$ on coarse-grained lattice $\mathcal{L}_1$ reads:

$$\mathcal{H}_1 = \sum_{s'_i \in \mathcal{L}_1} h_1^{[s'_i s'_{i+1} s'_{i+2}]} , \tag{2.45}$$

where for all sites $s_i \in \mathcal{L}$:

$$h_1^{[s'_i s'_{i+1} s'_{i+2}]} = \mathfrak{R}_1 h^{[s_i s_{i+1} s_{i+2}]} + \mathfrak{R}_1 h^{[s_{i+1} s_{i+2} s_{i+3}]} . \tag{2.46}$$

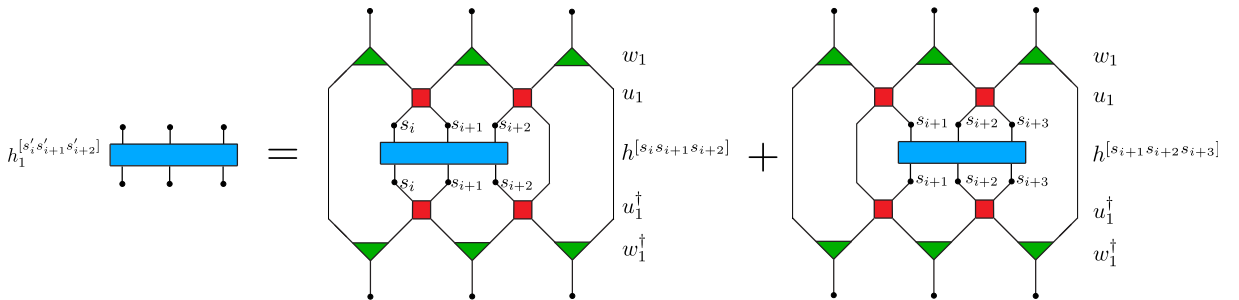Fig. 2.13 illustrates the situation referred to above.



Figure 2.13: Procedure of raising a physical Hamiltonian. Coarse-grained Hamiltonian $h_1^{[s'_i s'_{i+1} s'_{i+2}]}$ comprises two contributions which have the same structure of contraction.

Despite the fact that the two contributions in Fig. 2.13 are in general different, the structures of their contraction remain the same. From this observation, it follows that it is

useless to develop two separate procedures in order to calculate $h_1^{[s'_i s'_{i+1} s'_{i+2}]}$. It is sufficient to apply contraction in Fig. 2.12 two times: each time with a different set of component tensors. Assuming that MERA is translationally invariant, we use the following algorithm:

(i) Apply Fig. 2.12 to calculate $\mathfrak{R}_1 o$ using component tensors $u_1, w_1$ and $o = h^{[s_i s_{i+1} s_{i+2}]}$.

(ii) Apply Fig. 2.12 to calculate $\mathfrak{R}_1 \widetilde{o}$ using component tensors $\widetilde{u}_1, \widetilde{w}_1$ and $\widetilde{o}$ given by:

$$(\widetilde{u}_1)_{j_1 j_2}^{i_1 i_2} = (u_1)_{j_2 j_1}^{i_2 i_1} , \tag{2.47}$$

$$(\widetilde{w}_1)_{j_1 j_2}^{i_1} = (w_1)_{j_2 j_1}^{i_1} , \tag{2.48}$$

$$\widetilde{o}_{j_1 j_2 j_3}^{i_1 i_2 i_3} = \left( h^{[s_{i+1} s_{i+2} s_{i+3}]} \right)_{j_3 j_2 j_1}^{i_3 i_2 i_1} . \tag{2.49}$$

(iii) Use $\mathfrak{R}_1 o$ and $\mathfrak{R}_1 \widetilde{o}$ to calculate $h_1^{[s'_i s'_{i+1} s'_{i+2}]}$ :

$$\left( h_1^{[s'_i s'_{i+1} s'_{i+2}]} \right)_{j_1 j_2 j_3}^{i_1 i_2 i_3} = (\mathfrak{R}_1 o)_{j_1 j_2 j_3}^{i_1 i_2 i_3} + (\mathfrak{R}_1 \widetilde{o})_{j_3 j_2 j_1}^{i_3 i_2 i_1} . \tag{2.50}$$

The above algorithm can be easily generalized to MERA without translational invariance. For that purpose, we change Eqs. (2.47) and (2.48) in such a way that all disentanglers $\widetilde{u}_1$ and isometries $\widetilde{w}_1$ have to be assigned with proper $u_1$ and $w_1$, respectively, according to the rotation (left $\leftrightarrow$ right) of the tensor structure.

As a consequence, we note that in the case that MERA, apart from translational invariance, has additional symmetry:

$$(u_1)_{j_1 j_2}^{i_1 i_2} = (u_1)_{j_2 j_1}^{i_2 i_1} , \tag{2.51}$$

$$(w_1)_{j_1 j_2}^{i_1} = (w_1)_{j_2 j_1}^{i_1} \tag{2.52}$$

and at the same time the physical Hamiltonian is also translationally invariant and symmetric:

$$\left( h^{[s_i s_{i+1} s_{i+2}]} \right)_{j_1 j_2 j_3}^{i_1 i_2 i_3} = \left( h^{[s_i s_{i+1} s_{i+2}]} \right)_{j_3 j_2 j_1}^{i_3 i_2 i_1} \tag{2.53}$$

then, the procedure of raising the Hamiltonian given by Eq. (2.46) simplifies to:

$$h_1^{[s'_i s'_{i+1} s'_{i+2}]} = 2 \, \mathfrak{R}_1 h^{[s_i s_{i+1} s_{i+2}]} . \tag{2.54}$$

The lowering operation is defined analogically to the raising one. In this approach, the MERA scheme is read from top to bottom. Having the reduced density matrix for three consecutive sites in $\mathcal{L}_\tau$, we can calculate the reduced density matrix for corresponding sites of $\mathcal{L}_{\tau-1}$. Note, however, that this operation is ambiguous, i.e. two reduced density matrices: $\rho_\tau^{[s_i s_{i+1} s_{i+2}]}$ and $\rho_\tau^{[s_{i+1} s_{i+2} s_{i+3}]}$ can be constructed from $\rho_{\tau+1}^{[s'_i s'_{i+1} s'_{i+2}]}$ as presented in Fig. 2.14.

Because of this ambiguity, we define two operations of lowering: $\mathfrak{L}_{\tau+1}^L$ and $\mathfrak{L}_{\tau+1}^R$ for contractions shown in Fig. 2.14(a) and Fig. 2.14(b), respectively:

$$\rho_\tau^{[s_i s_{i+1} s_{i+2}]} = \mathfrak{L}_{\tau+1}^L \, \rho_{\tau+1}^{[s'_i s'_{i+1} s'_{i+2}]} , \tag{2.55}$$

$$\rho_\tau^{[s_{i+1} s_{i+2} s_{i+3}]} = \mathfrak{L}_{\tau+1}^R \, \rho_{\tau+1}^{[s'_i s'_{i+1} s'_{i+2}]} . \tag{2.56}$$
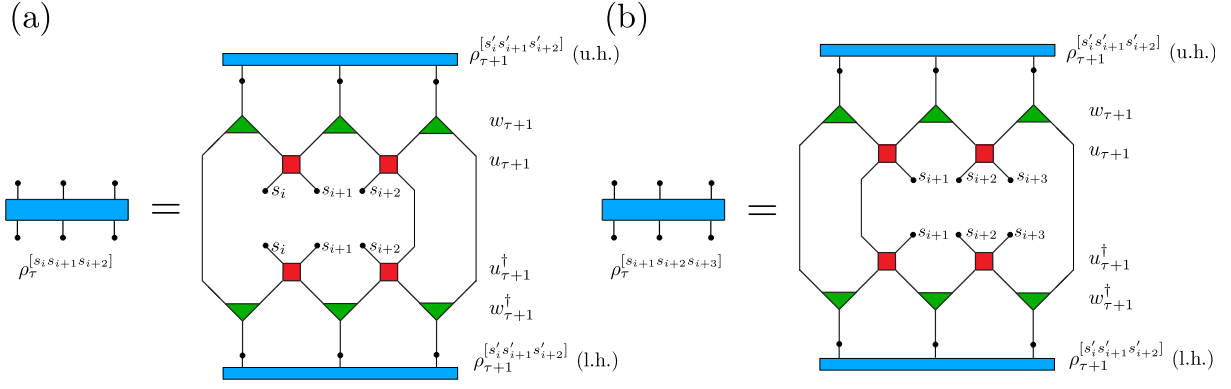
Figure 2.14: Lowering operation. Two (different in general) three-body reduced density matrices are created from $\rho_{\tau+1}^{[s'_i s'_{i+1} s'_{i+2}]}$: (a) using $\mathcal{L}^L_{\tau+1}$: $\rho_\tau^{[s_i s_{i+1} s_{i+2}]}$ and (b) using $\mathcal{L}^R_{\tau+1}$: $\rho_\tau^{[s_{i+1} s_{i+2} s_{i+3}]}$. To make the figures more transparent, reduced density matrix $\rho_{\tau+1}^{[s'_i s'_{i+1} s'_{i+2}]}$ is splitted to upper and lower "half" (u.h. and l.h. respectively).

Since tensor structures illustrated in Fig. 2.14(a) and Fig. 2.11(c) share certain similarities, it is not necessary to seek an optimal way of contracting tensors in Fig. 2.14(a) in order to calculate $\rho_\tau^{[s_i s_{i+1} s_{i+2}]}$. It suffices to follow the previously developed optimal contraction method shown in Fig. 2.12 in the reversed order. Hence, the computation of $\rho_\tau^{[s_i s_{i+1} s_{i+2}]}$ takes place in ten steps presented below. Tensors $\{r_i\}_{i=1}^9$ stores intermediary results, central dot $\cdot$ denotes a tensor contraction as in Fig. 2.12.

$$
\begin{aligned}
&\text{(i) } \rho_{\tau+1}^{[s'_i s'_{i+1} s'_{i+2}]} \cdot w^\dagger_{\tau+1} = r_1 \,, && \text{(ii) } r_1 \cdot w_{\tau+1} = r_2 \,, \\[2mm]
&\text{(iii) } r_2 \cdot w^\dagger_{\tau+1} = r_3 \,, \quad \text{(iv) } r_3 \cdot w_{\tau+1} = r_4 \,, \quad \text{(v) } r_4 \cdot w^\dagger_{\tau+1} = r_5 \,, \\[2mm]
&\text{(vi) } r_5 \cdot u^\dagger_{\tau+1} = r_6 \,, \quad \text{(vii) } r_6 \cdot w_{\tau+1} = r_7 \,, \quad \text{(viii) } r_7 \cdot u_{\tau+1} = r_8 \,, \\[2mm]
&\text{(ix) } r_8 \cdot u^\dagger_{\tau+1} = r_9 \,, \quad \text{(x) } r_9 \cdot u_{\tau+1} = \rho_\tau^{[s_i s_{i+1} s_{i+2}]} \,.
\end{aligned}
\tag{2.57}
$$

As with the raising operation, the procedure which leads to calculating $\rho_\tau^{[s_i s_{i+1} s_{i+2}]}$ in Fig. 2.14(a) can be implemented to compute $\rho_\tau^{[s_{i+1} s_{i+2} s_{i+3}]}$ in Fig. 2.14(b) by appropriate tensor substitutions, similar to those in Eqs. (2.47) – (2.49). In the presence of additional symmetries of MERA Eqs. (2.51) and (2.52), two reduced density matrices $\rho_\tau^{[s_i s_{i+1} s_{i+2}]}$ and $\rho_\tau^{[s_{i+1} s_{i+2} s_{i+3}]}$ are equal.

While working with translationally invariant systems, it is expected to remain translational symmetry also in coarse-grained lattices. Note hovewer that even for translationally invariant MERA, reduced density matrices given by Eqs. (2.55) and (2.56) do not have to be the same in general. Because of this, in translationally invariant systems we impose this symmetry by taking an average over different reduced density matrices.

## 2.5 MERA update: Obtaining the ground state

As seen in Sections 2.4.1 and 2.4.2, since the causal cone of the studied MERA scheme is 3, it is natural in this approach to examine ground state properties of Hamiltonians that describe interactions between nearest neigbors and next nearest neighbors on a lattice of size $N$ with periodic boundary conditions:

$$\mathcal{H} = \sum_{s_i \in \mathcal{L}} h^{[s_i s_{i+1} s_{i+2}]} . \tag{2.58}$$

The lattice size is given by $N = 2^{K+1}$, where $K$ stands for the number of different layers of disentanglers and isometries.

Assume for a while that all tensors in MERA are specified. Then, the energy of state $|\psi\rangle$ which is defined by MERA reads:

$$E = \sum_{s_i \in \mathcal{L}} \text{Tr} \left( h^{[s_i s_{i+1} s_{i+2}]} \rho^{[s_i s_{i+1} s_{i+2}]} \right) , \tag{2.59}$$

where $\rho^{[s_i s_{i+1} s_{i+2}]} \equiv \rho_0^{[s_i s_{i+1} s_{i+2}]}$ is the reduced density matrix for three subsequent spins on physical lattice $\mathcal{L}$. All $N$ reduced density matrices $\rho$ can be calculated by means of multiple action of lowering operations $\mathfrak{L}^L$ and $\mathfrak{L}^R$ starting from the top tensor which defines two density matrices:

$$\left( \rho_K^{[s_1' s_2']} \right)_{j_1 j_2}^{i_1 i_2} = t_{i_1 i_2} \left( t_{j_1 j_2} \right)^* , \quad \left( \rho_K^{[s_2' s_1']} \right)_{j_1 j_2}^{i_1 i_2} = t_{i_2 i_1} \left( t_{j_2 j_1} \right)^* . \tag{2.60}$$

Th aim of one of the approaches to calculating $\{\rho^{[s_i s_{i+1} s_{i+2}]}\}_{i=1}^N$ (and hence, total energy $E$) is to compute each reduced density matrix separately. To achieve this, for given three consecutive spins $[s_i s_{i+1} s_{i+2}]$, we draw their causal cone and, by reading it from top to bottom, we decide on whether to use $\mathfrak{L}_\tau^L$ or $\mathfrak{L}_\tau^R$ in order to transform $\rho_\tau$ to $\rho_{\tau-1}$ in a given layer. For some sites $[s_i s_{i+1} s_{i+2}]$ of $\mathcal{L}$, this technique leads to the following formula for reduced density matrix $\rho$:

$$\rho^{[s_i s_{i+1} s_{i+2}]} = \mathfrak{L}_1^L \mathfrak{L}_2^L \cdots \mathfrak{L}_{K-1}^R \mathfrak{L}_K^L \rho_K^{[s_1' s_2']} . \tag{2.61}$$

In Section 2.4.2, we have verified that the cost of lowering operation $\mathfrak{L}$ scales as $m^9$, what follows, is that the cost of performing the above calculations scales as $m^9 K$, i.e. as $m^9 \log N$. In order to determine the energy of the state, we need to add up $N$ such contributions. Then the total cost of computing the energy scales as $m^9 N \log N$.

By choosing another method of computing $\{\rho^{[s_i s_{i+1} s_{i+2}]}\}_{i=1}^N$, it is possible to reduce the cost of evaluating the total energy to $\mathcal{O}(m^9 N)$. To this end, we calculate all reduced density matrices in all layers, layer by layer, starting from two density matrices defined by top tensor: $\{\rho_K^\alpha\}_{\alpha=1}^2$. This method leads to a sequence of reduced density matrices on different coarse-grained lattices:

$$\{\rho_K^\alpha\}_{\alpha=1}^2 \xrightarrow{2 \times \{\mathfrak{L}_K^L, \mathfrak{L}_K^R\}} \{\rho_{K-1}^\alpha\}_{\alpha=1}^4 \xrightarrow{4 \times \{\mathfrak{L}_{K-1}^L, \mathfrak{L}_{K-1}^R\}} \{\rho_{K-2}^\alpha\}_{\alpha=1}^8 \cdots$$
$$\cdots \xrightarrow{2^{K-1} \times \{\mathfrak{L}_2^L, \mathfrak{L}_2^R\}} \{\rho_1^\alpha\}_{\alpha=1}^{2^K} \xrightarrow{2^K \times \{\mathfrak{L}_1^L, \mathfrak{L}_1^R\}} \{\rho_0^\alpha\}_{\alpha=1}^N . \tag{2.62}$$

The total number of lowering operations amounts to:

$$\sum_{n=2}^{K+1} 2^n \;=\; 2N - 4 \;. \tag{2.63}$$

The cost of calculating the energy of state given by MERA in this approach scales thus as $m^9 N$. In the case of translationally invariant MERA, all the reduced density matrices on given lattice $\mathcal{L}_\tau$ are the same. That is, only two lowering operations are crucial to transform $\rho_\tau$ into $\rho_{\tau-1}$. In this situation, the cost of computing energy scales as $m^9 \log N$.

There are basically two approaches to updating MERA in order to obtain the ground state of a given Hamiltonian, both of which are used in this Dissertation to examine the properties of two-dimensional systems.

The first one involves parametrization of every tensor of MERA. This process has to be carried out so as to preserve all the conditions that are met by tensors in MERA. Additionally, having some knowledge of symmetries that must be obeyed by the ground state under investigation, one may incorporate them into MERA tensors. This makes it possible to lower the total number of parameters that span the whole tensor structure. The application of this technique is detailed in Chapter 3.

As a result of the parametrization, the energy of the state in Eq. (2.59) is a function of some number of variational parameters: $E = E(q_1, \ldots, q_M)$. In order to obtain the ground state, it is sufficient to minimize the function by applying standard minimization procedures.

This method is set out in more detail in Chapter 3 where the ground state of a two-dimensional quantum Ising model on $4 \times 4$ and $8 \times 8$ square lattices is determined.
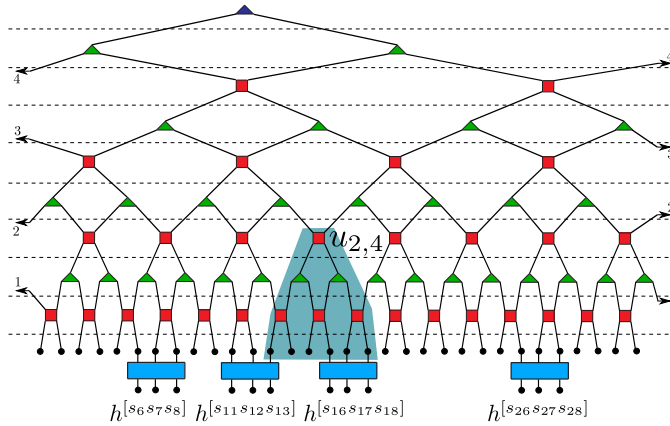


Figure 2.15: Future causal cone of $u_{2,4}$. Hamiltonians $h^{[s_6 s_7 s_8]}$ and $h^{[s_{26} s_{27} s_{28}]}$ lie outside the cone, whereas $h^{[s_{11} s_{12} s_{13}]}$ and $h^{[s_{16} s_{17} s_{18}]}$ intersect with it. Subset $\mathcal{A}$ of lattice $\mathcal{L}$ is given by $\mathcal{A} = \{s_{11}, s_{12}, \ldots, s_{18}\}$.

The second approach is based on the idea of optimizing the whole tensor which results in minimizing the total energy at each step. That is, the parametrization of the tensor network is not required. For the sake of concreteness, let us focus on optimizing disentangler $u_{2,4}$, while the rest of tensors are fixed. It is straightforward to generalize this method to other disentanglers and isometries.

At the beginning, we extract the maximal number of terms that does not depend on $u_{2,4}$ from the sum in Eq. (2.59). These terms lie outside the future causal cone of $u_{2,4}$, as shown in Fig. 2.15. To achieve this, let $\mathcal{A}$ denote a part of lattice $\mathcal{L}$ that is given by: $\mathcal{A} = \{s_i \in \mathcal{L} \mid h^{[s_i s_{i+1} s_{i+2}]}$ intersects with the future causal cone of $u_{2,4}\}$. We can thus

write:

$$
\begin{aligned}
E &= \sum_{s_i \in \mathcal{A}} \mathrm{Tr}\left(h^{[s_i s_{i+1} s_{i+2}]} \rho^{[s_i s_{i+1} s_{i+2}]}\right) + \sum_{s_i \in \mathcal{L} \backslash \mathcal{A}} \mathrm{Tr}\left(h^{[s_i s_{i+1} s_{i+2}]} \rho^{[s_i s_{i+1} s_{i+2}]}\right) \\
&= E_{\mathcal{A}} + E_{\mathcal{L} \backslash \mathcal{A}} \,.
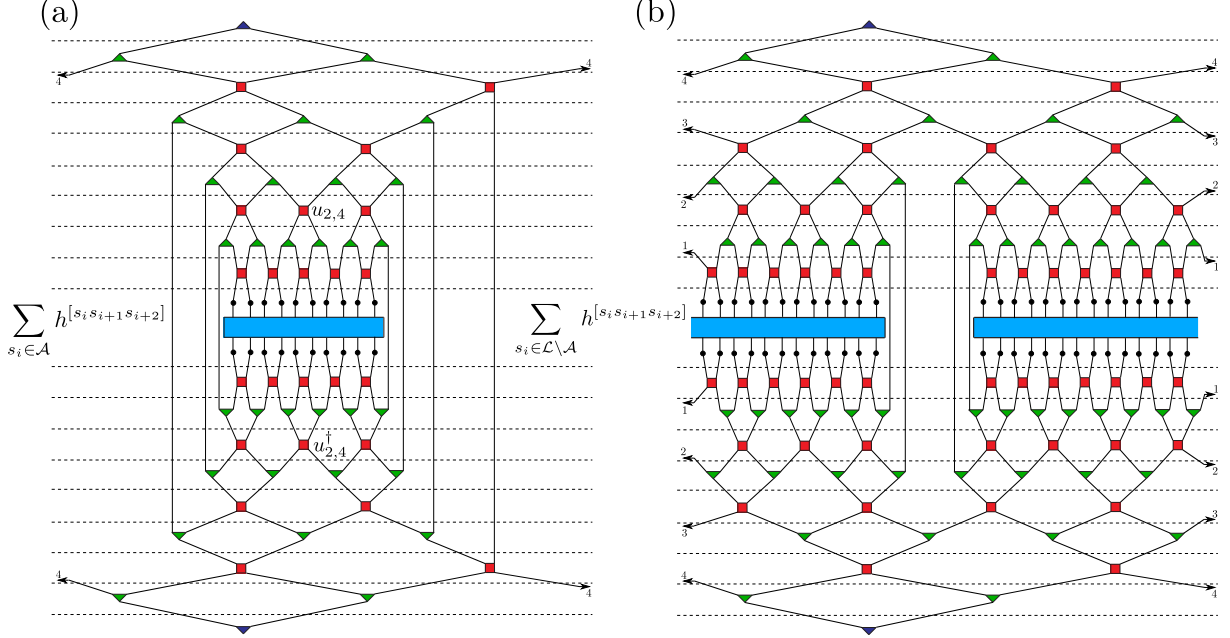\end{aligned}
\tag{2.64}
$$



Figure 2.16: Two contributions to the energy given by Eq. (2.64). (a) $E_{\mathcal{A}}$ – contribution to the energy that comes from Hamiltonians $h^{[s_i s_{i+1} s_{i+2}]}$ which intersects with the future causal cone of $u_{2,4}$. (b) $E_{\mathcal{L} \backslash \mathcal{A}}$ – contribution to the energy that comes from Hamiltonians $h^{[s_i s_{i+1} s_{i+2}]}$ which lie outside the cone. Only $E_{\mathcal{A}}$ contribution depends on $u_{2,4}$ since in an expression for $E_{\mathcal{L} \backslash \mathcal{A}}$, tensors $u_{2,4}$ and $u_{2,4}^\dagger$ are eliminated.

Only the first part ($E_{\mathcal{A}}$) of Eq. (2.64) depends on $u_{2,4}$ and thus, $E_{\mathcal{L} \backslash \mathcal{A}}$ is an irrelevant constant from the minimization procedure point of view. Fig. 2.16 illustrates this situation. In order to minimize $E_{\mathcal{A}}$ we construct the so-called environment of tensor $u_{2,4}$. The environment of $u_{2,4}$ constitutes, by definition, a network of tensors that is constructed in order to obtain $E_{\mathcal{A}}$ with eliminated tensor $u_{2,4}$. What follows from this definition is that environment $\mathcal{E}_{u_{2,4}}$ contracted with $u_{2,4}$ gives energy $E_{\mathcal{A}}$:

$$
E_{\mathcal{A}} = \mathrm{Tr}(\mathcal{E}_{u_{2,4}} u_{2,4}) \,.
\tag{2.65}
$$

Notice that environment $\mathcal{E}_{u_{2,4}}$ actually depends on $u_{2,4}$ as one of the tensors that comprises the environment is $u_{2,4}^\dagger$. Still, if we treat $u_{2,4}$ and $u_{2,4}^\dagger$ as independent tensors, the optimal choice of $u_{2,4}$ that minimizes $E_{\mathcal{A}}$ in Eq. (2.65) is given by:

$$
u_{2,4} = -VU^\dagger \,,
\tag{2.66}
$$

where $U$ and $V$ are unitary matrices that are obtained by means of singular value decomposition of environment $\mathcal{E}_{u_{2,4}}$:

$$
\mathcal{E}_{u_{2,4}} = UDV^\dagger \,.
\tag{2.67}
$$

To calculate $\mathcal{E}_{u_{2,4}}$, we proceed as follows. First of all, note that a part of the tensor structure presented in Fig. 2.16(a) can be contracted by means of raising and lowering operations. To do so, we apply raising operation $\mathfrak{R}_1$ to eight physical Hamiltonians $\{h^{[s_i s_{i+1} s_{i+2}]}\}_{i=11}^{18}$ by transforming them into four coarse-grained Hamiltonians $\{h_1^{[s_i' s_{i+1}' s_{i+2}']}\}_{i=5}^{8}$. The next step involves multiple application of lowering operations $\mathfrak{L}_\tau^L$ and $\mathfrak{L}_\tau^R$ applied with a view to computing two reduced density matrices $\{\rho_2^{[s_i'' s_{i+1}'' s_{i+2}'']}\}_{i=3}^{4}$. Having completed these two steps, environment $\mathcal{E}_{u_{2,4}}$ becomes a sum of four contributions shown in Fig. 2.17.
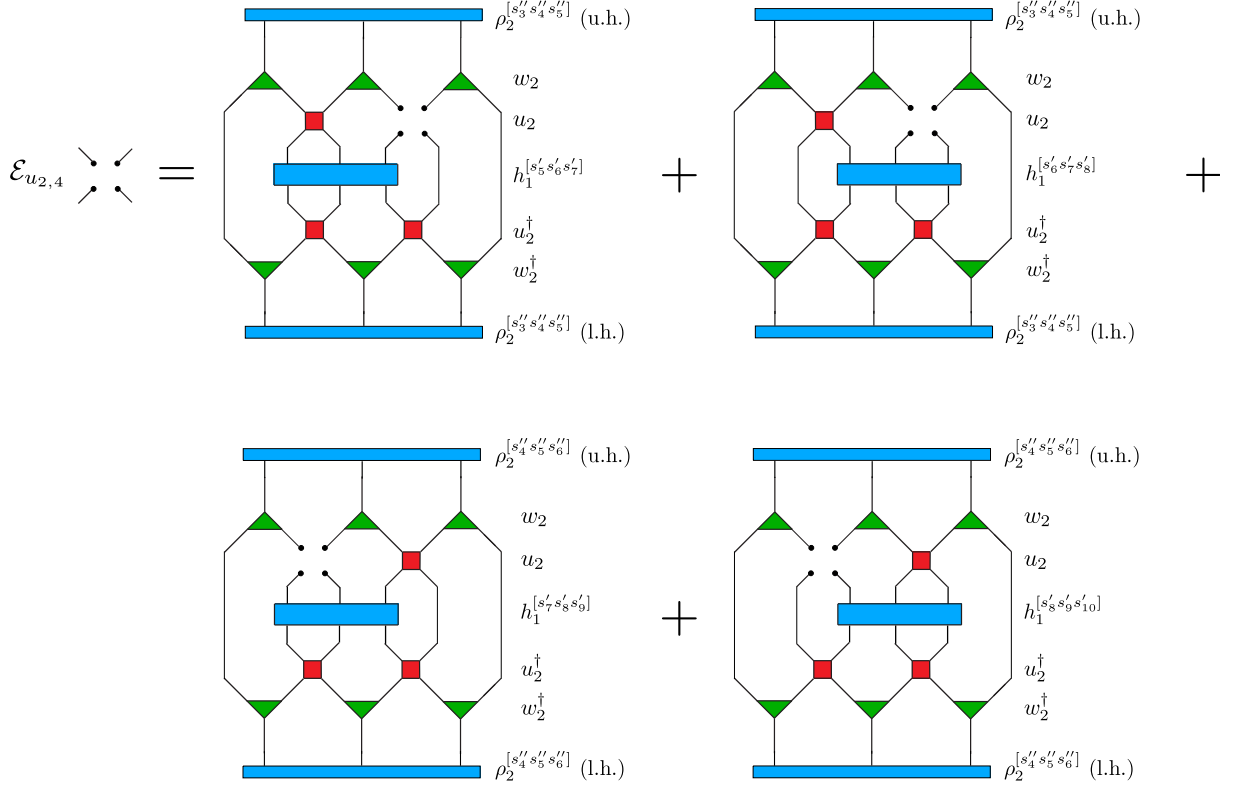


Figure 2.17: Environment of disentangler $u_{2,4}$ defined by Eq. (2.65). $\mathcal{E}_{u_{2,4}}$ consists of four independent contributions: $\mathcal{E}_{u_{2,4}} = \sum_{i=1}^{4} \mathcal{E}_{u_{2,4}}^{(i)}$. Each of them can be calculated by reusing the parts of raising and lowering procedures.

It is worth mentioning that also this time, it is not necessary to search for an optimal method of contracting any of these four contributions. The best strategy (that scales as $m^9$) is achieved by following some selected steps from the procedure of raising depicted in Fig. 2.12 and from the lowering one presented in the set of Eqs. (2.57). To illustrate so, let us calculate $\mathcal{E}_{u_{2,4}}^{(1)}$, i.e. the first contribution to $\mathcal{E}_{u_{2,4}}$ shown in Fig. 2.17. We identify a particular step of raising procedure $h_1^{[s_5' s_6' s_7']}$ where disentangler $u_{2,4}$ is used. In Fig. 2.12, this is step (iii). This provides us with information that steps (i) and (ii) from the procedure of raising can be reused in order to determine $\mathcal{E}_{u_{2,4}}^{(1)}$. The same is applicable to the procedure of lowering $(\mathfrak{L}_2^L) \, \rho_2^{[s_3'' s_4'' s_5'']}$. It follows from Eqs. (2.57) that disentangler $u_{2,4}$ is present in step (viii), i.e. steps (i) – (vii) can be used in the current calculation. Once these steps are performed, it is enough to contract two intermediary tensors: $t_2$ from

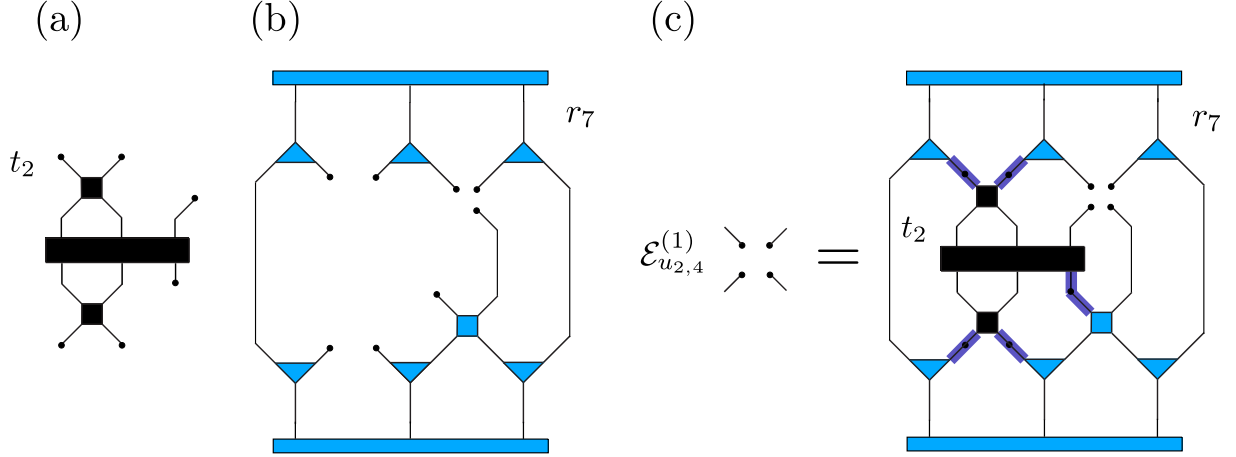Fig. 2.12 and $r_7$ from Eqs. (2.57), as presented in Fig. 2.18.



Figure 2.18: Calculating $\mathcal{E}_{u_{2,4}}^{(1)}$. (a) Parts of the raising procedure (tensor $t_2$) and (b) lowering procedure (tensor $r_7$) are used. Cost of contraction presented in (c) scales as $m^9$.

In parallel, $\mathcal{E}_{u_{2,4}}^{(3)}$ is calculated by joining parts of the procedures of raising $h_1^{[s_7' s_8' s_9']}$ and lowering (by $\mathcal{L}_2^L$) reduced density matrix $\rho_2^{[s_4'' s_5'' s_6'']}$. However, here, the above technique is degenerate because $u_{2,4}$ appears already in the first step of raising $h_1^{[s_7' s_8' s_9']}$ (see Fig. 2.12), and in the last step of lowering $\rho_2^{[s_4'' s_5'' s_6'']}$. In those circumstances, $\mathcal{E}_{u_{2,4}}^{(3)}$ is obtained as contraction of $h_1^{[s_7' s_8' s_9']}$ with intermediary tensor $r_9$ from Eqs. (2.57). Contributions $\mathcal{E}_{u_{2,4}}^{(2)}$ and $\mathcal{E}_{u_{2,4}}^{(4)}$ are computed analogously using modified raising and lowering operations by means of an indices exchange given by Eqs. (2.47) - (2.49).

The calculation of environments of isometries is like the above described referring to disentanglers. The future causal cones of isometries are thicker as compared to those of disentanglers and, hence, there are more contributions to environments. It is uncomplicated to check that there are exactly six different contributions to the environment of isometries in the MERA scheme studied in this chapter. The environment of the top tensor is structurally different because there are no reduced density matrices to be taken into account. This fact simplifies calculations since in order to calculate $\mathcal{E}_t$, it suffices to contract the renormalized Hamiltonian on coarse-grained lattice $\mathcal{L}_K$ with tensor $t^\dagger$.

The method of optimizing MERA based on the idea of computing environments of tensors leads us to the following algorithm for obtaining the ground state. Steps (i) – (vii) are iterated up to the convergence of the total energy of a state.

(i) Calculate all reduced density matrices on coarse-grained lattices $\mathcal{L}_K, \mathcal{L}_{K-1}, \ldots, \mathcal{L}_1$ using the optimal technique proposed at the beginning of the present section (by means of sequence in Eq. (2.62)).

(ii) Compute environment $\mathcal{E}_{u_{1,1}}$ of disentangler $u_{1,1}$ by means of physical Hamiltonians $\{h^{[s_i s_{i+1} s_{i+2}]}\}_{i=1}^N$ and previously calculated $\{\rho_1^{[s_i' s_{i+1}' s_{i+2}']}\}_{i=1}^{N/2}$.

(iii) Perform singular value decomposition of $\mathcal{E}_{u_{1,1}}$:

$$\mathcal{E}_{u_{1,1}} = UDV^\dagger \tag{2.68}$$

31

and update disentangler $u_{1,1}$ with its new version:

$$u_{1,1} = -VU^{\dagger} . \tag{2.69}$$

(iv) Repeat steps (ii) and (iii) for all disentanglers and isometries in the first layer.

(v) Raise all Hamiltonians $\{h_0^{[s_i s_{i+1} s_{i+2}]}\}_{i=1}^{N}$ to coarse-grained lattice $\mathcal{L}_1$ using the newest version of $u_1$ and $w_1$.

(vi) Repeat steps (ii) – (v) for all layers of tensors up to the top tensor.

(vii) Update the top tensor.

The second approach is used in Chapter 4 in order to study a quantum phase transition between the Ising-like ground state and anisotropic one of the generalized compass model in two spatial dimensions. Generalization to infinite systems is presented there, as well.

# Chapter 3

# MERA in two dimensions: Quantum Ising model

## 3.1 Symmetric two-dimensional MERA

Chapter 2 discusses the properties of one-dimensional MERA. In Ref. [34], this algorithm is generalized further to two-dimensions, and in Ref. [11], it is put in a more general unifying framework. In this chapter, we propose an alternative two-dimensional Ansatz presented in Fig. 3.1. Part (a) of this figure depicts a three-dimensional view of the structure of the proposed tensor network for a $4 \times 4$ lattice with a periodic boundary condition. Consecutive intersections of this tensor network are shown in Fig. 3.1(b). This figure explains how the original lattice is coarse-grained in a general case of an arbitrary size of the system.
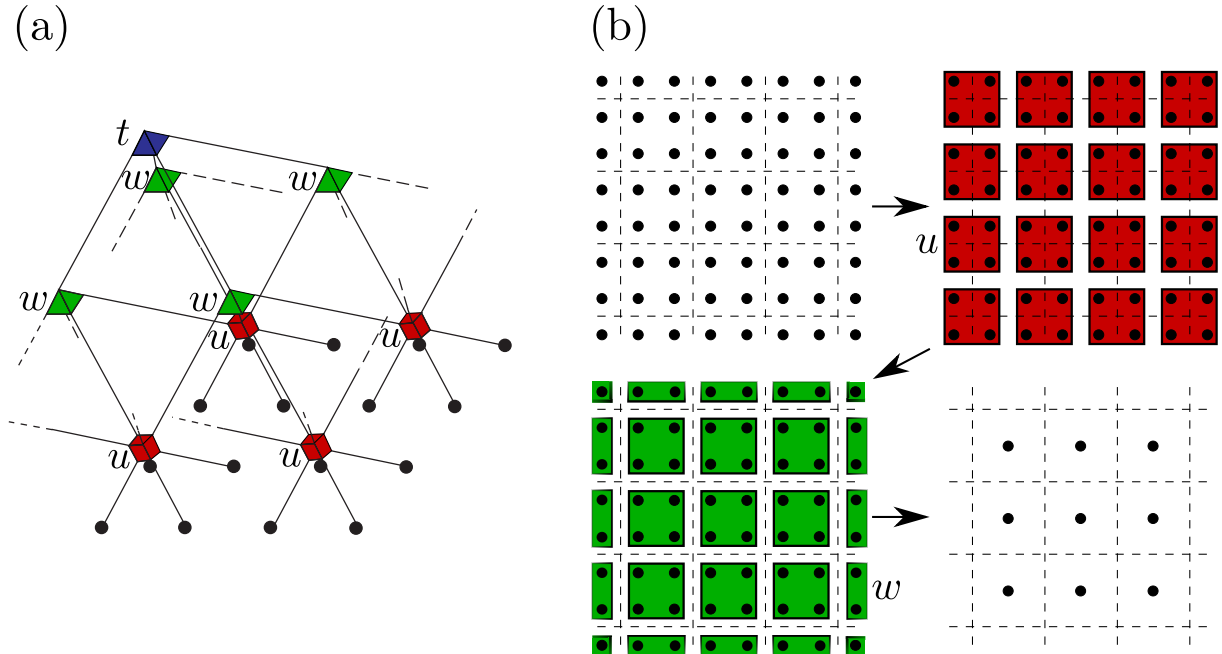


Figure 3.1: (a) Symmetric two-dimensional MERA on a periodic $4 \times 4$ lattice. Isometries $w$ replace 4-spin square plaquettes with one effective block spin in just one decimation step.

In this symmetric Ansatz, $2 \times 2$ square plaquettes shown in Fig. 3.1(b) are replaced with effective block spins in each decimation step. The symmetric Ansatz is disentangling in a systematic way all those pairs of nearest neighbor spins which belong to different $2 \times 2$-spin decimation blocks, see Fig. 3.2, where the spins on a two-dimensional square lattice are grouped into blue and red plaquettes.



We propose that, in each decimation step, each blue plaquette is replaced with an effective block spin whose Hilbert space is truncated to its $m$ most important states. Still, before each decimation, the blue plaquettes are partly disentangled by 4-spin unitary disentanglers acting on the red plaquettes. They remove entanglement between all those pairs of nearest neighbor spins which belong to different blue decimation blocks.

Indeed, note that in Fig. 3.2, all links joining such pairs of spins are painted red. These red links are naturally grouped into red plaquettes and the proposed 4-spin disentanglers remove all the unwanted "red" nearest neighbor entanglement before the next decimation.

The red plaquettes need crucially be disjoint because due to this, all the unwanted "red" entanglement can be removed by the small 4-spin disentanglers acting on individual red plaquettes. Other decimation schemes either do not remove
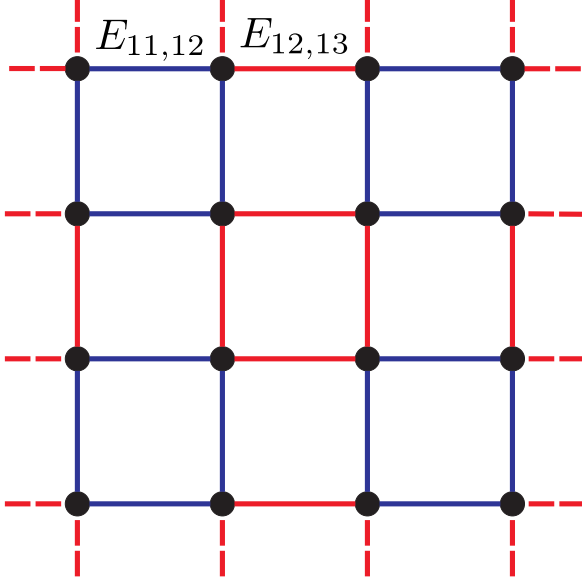
Figure 3.2: Symmetric decimation in two dimensions: each blue 4-spin square plaquette is replaced with a block spin whose Hilbert space is truncated to its $m$ most important states. Yet, before this decimation, a unitary 4-spin disentangler is applied to each red plaquette. The disentanglers remove unwanted entanglement between all those (red) nearest neighbor pairs of spins which belong to different (blue) decimation blocks.

all the unwanted nearest neighbor entanglement between different decimation blocks or they require disentanglers acting on more than 4 spins.

The symmetric variant of the renormalization group motivates MERA shown in Fig. 3.1 in the case of a $4 \times 4$ periodic lattice. This graph represents the following quantum state:

$$t_{i_{11}i_{12}i_{21}i_{22}} \times$$

$$w^{i_{11}}_{j_{44}j_{41}j_{14}j_{11}} \qquad w^{i_{12}}_{j_{42}j_{43}j_{12}j_{13}} \qquad w^{i_{21}}_{j_{24}j_{21}j_{34}j_{31}} \qquad w^{i_{22}}_{j_{22}j_{23}j_{32}j_{33}} \quad \times$$

$$u^{j_{11}j_{12}j_{21}j_{22}}_{k_{11}k_{12}k_{21}k_{22}} \quad u^{j_{13}j_{14}j_{23}j_{24}}_{k_{13}k_{14}k_{23}k_{24}} \quad u^{j_{31}j_{32}j_{41}j_{42}}_{k_{31}k_{32}k_{41}k_{42}} \quad u^{j_{33}j_{34}j_{43}j_{44}}_{k_{33}k_{34}k_{43}k_{44}} \quad \times$$

$$\left| \begin{array}{cccc} k_{11} & k_{12} & k_{13} & k_{14} \\ k_{21} & k_{22} & k_{23} & k_{24} \\ k_{31} & k_{32} & k_{33} & k_{34} \\ k_{41} & k_{42} & k_{43} & k_{44} \end{array} \right\rangle . \tag{3.1}$$

Here the double subscript indices numerate rows and columns of the lattice and the repeated indices imply summation. A generalization to greater $2^n \times 2^n$ lattices is obtained by adding $(n-2)$ layers of isometries and disentanglers.

## 3.2   Two-dimensional quantum Ising model

In this section, we use MERA to find the ground state of the spin-$\frac{1}{2}$ transverse quantum Ising model

$$\mathcal{H} = -g \sum_i \sigma^x_i - \sum_{\langle i,j \rangle} \sigma^z_i \sigma^z_j \tag{3.2}$$

on 2×2, 4×4 and 8×8 periodic square lattices. Here, $\sigma^x$ and $\sigma^z$ are Pauli matrices. Tensors $t$ and all layers of different $w_\tau$ and $u_\tau$ are optimized to minimize total energy. Provided that the minimization preserves all constraints on $t, w_\tau, u_\tau$ (normalization, orthonormality and unitarity, respectively), there is no need to obtain vectors $(w_\tau)^i$ as leading eigenstates of reduced density matrices and to construct tensors $u_\tau$ as disentanglers that minimize the entropy of those matrices. Tensors $w_\tau$ and $u_\tau$ that minimize the energy are at the same time good candidates for the leading eigenstates and optimal disentanglers, respectively.

In most calculations, we use $m = 2$ in all tensors i.e. the minimal non-trivial value of the truncation parameter, except for the $8 \times 8$ lattice where it is necessary to increase the parameter to $m = 3$, but only in top tensor $t$ near the critical $g = 3.04$. For any $g$, the initial state for the minimization is the Schrödinger cat state $|\uparrow\uparrow\uparrow \ldots \uparrow\rangle + |\downarrow\downarrow\downarrow \ldots \downarrow\rangle$ which is the ground state when $g \to 0$. This state translates into trivial disentanglers $u_\tau = \mathbb{I}$, top $t$ having only two non-zero elements $t_{0000} = t_{1111} = 1/\sqrt{2}$, and all $w_\tau$'s being non-zero only when $(w_\tau)^0_{0000} = (w_\tau)^1_{1111} = 1$.

As we seek the ground state, we assume that all tensors $t, w_\tau, u_\tau$ are real. Tensor $t$ and each vector $(w_\tau)^i$ are quantum states on a $2 \times 2$ square plaquette. We assume that $t$ is symmetric under all exchanges of lower indices that correspond to symmetry transformations of the $2 \times 2$ plaquette. Since each vector $(w_\tau)^i$ is an eigenstate of the reduced density matrix, it must be either symmetric or anti-symmetric under each of these symmetry transformations. In all considered cases, we find that the lowest energy is obtained when all vectors $(w_\tau)^i$ are assumed symmetric under all transformations. In

this symmetric subspace, it is convenient to parametrize the tensors as (here $m = 2$)

$$t_{ijkl} \simeq \sum_{\alpha=1}^{6} t_\alpha \, v_{ijkl}^\alpha \, ,$$

$$(w_\tau)_{ijkl}^n \simeq \sum_{\alpha=1}^{6} (w_\tau)_\alpha^n \, v_{ijkl}^\alpha \, ,$$

$$u = \exp\left( i \sum_{\alpha=1}^{21} q^\alpha A_\alpha \right) \, , \tag{3.3}$$

where $\simeq$ means equality up to normalization. Here $v_{ijkl}^\alpha = \langle {}_k^i {}_l^j | v^\alpha \rangle$, where the states

$$\begin{aligned}
|v^1\rangle &= |{}_0^0 {}_0^0\rangle \, , \\
|v^2\rangle &= |{}_1^1 {}_1^1\rangle \, , \\
|v^3\rangle &= \frac{1}{2} \left( |{}_0^1 {}_0^0\rangle + |{}_0^0 {}_0^1\rangle + |{}_1^0 {}_0^0\rangle + |{}_0^0 {}_1^0\rangle \right) \, , \\
|v^4\rangle &= \frac{1}{\sqrt{2}} \left( |{}_0^1 {}_1^0\rangle + |{}_1^0 {}_0^1\rangle \right) \, , \\
|v^5\rangle &= \frac{1}{2} \left( |{}_0^1 {}_0^1\rangle + |{}_1^0 {}_1^0\rangle + |{}_1^1 {}_0^0\rangle + |{}_0^0 {}_1^1\rangle \right) \, , \\
|v^6\rangle &= \frac{1}{2} \left( |{}_1^0 {}_1^1\rangle + |{}_1^1 {}_1^0\rangle + |{}_0^1 {}_1^1\rangle + |{}_1^1 {}_0^1\rangle \right)
\end{aligned} \tag{3.4}$$

are a basis of symmetric states on the $2 \times 2$ plaquette. Thus, if $m = 2$, there are 6 symmetric states while for $m = 3$, there are 21 such states. $A_\alpha$'s are imaginary 4-spin hermitian operators invariant under the symmetries of the $2 \times 2$ plaquette:

$$\begin{aligned}
A_1 &\simeq \begin{bmatrix} \sigma^y & \mathbb{I} \\ \mathbb{I} & \mathbb{I} \end{bmatrix} + \begin{bmatrix} \mathbb{I} & \sigma^y \\ \mathbb{I} & \mathbb{I} \end{bmatrix} + \begin{bmatrix} \mathbb{I} & \mathbb{I} \\ \sigma^y & \mathbb{I} \end{bmatrix} + \begin{bmatrix} \mathbb{I} & \mathbb{I} \\ \mathbb{I} & \sigma^y \end{bmatrix} \, , \\[4pt]
A_2 &\simeq \begin{bmatrix} \sigma^y & \sigma^x \\ \mathbb{I} & \mathbb{I} \end{bmatrix} + \begin{bmatrix} \sigma^x & \sigma^y \\ \mathbb{I} & \mathbb{I} \end{bmatrix} + \begin{bmatrix} \mathbb{I} & \mathbb{I} \\ \sigma^y & \sigma^x \end{bmatrix} + \begin{bmatrix} \mathbb{I} & \mathbb{I} \\ \sigma^x & \sigma^y \end{bmatrix} + \\[4pt]
&\quad \begin{bmatrix} \sigma^y & \mathbb{I} \\ \sigma^x & \mathbb{I} \end{bmatrix} + \begin{bmatrix} \sigma^x & \mathbb{I} \\ \sigma^y & \mathbb{I} \end{bmatrix} + \begin{bmatrix} \mathbb{I} & \sigma^y \\ \mathbb{I} & \sigma^x \end{bmatrix} + \begin{bmatrix} \mathbb{I} & \sigma^x \\ \mathbb{I} & \sigma^y \end{bmatrix} \, , \\[4pt]
A_3 &\simeq \begin{bmatrix} \sigma^z & \mathbb{I} \\ \mathbb{I} & \sigma^y \end{bmatrix} + \begin{bmatrix} \sigma^y & \mathbb{I} \\ \mathbb{I} & \sigma^z \end{bmatrix} + \begin{bmatrix} \mathbb{I} & \sigma^z \\ \sigma^y & \mathbb{I} \end{bmatrix} + \begin{bmatrix} \mathbb{I} & \sigma^y \\ \sigma^z & \mathbb{I} \end{bmatrix} \, , \\[4pt]
&\;\;\vdots \\[4pt]
A_{21} &\simeq \begin{bmatrix} \mathbb{I} & \sigma^y \\ \sigma^y & \sigma^y \end{bmatrix} + \begin{bmatrix} \sigma^y & \mathbb{I} \\ \sigma^y & \sigma^y \end{bmatrix} + \begin{bmatrix} \sigma^y & \sigma^y \\ \mathbb{I} & \sigma^y \end{bmatrix} + \begin{bmatrix} \sigma^y & \sigma^y \\ \sigma^y & \mathbb{I} \end{bmatrix} \, ,
\end{aligned} \tag{3.5}$$

where we use the following operator notation.

For $a, b, c, d \colon \mathbb{V} \to \mathbb{V}$ and $|i\rangle, |j\rangle, |k\rangle, |l\rangle \in \mathbb{V}$, we define:

$$\begin{bmatrix} a & b \\ c & d \end{bmatrix} \colon \mathbb{V}^{\otimes 4} \to \mathbb{V}^{\otimes 4}, \quad \begin{bmatrix} a & b \\ c & d \end{bmatrix} \left| {}_k^i {}_l^j \right\rangle = \left| {}_{k'}^{i'} {}_{l'}^{j'} \right\rangle \, , \tag{3.6}$$

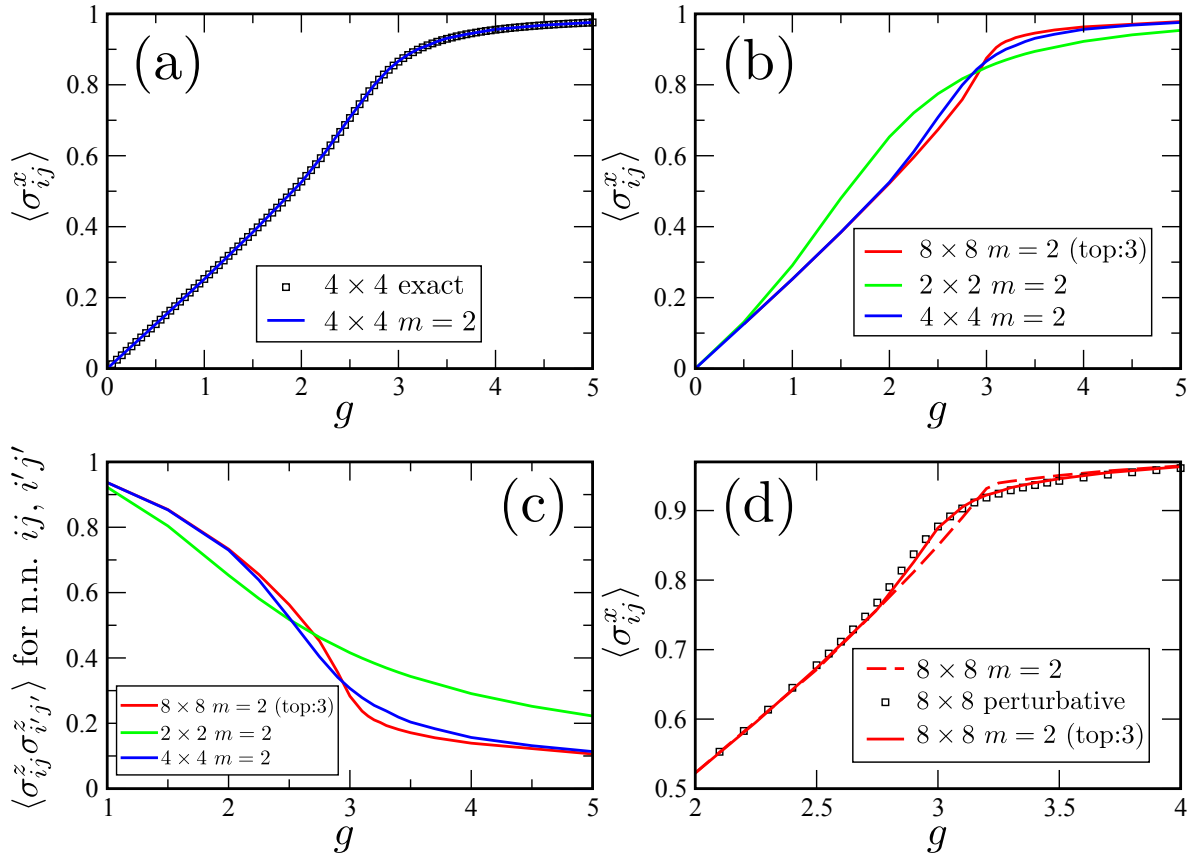where $|i'\rangle = a|i\rangle$, $|j'\rangle = b|j\rangle$, $|k'\rangle = c|k\rangle$ and $|l'\rangle = d|l\rangle$.

Figure 3.3: In (a), we compare transversal magnetization $\langle \sigma^x \rangle$ on the $4 \times 4$ lattice obtained from MERA with exact diagonalization. In (b) and (c), transversal magnetization and nearest neighbor ferromagnetic correlator obtained from MERA are shown for different lattice sizes. In (d), we compare transversal magnetization on the $8 \times 8$ lattice when $m = 2$ in all tensors and when it increases to $m = 3$ in the top tensor with the perturbative results from Ref. [29].

Each $A_\alpha$ is a symmetrized sum of tensor products of Pauli matrices with each term in the sum including an odd number of $\sigma^y$'s. They are normalized so that $\mathrm{Tr}\left[A_\alpha^\dagger A_\beta\right] = \delta_{\alpha\beta}$.

The minimized energy is a sum of all bond energies

$$E_{i,j} = -\frac{1}{4}g\left(\langle \sigma_i^x \rangle + \langle \sigma_j^x \rangle\right) - \langle \sigma_i^z \sigma_j^z \rangle . \tag{3.7}$$

However, thanks to the assumed symmetry of the tensors, only some of them need to be calculated. For example, on the $4 \times 4$ lattice in Fig. 3.2, only two bond energies: $E_{11,12}$ and $E_{12,13}$ need to be evaluated. By symmetry, all other bond energies equal either $E_{11,12}$ or $E_{12,13}$, and the total energy is $\langle \mathcal{H} \rangle = 16E_{11,12} + 16E_{12,13}$. Similarly, the $8 \times 8$ square lattice has 6 and, in general, an $N \times N$ square lattice has $\frac{N^2}{16} + \frac{N}{4}$ independent bond energies. The total number of bonds is $2N^2$ so, for large $N$, we save a factor of 32 simply by using the assumed tensor symmetries. Thus, for large $N$, the cost of calculating energy is proportional to the lattice size times the cost of calculating any bond energy $E_{i,j}$ which is polynomial in $m$. Here the proof follows similar lines as in Sections 2.4.2 and 2.5 . The indices are contracted along causal cones whose horizontal cross-section is $3 \times 3$ (or $4 \times 4$)

37

spins when cut above (or below) a layer of isometries $w$. To avoid the intermediate $4 \times 4$ stage, we do not apply all isometries first and then all disentanglers, but we apply some isometries earlier than others, gradually including disentanglers, i.e. we pass through a series of intermediate non-horizontal cross-sections never exceeding 11 spins.

The energy is minimized with respect to the variational parameters $\{t_\alpha, (w_\tau)^n_\alpha, (q_\tau)_\alpha\}$ in Eq. (3.3) using different standard minimization routines. However, the best performance is achieved with the simplest steepest descent method with gradients of the energy estimated from finite differences. Total number of variational parameters is as follows: for $4 \times 4$ lattice with $m = 2$, there are 39 parameters and in the case of $8 \times 8$ lattice with $m = 2$ and $m = 3$ (in top) – 72 and 93 parameters, respectively. Our calculations demonstrate that the energy of MERA can be minimized in a fairly straightforward manner.

In figure 3.3, we summarize our results for $2 \times 2$, $4 \times 4$ and $8 \times 8$ periodic square lattices. Panels (a) and (d) are of special interest since we compare transversal magnetization obtained from MERA with exact results on the $4 \times 4$ lattice and perturbative results on the $8 \times 8$ lattice. On the $4 \times 4$ lattice, $m = 2$ is accurate enough, but on the $8 \times 8$ lattice, $m$ in the top tensor has to be increased to $m = 3$. This is essential because with an increasing lattice size, the Ising model develops a critical point at $g = 3.04$ – this tendency can be observed in panels (b) and (c).

To conclude, in this Chapter we proposed and tested a symmetric version of MERA in 2D. Using the smallest non-trivial truncation parameter $m = 2$ in most tensors and fairly straightforward optimization methods we obtained surprisingly accurate numerical results for the ground state of the 2D quantum Ising model.

# Chapter 4

# Infinite MERA: Spontaneous symmetry breaking in a generalized orbital compass model

In this chapter, we introduce a generalized two-dimensional orbital compass model which interpolates continuously from the classical Ising model to the orbital compass model with frustrated quantum interactions, and investigate it using the infinite MERA algorithm.

The orbital compass model (OCM) is physically motivated by the orbital interactions which arise for strongly correlated electrons in transition metal oxides with partly filled degenerate $3d$ orbitals and lead to rich and still poorly understood quantum models.

Although conceptually quite simple, the OCM has an interdisciplinary character as it plays an important role in a variety of contexts beyond the correlated transition metal oxides, such as: (i) the implementation of protected qubits for quantum computations in Josephson lattice arrays [13, 26], (ii) topological quantum order [27], or (iii) polar molecules in optical lattices and systems of trapped ions [23]. Numerical studies [12, 35] suggest that when anisotropic interactions are varied through the isotropic point of the 2D OCM, the ground state is not an orbital liquid type but, instead, a first order quantum phase transition (QPT) occurs between two different types of Ising-type order dictated by one or the other interaction. Recently, the existence of this transition, similar to the one which occurs in the exact solution of the one-dimensional OCM [2, 14], has been confirmed using the projected entangled-pair state algorithm [28]. This implies that the symmetry is spontaneously broken at the compass point and the spin order follows one of the two equivalent frustrated interactions.

Having the knowledge that the ground states of the 2D Ising model and the 2D OCM are quite different, we introduce a generalized OCM which interpolates between these two limiting cases. This model allows us to investigate: (i) the physical consequences of gradually increasing frustration in a 2D system, (ii) where a QPT occurs from the Ising ground state to the degenerate ground state of the OCM, and, finally, (iii) the order and the physical mechanism of this QPT. As increasing frustration of the orbital interactions introduces entangled states, the present problem provides a unique opportunity to use the infinite MERA algorithm in order to find reliable answers to the above questions. As

explained below, the QPT in the generalized OCM occurs only surprisingly close to the maximally frustrated interactions in the OCM. We also explain the physical origin of this behavior using an analytic approach based on the spin-wave theory. These calculations are included in Appendix A.

## 4.1   Generalized compass model

In this section, we examine the nature and position of the QPT when the OCM point is approached in a different way than the one studied before [12, 35, 28], namely, when frustration of interactions along two nonequivalent directions gradually increases. Therefore, we introduce a 2D generalized OCM with ferro-like interactions on a square lattice in $ab$ plane (we assume the exchange constant $J = 1$),

$$\mathcal{H}(\theta) \;=\; -\sum_{ij\in ab} \left\{ \sigma^a_{ij}(\theta)\sigma^a_{i+1,j}(\theta) + \sigma^b_{ij}(\theta)\sigma^b_{i,j+1}(\theta) \right\}. \tag{4.1}$$

The interactions occur between nearest neighbors and are balanced along both lattice directions $a$ and $b$. Here $\{ij\}$ labels lattice sites, with $i$ $(j)$ increasing along $a$ $(b)$ axes, and $\{\sigma^a_{ij}(\theta), \sigma^b_{ij}(\theta)\}$ are linear combinations of Pauli matrices describing interactions for $S = 1/2$ spins:

$$\sigma^a_{ij}(\theta) \;=\; \cos(\theta/2)\,\sigma^x_{ij} + \sin(\theta/2)\,\sigma^z_{ij}\,, \tag{4.2}$$

$$\sigma^b_{ij}(\theta) \;=\; \cos(\theta/2)\,\sigma^x_{ij} - \sin(\theta/2)\,\sigma^z_{ij}\,. \tag{4.3}$$

The interactions in Eq. (4.1) include the classical Ising model at $\theta = 0°$ for $\sigma^x_{ij}$ operators and become gradually more frustrated with increasing angle $\theta \in (0°, 90°]$ – they interpolate between the Ising model (at $\theta = 0°$) and the isotropic OCM (at $\theta = 90°$), see Fig. 4.1. The latter case is equivalent to the 2D OCM with standard interactions $\sigma^z_{ij}\sigma^z_{i,j+1}$ and $\sigma^x_{ij}\sigma^x_{i+1,j}$ along the $a$ and $b$ directions [22, 21, 25, 24, 13, 26, 12, 35] by a straightforward unitary transformation. The model (4.1) also includes as a special case, the 2D orbital model for $e_g$ electrons at $\theta = 60°$ describing, for instance, the orbital part of the superexchange interactions in the ferromagnetic planes of LaMnO$_3$ [18].

Since the isotropic model has the same interaction strength, for the bonds along both $a$ and $b$ axis, it is symmetric under transformation $a \leftrightarrow b$, and the issue of the QPT between different ground states of the anisotropic compass model [28] does not arise. On one hand, this symmetry is obeyed by the classical Ising ground state, while on the other hand, in the ground state of the OCM, this symmetry is spontaneously broken (and the ground state is degenerate). Thus, an intriguing question concerning the ground state of the model (4.1) arises whether it has the same high symmetry as the Ising model in a broad range of $\theta$, or the symmetry is soon spontaneously broken when $\theta$ increases, i.e. there are degenerate ground states with lower symmetries, also for the $e_g$ orbital model, see Fig. 4.1(b). This question is addressed by investigating the energy contributions along two equivalent lattice directions $a$ and $b$ by applying the infinite MERA algorithm.
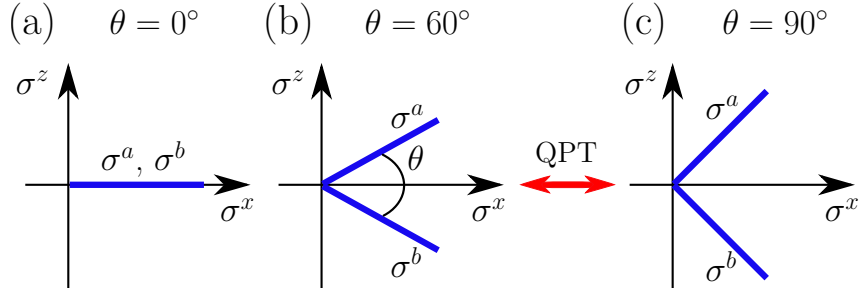
Figure 4.1: Artist's view of the evolution of orbital interactions in the generalized OCM Eq. (4.1) with increasing angle $\theta$. Blue lines indicate favored spin direction induced by interactions along two nonequivalent lattice axes $a$ and $b$. Different panels show: (a) the Ising model at $\theta = 0°$, (b) the 2D $e_g$ orbital model at $\theta = 60°$, and (c) the OCM at $\theta = 90°$. Spin order follows the interactions in the Ising limit, while it follows one of the equivalent interactions, $\sigma^a$ or $\sigma^b$, in the OCM. It results in the symmetry breaking QPT which occurs between (b) and (c), as we show in Section 4.4 and Appendix A.

## 4.2 Infinite MERA

In order to obtain the ground state, we use a translationally invariant MERA on an infinite lattice [16]. Since every layer represents a coarse-graining renormalization group transformation, depicted in Fig. 4.2 (a) and (b), we assume that after a finite number of such transformations a fixed point of the renormalization group is reached (either trivial or non-trivial) and from that time on, the following transformations are the same. In other words, at the bottom of the tensor network, there is a finite number of non-universal layers whose tensors are different in general, but above certain level, all layers are the same. The bottom layers describe non-universal short range correlations and the universal layers above this level, describe universal properties of the fixed point. Number $N$ of the non-universal bottom layers is one of the parameters of the infinite-lattice MERA. We have verified that it is sufficient to keep up to three non-universal layers, depending on how close the critical point is.

Starting with randomly selected tensors, the structure is optimized layer by layer, from the top to bottom and backwards. In given layer $\tau$, we calculate an environment of each tensor type by means of renormalized Hamiltonians $h_\tau$ and density matrices $\rho_\tau$ computed from other layers, as explained in Section 2.4.2. The environments are aimed at updating tensors to minimize the total energy. In the universal layer, this updating technique is slightly different, notably, $h_\infty$ and $\rho_\infty$ are fixed points of the renormalization procedure defined by tensors in this layer. The above steps are iterated until the convergence of energy is achieved. For given $\theta$, we obtain the ground state for different values of dimension $m$. It turns out that in most cases it suffices to work with $m = 3$, which is the same in each layer. However, it is vital to increase $m$ to 4 in the neighborhood of the critical point. The number of operations and the required memory scale as $\mathcal{O}(m^{16})$ and $\mathcal{O}(m^{12})$, respectively. The inset in Fig. 4.4(a), Section 4.4, presents the convergence of the energy of the ground state with an increasing bond dimension. Here we also present a comparison
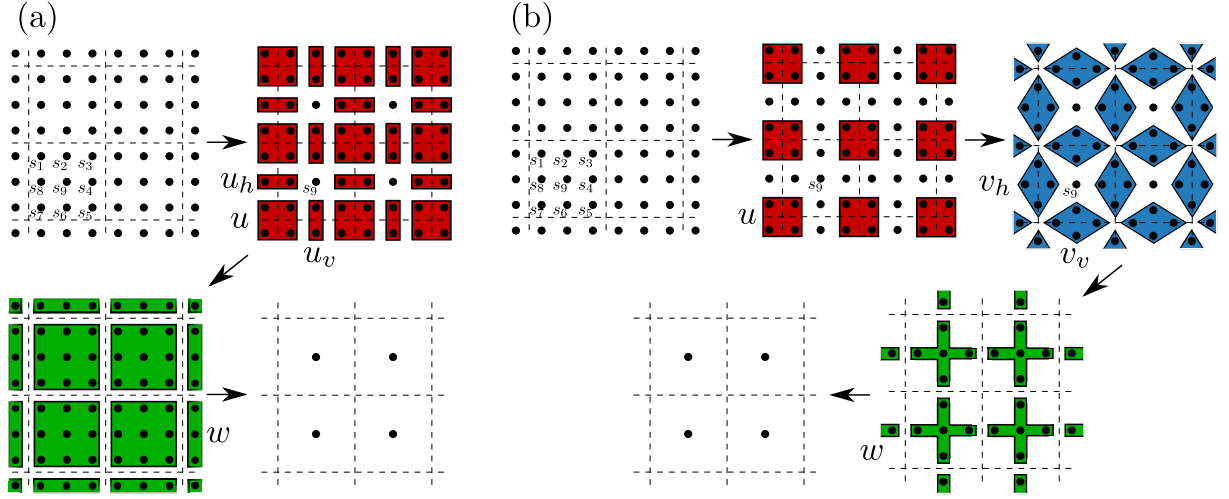
Figure 4.2: MERA schemes applied to the OCM. (a) 9-to-1 scheme: red boxes represent the action of disentanglers $u, u_h, u_v$ and green ones – isometries $w$; arrows indicate subsequent transformations used. This is a coarse-graining renormalization group transformation where each $3\times3$ plaquette in the top-left panel is replaced with a coarse-grained spin in the bottom-right panel (nine spins are replaced with one coarse-grained spin). To minimize the number of states $m$ of the coarse-grained spin, the microscopic spins are disentangled prior to decimation. (b) 5-to-1 scheme: disentanglers $u$ act on the corners of a $3 \times 3$ plaquette and additionally rotate four spins by 45°. Disentanglers $u_h$ and $u_v$ used in the 9-to-1 scheme are replaced here with tensors $v_h$ and $v_v$, which are represented by blue boxes. Isometries $w$ group five spins into one effective spin in this scheme. The labels of spins $s_1$ - $s_9$ in a single block are addressed in the text.

of results obtained with an alternative 5-to-1 scheme.

The algorithm is implemented in `c++` and optimized in order to work on multiprocessor computers. On an eight-core 2.3 GHz processor, it takes about half an hour to update the whole tensor network which consists of four layers of tensors with $m = 4$. Near the critical point, i.e. at $\theta \simeq \theta_c$, the convergence requires several thousands of iterations whereas it is significantly faster far from $\theta_c$. When $\theta$ is scanned from 0° to 90° (or back), it is more efficient to use the previous ground state as an initial state for the next discrete value of $\theta$ instead of starting from a random initial state for each value of $\theta$. We carefully verify the convergence to the ground state by scanning $\theta$ back and forth and comparing the results with those obtained from random initial states for selected values of $\theta$.

## 4.3   Correlations

In order to calculate correlations, we take advantage of the special structure of the renormalization group transformations, as illustrated in Fig. 4.2 (a) and (b). The considerations below apply to both schemes. A site of the lattice that lies in the center of a $3 \times 3$ decimation block ($s_9$ in Fig. 4.2 (a) and (b)) undergoes renormalization in a particularly easy manner. Since no disentangler is applied to this central site, a one-site operator $o_{\tau-1}$ at this site is mapped by the $\tau$-th renormalization group transformation

into a coarse-grained one-site operator

$$o_\tau = R_\tau o_{\tau-1} .$$ (4.4)

Here, $R_\tau$ is a renormalizer superoperator for the 9-to-1 scheme built out of contracted isometries only, as shown in Fig. 4.3(a):

$$(R_\tau)^{ij}_{kl} = \sum_{n_1,...,n_8=0}^{m-1} (w_\tau)^i_{n_1...n_8 k} (w_\tau^\dagger)^{n_1...n_8 l}_j .$$ (4.5)

Renormalizer superoperator for the 5-to-1 scheme can be constructed in a similar way. In that case, isometry $w_\tau$ would have five lower indices; four of them located at the edges are contracted with proper indices from $w_\tau^\dagger$.
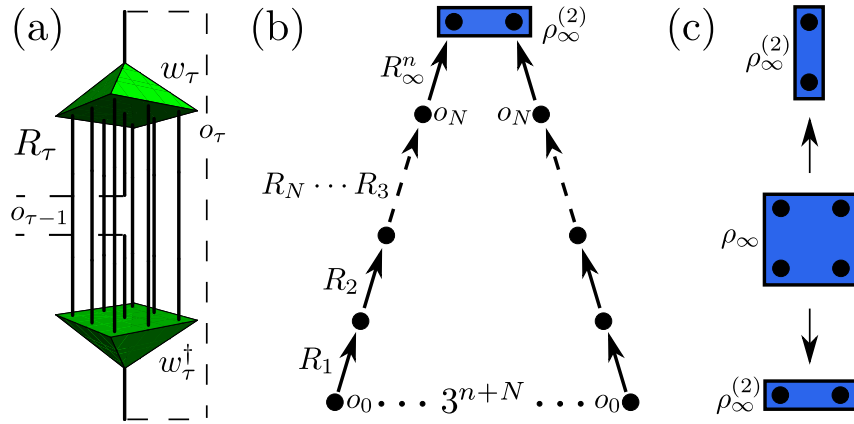


Figure 4.3: (a) Renormalizer superoperator for the 9-to-1 scheme which consists of isometries only. The connections show how the isometries are contracted; compare Eq. (4.5). (b) Method of calculating correlations $\langle o_\mathbf{x} o_\mathbf{y} \rangle = \langle o_0 o_0 \rangle$ between two sites separated by distance $3^{n+N}$. The scheme presents a graphical explanation of Eq. (4.9). (c) Deriving $\rho^{(2)}_\infty$ from $\rho_\infty$ when sites are separated vertically (top) and horizontally (bottom).

The meaning of transformations $w_\tau$ and $w_\tau^\dagger$ is demonstrated in Figs. 4.2 and 4.3(a). Thus, if we have $N$ non-universal layers at the bottom of the MERA scheme, then renormalized one-site operators at the central sites just below the universal layer are given by (see Fig. 4.3(b)):

$$o_N = R_N R_{N-1} \cdots R_1 o_0 ,$$ (4.6)

where $o_0 \equiv o$ denotes a physical, microscopic one-site operator at one of the central sites at the very bottom of the MERA tensor network.

To extract information on the correlations, it is convenient to write eigendecomposition of renormalizer $R_\infty$ in the universal layer:

$$R_\infty v_\alpha = \lambda_\alpha v_\alpha .$$ (4.7)

It is straightforward to verify the basic property of the spectrum of $R_\infty$: $|\lambda_\alpha| \le 1$. The orthonormality of vectors $(w_\infty)^i$ in Eq. (4.5) implies that the identity operator $(v_1)_{ij} = \delta_{ij}$

is an eigenvector with eigenvalue $\lambda_1 = 1$. In our numerical calculations, this is the only eigenvalue with modulus 1.

After the operator $o_N$ is decomposed as $o_N = \sum_\alpha o_N^\alpha v_\alpha$, a repeated action of the renormalizer $R_\infty$ in the universal layers can be written as

$$R_\infty^n o_N = \sum_\alpha \lambda_\alpha^n o_N^\alpha v_\alpha . \tag{4.8}$$

A correlator between two central sites $\mathbf{x}$ and $\mathbf{y}$ separated by distance $|\mathbf{x} - \mathbf{y}| = 3^{n+N}$ in the horizontal (vertical) direction is thus given by:

$$\langle o_\mathbf{x} o_\mathbf{y} \rangle = \mathrm{Tr} \left\{ \rho_\infty^{(2)} \left( R_\infty^n o_N \otimes R_\infty^n o_N \right) \right\} \tag{4.9}$$

$$= \sum_{\alpha,\beta} o_N^\alpha o_N^\beta \, c_{\alpha\beta} \lambda_\alpha^n \lambda_\beta^n \tag{4.10}$$

$$= \sum_{\alpha,\beta} \frac{o_N^\alpha o_N^\beta \, c_{\alpha\beta}}{r^{-\log_3(\lambda_\alpha \lambda_\beta)}} , \tag{4.11}$$

where $r = 3^n$ and

$$c_{\alpha\beta} = \mathrm{Tr} \left\{ \rho_\infty^{(2)} \left( v_\alpha \otimes v_\beta \right) \right\} . \tag{4.12}$$

Here $\rho_\infty^{(2)}$ is a two-site reduced density matrix in a universal layer derived from $\rho_\infty$ as depicted in Fig. 4.3(c).

Correlations corresponding to the leading eigenvalue $\lambda_1 = 1$ do not decay with the distance between $\mathbf{x}$ and $\mathbf{y}$. They describe a long range order in operator $o$ and can be used to extract its expectation value $\langle o \rangle$:

$$\langle o \rangle^2 = \lim_{|\mathbf{x}-\mathbf{y}| \to \infty} \langle o_\mathbf{x} o_\mathbf{y} \rangle = o_N^1 o_N^1 c_{11} = \left( o_N^1 \right)^2 , \tag{4.13}$$

where we use the property: $\lim_{n \to \infty} \lambda_\alpha^n = 0$ that holds for $\alpha > 1$ and the fact that $c_{11} = 1$ which is a consequence of $v_1$ being an identity. Thus, only a one-site operator with a non-zero coefficient $o_N^1$ has a non-zero expectation value. A trivial example involves the identity $o = \mathbb{I}$. Indeed, we obtain $o_N = \mathbb{I}$ in Eq. (4.6), which is equivalent to $o_N^1 = 1$, and Eq. (4.13) yields $\langle \mathbb{I} \rangle^2 = 1$, as expected.

## 4.4 Results

### 4.4.1 Symmetry breaking transition

Information about the ground state of the OCM exhibited in Eq. (4.1) is contained in average energy per bond $E(\theta)$ and energy anisotropy $\Delta E(\theta)$:

$$E(\theta) = -\frac{1}{2} \left\langle \sigma_{ij}^a(\theta) \sigma_{i+1,j}^a(\theta) + \sigma_{ij}^b(\theta) \sigma_{i,j+1}^b(\theta) \right\rangle, \tag{4.14}$$

$$\Delta E(\theta) = \left| \left\langle \sigma_{ij}^a(\theta) \sigma_{i+1,j}^a(\theta) \right\rangle - \left\langle \sigma_{ij}^b(\theta) \sigma_{i,j+1}^b(\theta) \right\rangle \right|. \tag{4.15}$$

In the classical limit of Ising interactions, $E(0°) = -1$ and $\Delta E(0°) = 0$. Due to increasing frustration, energy $E(\theta)$ gradually increases for increasing angle $\theta$ in Eq. (4.1) and reaches
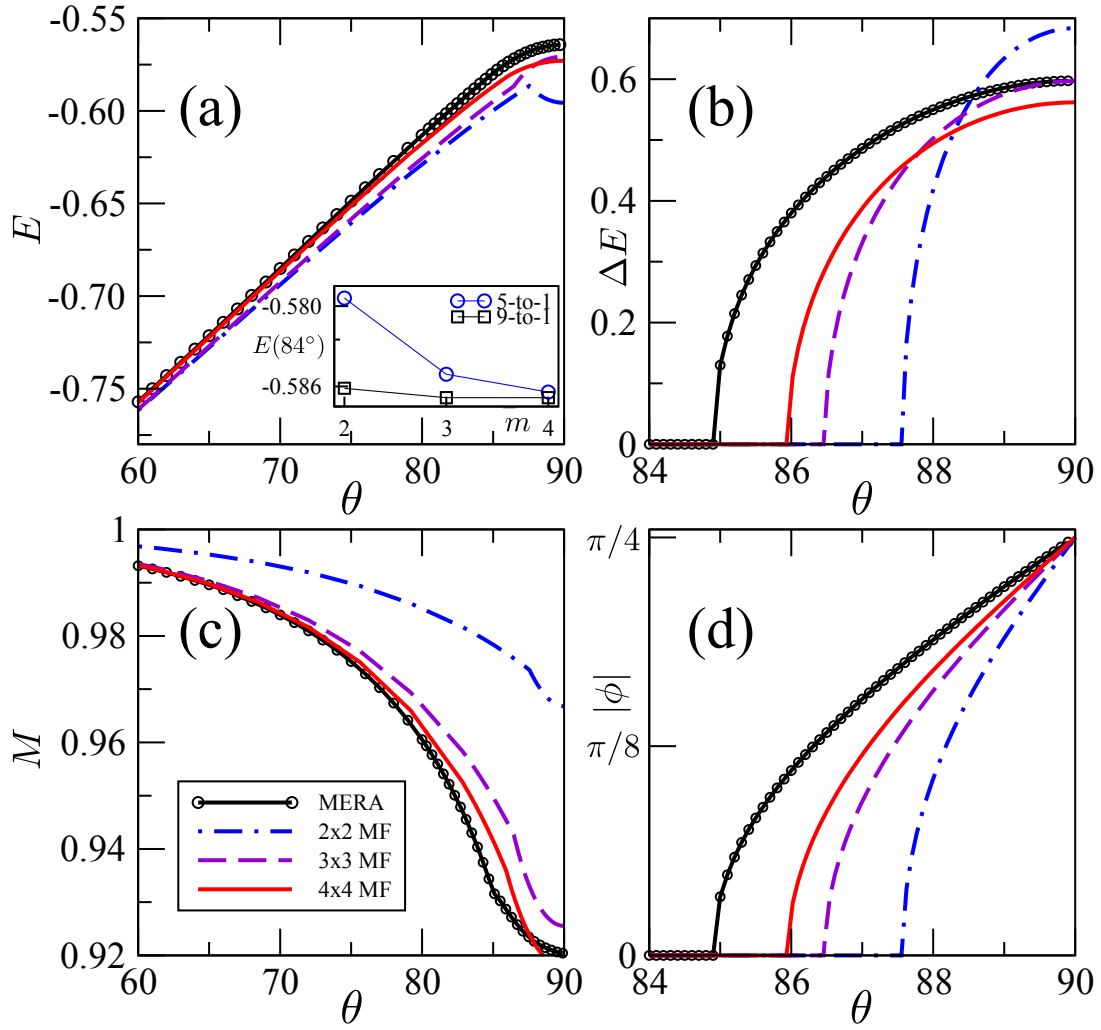
Figure 4.4: Ground state obtained for the generalized OCM Eq. (1) using MERA: (a) average energy $E$ per bond given by Eq. (4.14), (b) energy anisotropy $\Delta E$ given by Eq. (4.15), (c) spontaneous magnetization $M$ given by Eq. (4.17), and (d) magnetization orientation $\phi$ given by Eq. (4.18). Embedded $L \times L$ clusters coupled with the neighboring spins by mean-field terms ($L \times L$ MF) exhibit qualitatively similar behavior. *Inset*: Convergence of the ground state energy obtained by two MERA schemes with increasing bond dimension $m$. Black: 9-to-1 scheme presented in Fig. 4.2(a); blue: 5-to-1 scheme shown in Fig. 4.2(b). The 9-to-1 scheme results prove to converge faster for $\theta$ close to $\theta_c$. The comparison is made for schemes with the same dimension of effective block spins in all layers. The performance of the 5-to-1 scheme can be further improved by considering different dimensions on some of the effective spins.

a maximum of $E(90°) \simeq -0.57$ in the OCM, see Fig. 4.4(a). This growth is smooth and does not indicate the existence of a QPT.

However, by investigating anisotropy $\Delta E(\theta)$ shown in Eq. (4.15) between the $a$ and $b$ bonds, we identify angle $\theta_c$ at which $\Delta E(\theta)$ starts to grow. Although a gradual evolution of the ground state staring from $\theta = 0°$ might also be expected, the Ising-type state is first surprisingly robust in a broad range of angles $\theta \in [0°, \theta_c]$, and the energy associated with the bonds along the $a$ and $b$ axes remains unchanged, i.e. $\Delta E(\theta) \equiv 0$. Next, the

symmetry between the $a$ and $b$ directions is spontaneously broken above $\theta_c$, where a finite value of $\Delta E(\theta)$ is found, and then $\Delta E(\theta)$ grows rapidly with further increasing angle $\theta$, that is, large spin correlations develop along only one of the two equivalent directions $a$ and $b$. This QPT is detected by MERA at $\theta_c \simeq 84.8°$, see Fig. 4.4(b).

## 4.4.2 Magnetization in the ground state

In order to get a better understanding of the QPT at $\theta_c$, let us consider the expectation value of spontaneous magnetization $\mathbf{M} \equiv \{M^x, M^y, M^z\}$ derived from the long range order in the correlation function:

$$\lim_{|\mathbf{x}-\mathbf{y}|\to\infty} \langle \sigma_\mathbf{x}^k \sigma_\mathbf{y}^l \rangle = M^k M^l \,, \tag{4.16}$$

where $k(l) = x, y, z$. For the interactions in Eq. (1), one finds $M^y \equiv 0$ for any $\theta$.

We find that the ground state obtained using MERA for $\theta < \theta_c$ is characterized by $M^z = 0$ and an Ising-type long range order of $M^x$ which gradually decreases but still remains rather large, $|M^x| > 0.93$, in this parameter range. The symmetry between directions $a$ and $b$ is broken above $\theta_c$ by appearance of non-zero component $M^z$.

The value of the total magnetization

$$M = |\mathbf{M}| \equiv \sqrt{(M^x)^2 + (M^z)^2} \,, \tag{4.17}$$

obtained from MERA decreases continuously from $M(0°) = 1$ in the Ising model to $M(90°) \simeq 0.92$ in the OCM, see Fig. 4.4(c). Thus, the reduction in order parameter $M$ by quantum fluctuations arising from the admixture of the $z$-th component, is here rather small, and reproduces qualitative results obtained for the $e_g$ orbital model within the linear orbital wave theory [1]. Furthermore, on closer inspection of $M(\theta)$, we find that derivative $(\partial M(\theta)/\partial\theta)$ does not exist at $\theta = \theta_c$.

As expected from the behavior of $\Delta E$, the obtained symmetry breaking shown in Fig. 4.4 implies that the direction of spontaneous magnetization $\mathbf{M}$, parametrized by an orientation angle

$$\phi = \arctan\left(\frac{M^z}{M^x}\right) \,, \tag{4.18}$$

begins to change when $\theta$ increases above $\theta_c$, see Fig. 4.4(d). For $\theta < \theta_c$, the magnetization has only one component $M^x \neq 0$ with $\phi = 0$, pointing either parallel or anti-parallel to $\sigma^x$ which is half-way between $\sigma^a(\theta)$ and $\sigma^b(\theta)$, see Fig. 4.1. Below $\theta_c$, the ferromagnetic ground state is doubly degenerate and the magnetization is $\pm M = \pm|M^x|$. When $\theta$ increases above $\theta_c$, the magnetization begins to rotate in the $\{M^x, M^z\}$ plane by the non-zero angle $\pm\phi$ Eq. (4.18) with respect to the $\pm|M^x|$ initial magnetization below $\theta_c$, and each of these two states splits off into two ferromagnetic states rotated by $\pm|\phi|$ with respect to the $\sigma^x$-axis. As a result, one finds four degenerate states above $\theta_c$, and each of them is tilted with respect to $\pm\sigma^x$, either toward $\pm\sigma^a(\theta)$ or toward $\pm\sigma^b(\theta)$, depending on the sign of rotation angle $\phi$. In the OCM limit, $\theta = 90°$ is approached, the magnetization angle approaches $\phi = \pi/4$. In this limit, there are four degenerate Ising-type ferromagnetic

states, with magnetization either along $\pm\sigma^a(90°)$ (and $\langle\sigma^b(90°)\rangle = 0$), or $\pm\sigma^b(90°)$ (and $\langle\sigma^a(90°)\rangle = 0$).

In qualitative terms, the same results are obtained from the embedded $L \times L$ clusters and they are also shown in Fig. 4.4 for comparison. While the $2 \times 2$ cluster is too small and the quantum fluctuations are severely underestimated, the two larger $3 \times 3$ and $4 \times 4$ clusters are qualitatively similar and estimate the QPT point from above, see Fig. 4.4. Rather slow convergence of these results toward the MERA result for $\Delta E$ and for $|\phi|$ demonstrates the importance of longer-range correlations for the correct description of the QPT at $\theta = \theta_c$.

Altogether, these results prove that the degenerate ground state of the generalized OCM consists of a manifold of states with broken symmetry. This confirms that the OCM is in the Ising universality class [12, 35, 24] with no quantum coupling between different broken symmetry Ising-type states. However, we find the large value of $\theta_c \approx 84.8°$ rather surprising and we investigate it further using the spin-wave theory. These calculations are presented in Appendix A.

The absence of any algebraically decaying spin-spin correlations in the MERA ground state at $\theta_c$ is another surprise. They can arise from the subleading eigenvalues $\lambda_2, \lambda_3, \ldots$ which we find to be non-zero. Still, their corresponding coefficients $c_{\alpha\beta}$ with $\alpha > 1$ or $\beta > 1$ in Eq. (4.11) are small (at most $\simeq 10^{-4}$) and they decay with increasing dimension $m$ and especially the number of non-universal layers $N$. As a consequence, the only non-vanishing term in Eq. (4.11) is the leading one for $\alpha = \beta = 1$, describing the non-decaying long range order. Notice that this observation does not exclude non-trivial short range correlations up to a distance $3^N$ described by the $N$ non-universal layers. We believe that when $N$ is too small, then the missing short range correlations find their way to show up in the small but non-zero universal coefficients $c_{\alpha\beta}$, but these coefficients decay quickly with increasing $N$ as the short range correlations become accurately described by the increasing number of non-universal layers.

## 4.5   Conlusions

In sum, we have found that the second order quantum phase transition in the generalized orbital compass model (Eq. (4.1)) occurs at $\theta_c = 84.8°$ which is surprisingly close to compass point $\theta = 90°$, i.e. only when the interactions are sufficiently strongly frustrated. There is spontaneous ferromagnetic magnetization at any angle $\theta \in [0°, 90°]$. Below $\theta_c$, the ferromagnetic ground state is doubly degenerate with the spontaneous magnetization, either parallel or anti-parallel to average direction $\sigma^a_{ij} + \sigma^b_{ij}$. None of the directions, neither $a$ nor $b$, is preferred in this symmetric phase. In contrast, when $\theta$ increases above $\theta_c$, the symmetry between $a$ and $b$ becomes spontaneously broken and the ferromagnetic magnetization begins to align parallel/anti-parallel to either $\sigma^a_{ij}$ or $\sigma^b_{ij}$. The ground state is fourfold degenerate in this symmetry-broken phase. The spontaneous magnetization $M$ is close to 1 and quantum fluctuations remain small in the whole range of $\theta \in (0°, 90°]$.

These results are obtained using MERA and the mechanism of the QPT is explained

within the spin-wave theory. For classical spins, the minimum of energy is at one of the two symmetric states with the magnetization either parallel or anti-parallel to $\sigma^a_{ij} + \sigma^b_{ij}$, see Fig. A.1. The minimum becomes more and more shallow as compass point $\theta = 90°$ is approached. However, the quantum fluctuations are weak due to the gapful orbital wave excitations, and only very close to the above OCM point, become strong enough to split the shallow minimum into two distinct minima in the vicinity of the OCM point. In this way, the symmetry between the $a$ and $b$ axes is spontaneously broken. For this reason, the orbital $e_g$ model with ferro-orbital interactions, considered in Ref. [1], and corresponding to a "moderate" value of $\theta = 60°$ (see Fig. 4.1(b)), orders in a symmetric (uniform) phase induced by the stronger (here $\propto \sigma^x_{ij}\sigma^x_{i'j'}$) interaction component.

Interestingly, since – unlike in the Landau paradigm – the symmetry in the present model (cf. Eq. (4.1)) is broken rather than restored by quantum fluctuations, we do not find any algebraically decaying spin-spin correlations at the critical point found in the generalized orbital compass model (Eq. (4.1)). The spin waves also remain gapful at this point.

# Chapter 5

# Finite-range MERA: Further applications

In this chapter, we consider another variation of the MERA algorithm, namely, finite-range MERA. Typically, for a lattice with $N$ sites, MERA consists of $\log_2 N$ layers of tensors (Fig. 2.7). In this approach, we eliminate some number of layers that lie at the top of the network. Additionally, we replace the uppermost layer of isometries by top tensors $t$. This reduction causes that correlations in state $|\psi\rangle$ described by this tensor network are limited, i.e. there is no correlation between sites of the lattice which are separated by a distance larger than given number $\zeta$. This follows from the fact that causal cones for such sites are disjoined. Fig. 5.1 provides an example of finite-range MERA for the lattice of 32 spins with periodic boundary conditions. This figure depicts pairs of sites which are both still correlated and not correlated.

This example includes finite-range MERA consisting of a usual layer of disentanglers $u_1$ and isometries $w_1$ together with the second layer where the isometries are replaced by top tensors $t$. In the absence of three layers, sites $s_i$ and $s_{i+r}$ where $r \geq \zeta = 10$ are not correlated which means that $\langle o^{[s_i]} o^{[s_{i+r}]} \rangle = \langle o^{[s_i]} \rangle \langle o^{[s_{i+r}]} \rangle$.

From the perspective of a renormalization algorithm, the MERA scheme in 5.1 gener-
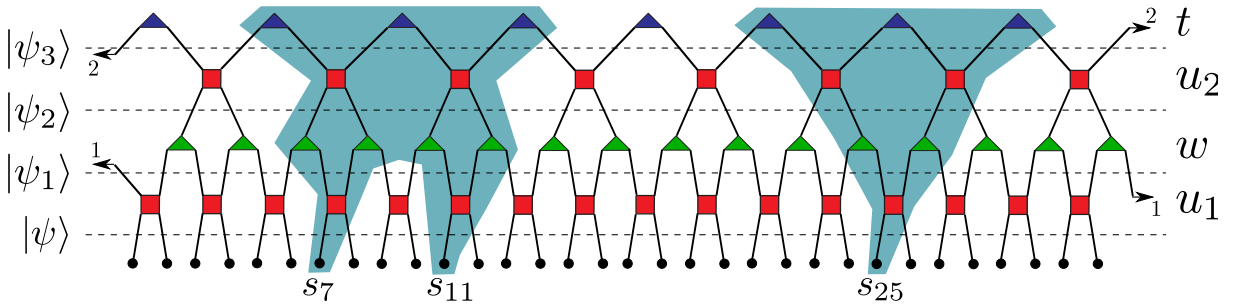


Figure 5.1: Example of finite-range MERA for a lattice of 32 spins with periodic boundary conditions. Wires denoted by the same numbers are connected. Sites $s_{11}$ and $s_{25}$ are not correlated because their causal cones are disjoined, i.e. $\langle o^{[s_{11}]} o^{[s_{25}]} \rangle = \langle o^{[s_{11}]} \rangle \langle o^{[s_{25}]} \rangle$. However, it is possible to have non-zero correlations between e.g. $s_7$ and $s_{11}$.

ates a sequence of states:

$$|\psi\rangle \xrightarrow{u_1^\dagger} |\psi_1\rangle \xrightarrow{w^\dagger} |\psi_2\rangle \xrightarrow{u_2^\dagger} |\psi_3\rangle \ . \tag{5.1}$$

What follows from the above construction is that state $|\psi_3\rangle$ is a product state: $|\psi_3\rangle = \bigotimes_{i=1}^8 |\psi_i^t\rangle$, where each $|\psi_i^t\rangle$ is a state directly given by top tensor $t$.

Finite-range MERA can also be used in order to find the ground state of a given Hamiltonian. The algorithm for updating the network is the same as the one described in Section 2.5. Still, in this case, the procedure is computationally less demanding since the network comprises fewer layers and hence, there are fewer tensors to optimize. The computational cost scales as $m^9$, i.e. it does not depend on the system size. This explains why such an ansatz is more suitable for describing the ground state with a finite range of correlations $\xi$. Here, the number of layers should be such that corresponding $\zeta$ would be larger than $\xi$.

Let us now consider two lattices of $N_1 = 2^{K_1}$ and $N_2 = 2^{K_2}$ sites, where $K_2 > K_1$ and two translationally invariant Hamiltonians with the same three-body interactions on each lattice. In order to obtain the ground states, in both cases, we employ the same translationally invariant finite-range MERA scheme with $K < K_1 < K_2$ layers as well as the updating technique based on the method of calculating environments which begin with the same initial conditions. Note that, in spite of the fact that lattices differ in size, we use the same number of tensors to describe both ground states.

Recall that the environment of a tensor in a given layer $\tau$ depends on other tensors in that layer, reduced density matrices $\rho_\tau$ and Hamiltonians $h_{\tau-1}$. $\rho_\tau$ is calculated by means of a multiple action of lowering operation $\mathfrak{L}$. Since in both cases there is the same number of layers above layer $\tau$, the corresponding reduced density matrices $\rho_\tau$ are also the same, i.e. they do not depend on the lattice size. As a consequence, the environments and therefore, the updated tensors are also identical. It follows that irrespective of the lattice size, at the end of the updating procedure, the descriptions of the ground state and also their energies are exactly the same.

This property can be used to take the limit of an infinite lattice. In this way, we obtain a very compact description (by means of just a few tensors) of translationally invariant, infinite systems.

It is clear that the above argument cannot be used for full MERA schemes: as there are more layers above layer $\tau$ in MERA for a larger lattice, reduced density matrices $\rho_\tau$ are in general different.

We can go further with this idea and reduce the number of layers in finite-range MERA to just one. The scheme presented Fig. 5.1 becomes trivial as it consists of one layer of disentanglers that is followed by top
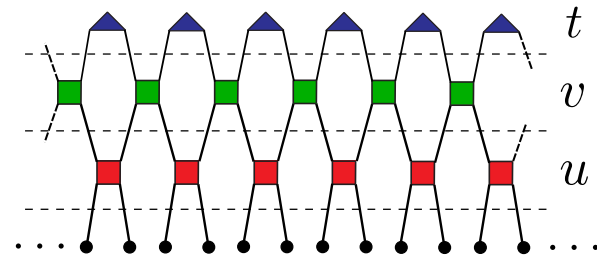


Figure 5.2: Finite-range MERA can be constructed on the basis of the more complicated MERA schemes. In this case, two layers of disentanglers are followed by top tensors. In this scheme, we have $\xi = 6$.

tensors. This single layer allows to further simplify the updating procedure. The operations of raising and lowering are not needed in this approach. Because of this, the cost of calculations scales as $m^6$ for a two-body, physical Hamiltonian, which is significantly lower than the cost in the general case. Notice that in full MERA scheme, the width of the causal cone is 3, and thus, the overall cost of calculations for a two-body and three-body Hamiltonian scales identically (as $m^9$).

Although the above example leads to a trivial scheme, one can think of more complicated schemes than those studied in Chapter 2. For instance, instead of one layer of disentanglers, two layers of disentanglers can be considered in order to enhance the disentangling power of the scheme. In full MERA scheme, it would result in an increase in the width of the causal cone up to 5. Using this scheme as a base, we can construct finite-range MERA with one layer of tensors, as shown in Fig. 5.2. In this example, $\zeta = 6$ but still the cost of calculations scales as $m^8$ even for a three-body, physical Hamiltonian.
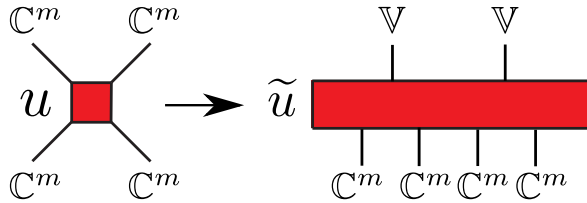


Figure 5.3: Enhancing the computational power of the scheme in Fig. 5.2 by means of replacing disentanglers $u$ by tensors $\widetilde{u}$. In the case of dim $\mathbb{V} = m^2$, tensor $\widetilde{u}$ is a disentangler.

The low cost of computation makes it possible to use large values of dimension $m$. This may be achieved by introducing additional changes into the scheme in Fig. 5.2. To this end, we extend disentanglers in the first layer in such a way that they act on more than two spins of a physical lattice. In the example presented in Fig. 5.3, tensor $\widetilde{u}$ is a disentangler provided that the dimension of spaces $\mathbb{V}$ is $m^2$ – in this case no information about the described state is lost. On a moderate computer, it is possible to extend disentanglers $u$ to act on 16 spins. Such an extension of the first layer of tensors lead to $\zeta = 48$ as well as allows to consider Hamiltonians which describe interactions on a longer range, at the same computational cost.

In two dimensions, considering finite-range MERA that comprises one layer leads to more spectacular gains in computational cost. For instance, we can built finite-range MERA by means of using only one layer of disentanglers in the two-dimensional scheme Fig. 3.1 and replacing the first layer of disentanglers with four-body tops. The cost of calculation in such a scheme scales as $m^{12}$ whereas because of the fact that the width of the causal cone is $3 \times 3$, the cost in the corresponding full MERA is $m^{28}$. Again, we can benefit from this low cost and propose a one-layer scheme that is more efficient in removing entanglement. Analogously to the one-dimensional case discussed above, we add another layer of disentanglers, as presented in Fig. 5.4(a). In this scheme, pairs of spins $s_{i,i}$ and $s_{i+5,i}$ as well as $s_{i,i}$ and $s_{i+5,i+5}$ can be correlated. Each spin of lattice $\mathcal{L}_0$ is entangled with 35 neighboring spins.

The computational cost scales as $m^2 m_1^7 m_2^{10}$ where $m_1$ and $m_2$ are the dimensions of
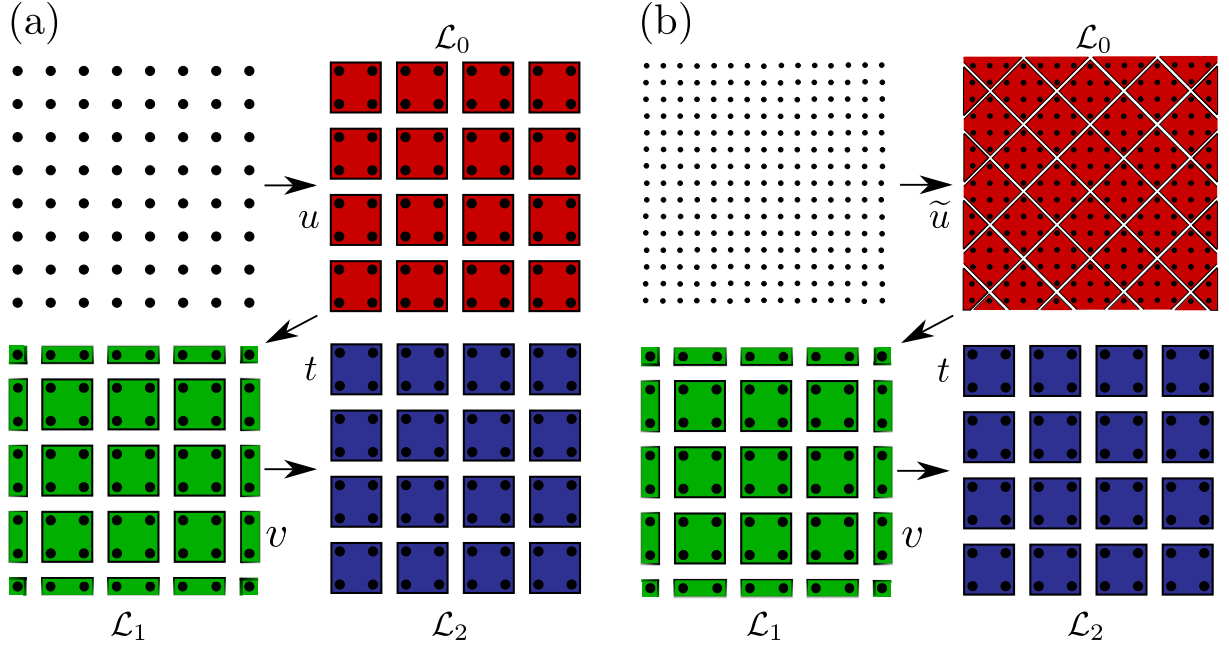
Figure 5.4: (a) Two-dimensional equivalent of the scheme presented in Fig. 5.2. (b) Disentanglers in the first layer are enlarged to take into account more spins of physical lattice $\mathcal{L}_0$ (8 in this example).

effective spins on lattices $\mathcal{L}_1$ and $\mathcal{L}_2$, respectively:

$$u\colon (\mathbb{C}^{m_1})^{\otimes 4} \to (\mathbb{C}^m)^{\otimes 4} \,,$$
$$v\colon (\mathbb{C}^{m_2})^{\otimes 4} \to (\mathbb{C}^{m_1})^{\otimes 4} \tag{5.2}$$

and $t \in (\mathbb{C}^{m_2})^{\otimes 4}$. In spin-$\frac{1}{2}$ systems, the amount of calculations is small and the disentanglers may be enlarged in the first layer as shown in Fig. 5.4(b). Now, tensors $\widetilde{u}$ map 8 sites of $\mathcal{L}_0$ into 4 effective sites of $\mathcal{L}_1$:

$$\widetilde{u}\colon (\mathbb{C}^{m_1})^{\otimes 4} \to (\mathbb{C}^m)^{\otimes 8} \,. \tag{5.3}$$

The extended scheme involves the pairs of spins $(s_{i,i}, s_{i+11,i})$, $(s_{i,i}, s_{i,i+10})$ and $(s_{i,i}, s_{i+5,i+5})$ which are correlated. In this case, each spin is entangled with as many as 71 neighboring spins of the physical lattice.

If $m_1 = 4$, this mapping is exact. However, we can introduce additional truncation of Hilbert space and use $m_1 < 4$. The same is applicable to the next layer of disentanglers. In this approach we deal with two refinement parameters: $m_1$ and $m_2$ in which convergence of results may be verified.

We employ both schemes presented in Fig. 5.4 in order to study ground state properties of the $J_1 - J_2$ model as well as the spin model which emerges as a limit of some fermionic Hamiltonian.

## 5.1  $J_1 - J_2$ model

In this section we study the $J_1 - J_2$ model given by the following Hamiltonian:

$$\mathcal{H} = J_1 \sum_{\langle i,j \rangle} \mathbf{S}_i \cdot \mathbf{S}_j + J_2 \sum_{\langle\langle i,j \rangle\rangle} \mathbf{S}_i \cdot \mathbf{S}_j , \tag{5.4}$$

where $J_1 > 0$ is the strength of the nearest neighbor interaction and $J_2 \geq 0$ is the next-nearest neighbor exchange constant. For simplicity, we assume that $J_1 = 1$.

There are two cases in which properties of the ground state of Hamiltonian (5.4) are well-known. For $J_2 = 0$, the ground state is a Heisenberg antiferromagnet with Néel order, whereas for $J_2 \to \infty$, the lattice is split into two sub-lattices with Néel order on each. The non-zero value of $J_1$ brings about the so-called collinear order in limit $J_2 \to \infty$. The above two cases are illustrated in Fig. 5.5(a). For intermediate values of $J_2$, the ground state becomes frustrated, and hence at some value of $J_2$, it is expected that Néel order is destroyed. For the same purpose, at a particular value of $J_2$ (possibly larger), the collinear order emerges. It has been verified that between the two points mentioned above, there exists a phase where no magnetic order exists. Some properties of this phase have been established by means of variational Monte Carlo [3] and series expansion [30]. Although an approximate phase diagram is established (see Fig. 5.5(b) for reference), still, there is a number of open questions that stimulate further research.
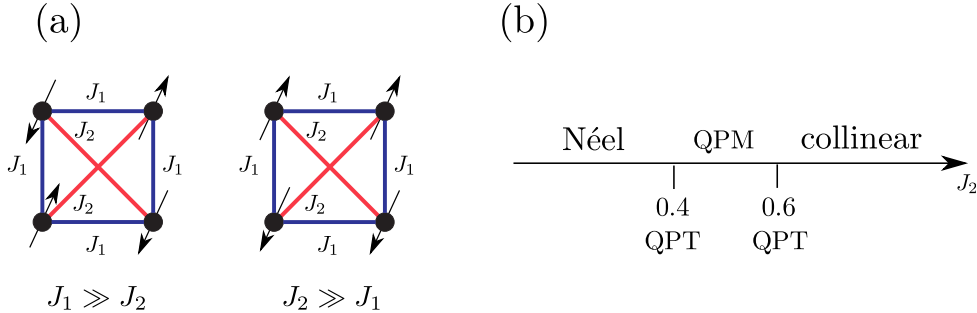


Figure 5.5: (a) Two limits of the $J_1 - J_2$ model: $J_1 \gg J_2$ poses a standard two-dimensional Néel order while $J_2 \gg J_2$ results in the collinear order. (b) Approximate phase diagram for the $J_1 - J_2$ model. There are at least three distinct phases with two quantum phase transitions between them. Néel order survives up to $J_2 \simeq 0.4$ when it changes into quantum paramagnet (QPM). Another known phase transition occurs at $J_2 \simeq 0.6$. At that point, the order of the state changes into collinear. This phase preserves for $J_2 \to \infty$.

In order to study the ground state of Hamiltonian Eq. (5.4), we apply finite-range MERA which consists of one layer of tensors only. In this approach, we use both two-dimensional schemes discussed in the previous section presented in Fig. 5.4. Note that both of them are fully capable of describing all possible orders that are expected in the $J_1 - J_2$ model. Special attention has to be paid to the scheme shown in Fig. 5.4(b) where nontrivial extension of disentanglers which is compatible with Néel and collinear order is proposed.
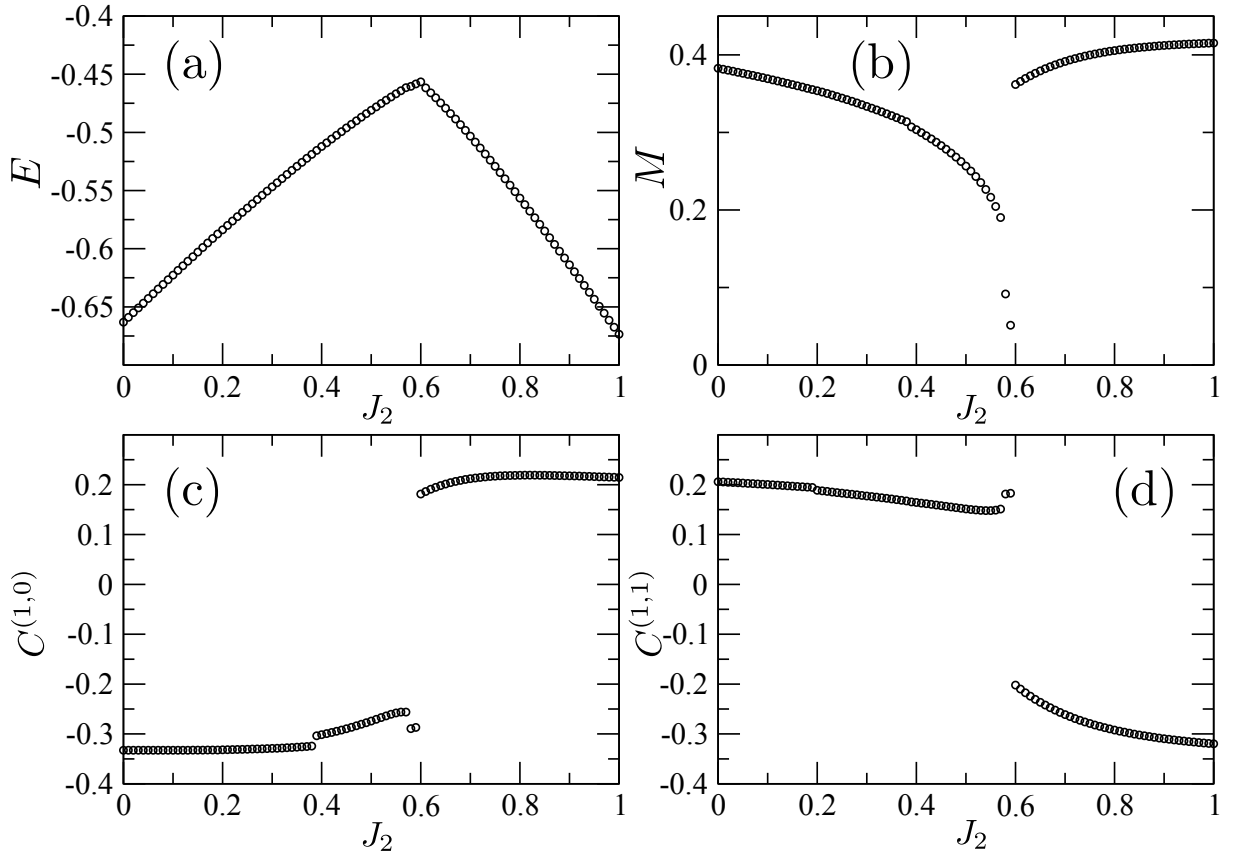
Figure 5.6: Ground state properties of the $J_1 - J_2$ model obtained by means of finite-range MERA presented in Fig. 5.4. (a) energy per lattice site; (b) magnetization: $M = ((M^x)^2 + (M^y)^2 + (M^z)^2)^{1/2}$, (c) correlations between nearest horizontal neighbors given by Eq. (5.5), and (d) next-nearest neighbors correlations given by Eq. (5.6).

It needs pointing out that not every MERA scheme is suitable for characterizing Néel (collinear) order. For instance, both schemes used in Chapter 4 require further modification since, in every decimation step, they group a $3 \times 3$ plaquette into one effective spin. For this reason, one should replace such a translationally invariant scheme by one that in every layer is split into two sublayers of tensors.

Finite-range MERA is designed to be a simple tool for obtaining the phase diagram of a given model at a relatively low cost. Information about a possible order allows to develop a more specialized scheme in order to enhance accuracy. We expect that the near critical points accuracy of finite-range MERA may be lower, therefore, we employ the following technique of investigating the phase diagram. We start with getting the ground state in one point in each known phase, e.g. at $J_2 = 0$, $J_2 = 0.5$ and $J_2 = 1$. From these points we scan the entire diagram: for small $\Delta J_2$, we calculate the ground state in $J_2 + \Delta J_2$ taking a starting point previously computed state at $J_2$. This method is fast and reliable provided that the critical points are not crossed. That is why we handle separate calculations for each phase. Fig. 5.6 presents preliminary results.

In accordance with the previously provided results, energy per lattice site grows while $J_2$ approaches point 0.6 from both sides, i.e. ground state become more frustrated

(Fig. 5.6(a)). Panels (c) and (d) present correlations between nearest (horizontally) and next-nearest neighbors on a lattice which are given by:

$$C^{(1,0)} = \langle \mathbf{S}_{(a,b)} \cdot \mathbf{S}_{(a+1,b)} \rangle, \tag{5.5}$$

$$C^{(1,1)} = \langle \mathbf{S}_{(a,b)} \cdot \mathbf{S}_{(a+1,b+1)} \rangle. \tag{5.6}$$

It can be seen that MERA predicts a correct ground state order: In the regime $J_2 \in [0, 0.6)$: Néel order ($C^{(1,0)} < 0$ and $C^{(1,1)} > 0$) and analogously collinear in $J_2 \in (0.6, 1]$. At present however, the phase obtained at $J_2 \in (0.4, 0.6)$ is incorrect (magnetization in panel (b)).

Table 5.1 summarizes the results in the collinear phase for $J_2 = 1$. Here we compare ground state energies for both applied schemes with different dimensions $m_1$ and $m_2$. These results prove that the extended scheme in Fig. 5.4(b) significantly outperforms the basic one. It is sufficient to increase dimension $m_1$ up to 3 to obtain better energy per lattice site. Further improvements are achieved in higher dimensions $m_1$ and $m_2$.

Table 5.1: Results for the collinear phase for $J_2 = 1$ derived by means of two finite-range MERA schemes in Fig. 5.4: in the first row, the results are calculated using basic scheme, the rest – using the enhanced one.

| dimensions $(m_1, m_2)$ | energy per site $E$ | correlator $C^{(1,0)}$ | correlator $C^{(1,1)}$ |
|---|---|---|---|
| $(2,2)$ | $-0.6745312$ | $0.2193617$ | $-0.3189142$ |
| $(3,2)$ | $-0.6827038$ | $0.2093609$ | $-0.3202768$ |
| $(3,3)$ | $-0.6834429$ | $0.2107143$ | $-0.3208897$ |
| $(4,2)$ | $-0.6849389$ | $0.2089632$ | $-0.3149432$ |

Work in progress includes: (i) The application of the extended scheme to phase $J_2 \in (0.4, 0.6)$ in order to learn more about its structure. This is helpful in designing more suitable MERA schemes for this particular phase. (ii) As the computational cost of investigating the system with next-next-nearest neighbors scales in the same way, we aim at studying the phase diagram of the $J_1 - J_2 - J_3$ model. (iii) The enhancement of computation power of the algorithm to extend the first layer of disentanglers to even larger spin blocks. This can be achieved from both programing as well as purely algorithmical points of view. Details can be found in [8].

## 5.2  Fermions in a non-abelian gauge field

In this section, we consider spin-$\frac{1}{2}$ fermions on an arbitrary lattice, given by Hamiltonian

$$\mathcal{H} = -t \sum_{\langle i,j \rangle} \sum_{\alpha,\beta=0,1} u^{ij}_{\alpha\beta} c^{\dagger}_{\alpha i} c_{\beta j} + U \sum_i n_{0i} n_{1i} . \tag{5.7}$$

Here, $c_{\alpha i}$ is a fermionic annihilation operator at site $i$ and internal state $\alpha \in \{0, 1\}$ in the computational basis. $n_{\alpha i} = c^{\dagger}_{\alpha i} c_{\alpha i}$ denotes a number of fermions in state $\alpha$ at site $i$.

$t$ is a hopping rate between nearest neighbor sites of a lattice, and $U$ is on-site interaction strength. Matrix $u^{ij}$ is a unitary transformation. Matrix $u^{ij}$ can be parametrized by

$$u^{ij} = \exp\left(i\vec{\phi}_{ij}\vec{\tau}\right) , \tag{5.8}$$

where $\vec{\phi}_{ij} = (\phi_{ij}^x, \phi_{ij}^y, \phi_{ij}^z)$ is a real vector, and $\vec{\tau} = (\tau^x, \tau^y, \tau^z)$ is a vector of Pauli matrices in the Hilbert space of internal states $\alpha \in \{0, 1\}$. For Hamiltonian Eq. (5.7) to be Hermitian, it is sufficient to assume $u^{ji} = (u^{ij})^\dagger$ or, equivalently, $\vec{\phi}_{ji} = -\vec{\phi}_{ij}$.

We assume here that the number of fermions is equal to the number of lattice sites and, moreover, we take the strong interaction limit of $U \gg t$. The interaction $U$-term has a degenerate zero energy subspace of states where no site is occupied by 2 fermions. This subspace is separated from states with double occupations by an energy gap of $U$. The matrix elements of the hopping term in the degenerate subspace are zero. To obtain a non-zero effective Hamiltonian in the degenerate subspace, we have to go to the second order in perturbative expansion. For instance, when $\vec{\phi}_{ij} = (\phi^x, 0, 0)$, then we obtain an effective Hamiltonian $\mathcal{H}_{i,j}^{\text{eff}}$ given by

$$\mathcal{H}_{ij}^{\text{eff}}(\phi_x, 0, 0) = \frac{t^2}{U}\left[-1 + \sigma_i^x \sigma_j^x + \right.$$
$$\left. (\sigma_i^y \sigma_j^y + \sigma_i^z \sigma_j^z)\cos 2\phi_x + \frac{1}{2}(\sigma_i^y \sigma_j^z - \sigma_i^z \sigma_j^y)\sin 2\phi_x\right] . \tag{5.9}$$

Here the Pauli operators represent fermionic operators

$$\sigma_i^x = c_i^{0\dagger} c_i^1 + c_i^{1\dagger} c_i^0 ,$$
$$\sigma_i^y = i\left(c_i^{0\dagger} c_i^1 - c_i^{1\dagger} c_i^0\right) ,$$
$$\sigma_i^z = n_{1i} - n_{0i} . \tag{5.10}$$

This effective Hamiltonian describes an interaction between two effective spins $\frac{1}{2}$ at nearest neighbor sites $\langle i, j \rangle$.

In a similar way we obtain

$$\mathcal{H}_{ij}^{\text{eff}}(0, \phi_y, 0) = \frac{t^2}{U}\left[-1 + \sigma_i^y \sigma_j^y + \right.$$
$$\left. (\sigma_i^z \sigma_j^z + \sigma_i^x \sigma_j^x)\cos 2\phi_y + \frac{1}{2}(\sigma_i^z \sigma_j^x - \sigma_i^x \sigma_j^z)\sin 2\phi_y\right] , \tag{5.11}$$

$$\mathcal{H}_{ij}^{\text{eff}}(0, 0, \phi_z) = \frac{t^2}{U}\left[-1 + \sigma_i^z \sigma_j^z + \right.$$
$$\left. (\sigma_i^x \sigma_j^x + \sigma_i^y \sigma_j^y)\cos 2\phi_z + \frac{1}{2}(\sigma_i^x \sigma_j^y - \sigma_i^y \sigma_j^x)\sin 2\phi_z\right] . \tag{5.12}$$

Let us now assume an infinite, two-dimensional square lattice. We take $\vec{\phi}_{ij} = (\phi_x, 0, 0)$ on horizontal links $\langle i, j \rangle$ and $\vec{\phi}_{ij} = (0, \phi_y, 0)$ on vertical ones. Effective Hamiltonian in this case reads:

$$\mathcal{H}^{\text{eff}} = \sum_{a,b}\left[\mathcal{H}_{(a,b),(a+1,b)}^{\text{eff}}(\phi_x, 0, 0) + \mathcal{H}_{(a,b),(a,b+1)}^{\text{eff}}(0, \phi_y, 0)\right] , \tag{5.13}$$
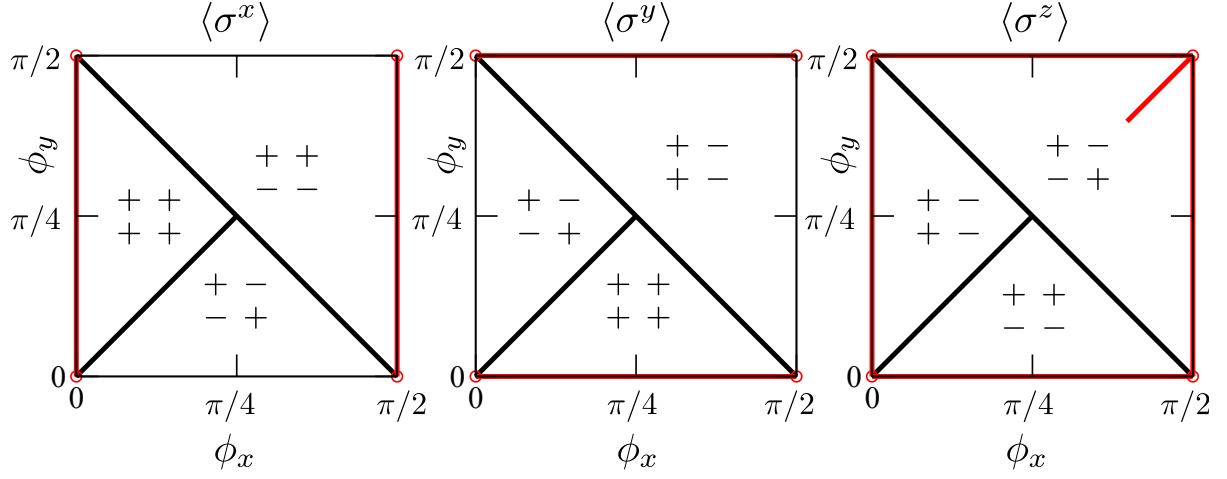
Figure 5.7: Phase diagram obtained from coupled $2 \times 2$ plaquettes. The diagram is symmetric under transformations: $(\phi^x, \phi^y) \to (\phi^x, \pi - \phi^y)$, $(\phi^x, \phi^y) \to (\pi - \phi^x, \phi^y)$ and $(\phi^x, \phi^y) \to (\pi - \phi^x, \pi - \phi^y)$. $\begin{smallmatrix} + & + \\ + & + \end{smallmatrix}$ denotes ferromagnetic phase; $\begin{smallmatrix} + & - \\ - & + \end{smallmatrix}$ – antiferromagnetic; $\begin{smallmatrix} + & + \\ - & - \end{smallmatrix}$ – collinear-$h$; $\begin{smallmatrix} + & - \\ + & - \end{smallmatrix}$ – collinear-$v$, red lines denote magnetization equaling zero. $\pm$ signs represent positive (negative) values of a given component of magnetization. In each phase, the ground state is (at least) two-fold degenerate. E.g. mean-field calculation gives $\begin{smallmatrix} + & + \\ - & - \end{smallmatrix}$ or $\begin{smallmatrix} - & - \\ + & + \end{smallmatrix}$ depending on initial (random) conditions. The diagram is partially confirmed by $4 \times 4$ coupled clusters. Away from phase boundaries, the order is the same as shown above. However, we do not exclude the possibility that the near boundaries phase order may vary.

where $\mathcal{H}^{\text{eff}}_{(a,b),(a+1,b)}$ and $\mathcal{H}^{\text{eff}}_{(a,b),(a,b+1)}$ are given by Eqs. (5.9) and (5.11), respectively.

Notice first that line $\phi_x = \phi_y$ is a symmetry axis of the system. Corresponding transformation reads:

$$
\begin{aligned}
i &\longleftrightarrow j, \\
\phi_x &\longleftrightarrow \phi_y, \\
\sigma^x &\longleftrightarrow \sigma^y, \\
\sigma^z &\longleftrightarrow -\sigma^z.
\end{aligned}
\tag{5.14}
$$

We begin analyzing the ground state of Hamiltonian (5.13) by studying its phase diagram in parameters $(\phi_x, \phi_y)$. To this end, as a first approximation, we assume that the ground state is a product of $L \times L$ plaquettes that are coupled with the neighboring sites by mean-field terms. Because of the antiferromagnetic order in some regime of $(\phi_x, \phi_y)$, odd values of $L$ are excluded. Thus, the calculations are performed for $L = 2$ and $L = 4$. Fig. 5.7 shows the phase diagram. Diagram is rich: it is split into three parts – each part represents an order of a given component of magnetization. We encounter ferromagnetic and antiferromagnetic order as well as collinear one. Notice that there is the symmetry between $x$ and $y$ component of magnetization whereas the order of the $z$ component is different. This behavior could be expected from the form of effective Hamiltonians Eqs. (5.9) and (5.11).

Observe that the $z$ component of magnetization equals zero on a segment which starts
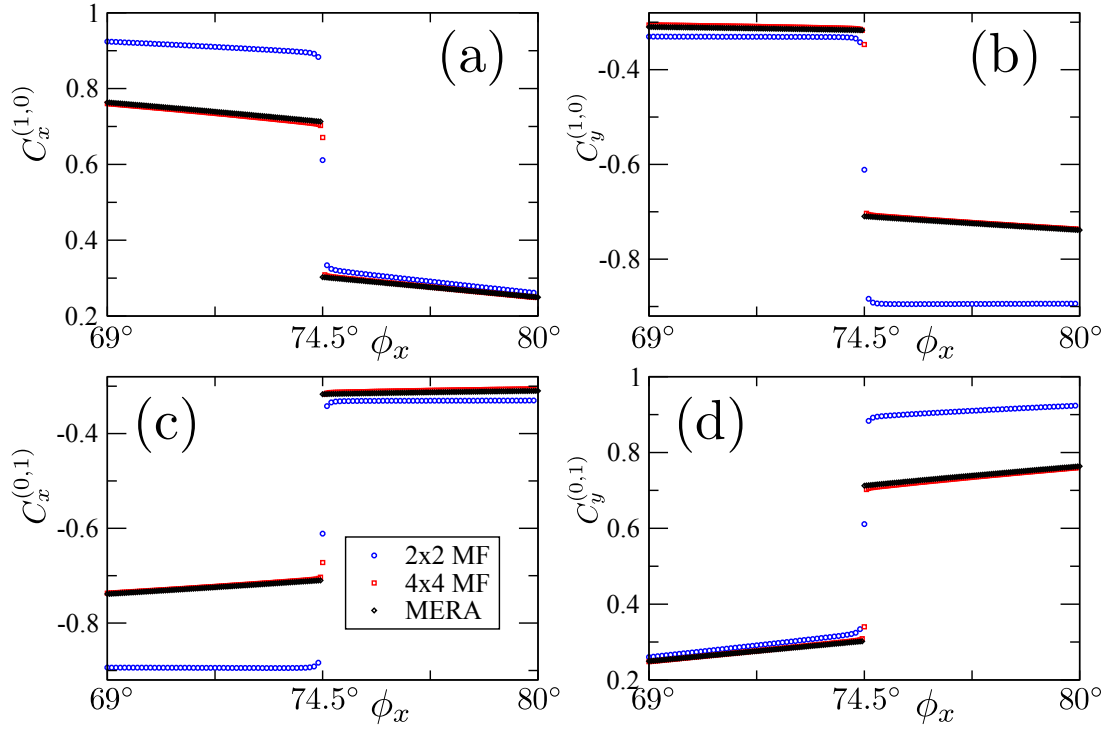
Figure 5.8: A perpendicular cross through a segment with $\langle \sigma^z \rangle = 0$ presented in phase diagram Fig. 5.7 at point $\phi_x = \phi_y = 74.5°$. (a), (b) correlations between nearest horizontal neighbors on a lattice in the $x$ and $y$ components, respectively. $C_x^{(1,0)}$ and $C_y^{1,0}$ are given by Eq. (5.15). (c), (d) analogous correlations between vertical neighbors. $C_x^{(0,1)}$ and $C_y^{0,1}$ are given by Eq. (5.16). The Panels present results obtained by means of $2 \times 2$, $4 \times 4$ coupled clusters as well as finite-range MERA (Fig. 5.4(a)). Points acquired from $4 \times 4$ coupled clusters and finite-range MERA almost coincide.

at $\phi_x = \phi_y \simeq 71.3°$ and ends in $\phi_x = \phi_y = \pi/2$. An interesting question arises: whether this behavior is physical and hence leads to an unusual phase transition or it is an artifact of mean-field approximation.

To answer the above question, we firstly apply finite-range MERA described at the beginning of this chapter to see whether the order of phases in the neighborhood of the segment predicted by mean-field calculations are confirmed also by finite-range MERA. Information about the nature of the ground state can be used to propose a more suitable scheme for investigating the possible quantum phase transitions at line $\phi_x = \phi_y$.

To this end, we obtain the ground state for $(\phi_x, \phi_y)$ on line that is perpendicular to line $\phi_x = \phi_y$ and crosses the segment. One such line is chosen: $\phi_y = 149° - \phi_x$, i.e. the line crosses the segment at $\phi_x = \phi_y = 74.5°$.

Because of the possible phase transition, we employ a technique of scanning with MERA described in the previous section. This time we handle two separate calculations starting from points to the left and to the right from the segment. Fig. 5.8 summarizes the results derived by means of $2 \times 2$ and $4 \times 4$ coupled clusters as well as from finite-range MERA. Correlations presented in different panels of this figure are given by:

$$C_x^{(1,0)} \quad = \quad \left\langle \sigma_{(a,b)}^x \; \sigma_{(a+1,b)}^x \right\rangle, \quad C_y^{(1,0)} \quad = \quad \left\langle \sigma_{(a,b)}^y \; \sigma_{(a+1,b)}^y \right\rangle, \qquad (5.15)$$

$$C_x^{(0,1)} \quad = \quad \left\langle \sigma_{(a,b)}^x \; \sigma_{(a,b+1)}^x \right\rangle, \quad C_y^{(0,1)} \quad = \quad \left\langle \sigma_{(a,b)}^y \; \sigma_{(a,b+1)}^y \right\rangle. \qquad (5.16)$$

It turns out that finite-range MERA breaks symmetry of Eq. (5.14) and produces an asymmetric solution. This may be due to initialization of the algorithm from random values that prefers one particular direction ($x$ or $y$). At present, we are working on incorporating this symmetry into the existing MERA algorithm to overcome this problem.

Apart from these difficulties, we can employ transformation (5.14) to the obtained solution and restore the symmetry in the following way: Having two solutions (from MERA and the transformed one), we compare their energies at each point $(\phi_x, \phi_y)$ and select a solution with lower energy. Fig. 5.9 depicts both of them. For $\phi_x > 74.5°$, the solution due to MERA has lower energy whereas for $\phi_x < 74.5°$ – the one transformed by means of Eq. (5.14). Black points in Fig. 5.8 illustrate the results from finite-range MERA with restored symmetry obtained by this method.



Figure 5.9: MERA solution undergoes symmetry transformation (5.14). The transformed solution (tMERA) has lower energy for $\phi < 74.5°$. The results presented in Fig. 5.8 are derived from a proper joining of these two solutions.

Preliminary results from finite-range MERA (basic scheme) confirm the pattern of bonds found by $2 \times 2$ and $4 \times 4$ coupled clusters for the $x$ and $y$ components of magnetization.

The $z$ component (not shown) tends to zero not only on line $\phi_x = \phi_y$ but also on its neighborhood. This conclusion is drawn on the basis of the results from $4 \times 4$ clusters and finite-range MERA in Fig. 5.4 and requires further investigation.

Work in progress [7] involves designing more suitable MERA scheme for closer investigation of this region of the diagram as well as obtaining more reliable results by means of enhanced finite-range MERA in Fig. 5.4.
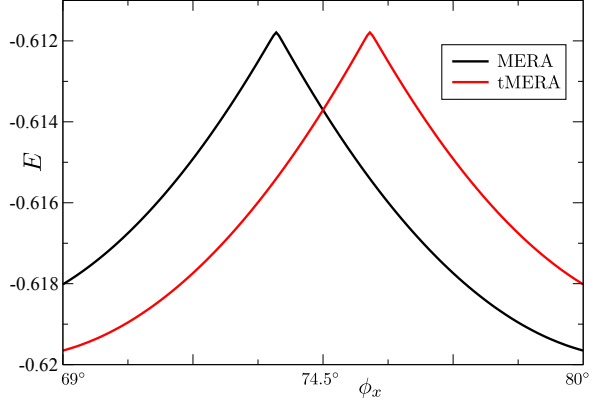
# Conclusions and outlook

In this Dissertation, we have developed and applied the MERA algorithms to various physical systems. Both, an intuitive view of the subject as well as a range of technical details have been provided and exhaustively discussed. Chapter 3 presents the very first approach to two-dimensional systems by means of entanglement renormalization techniques. In Chapter 5, as a part of the ongoing research, we give examples of MERA applications to the frustrated quantum models. MERA is a flexible tool which can be adapted in a straightforward way to frustrated systems. Thanks to its unique properties, various realization of frustrating interactions between even distant sites of a given lattice can be investigated.

In the near future, we intend to further develop the MERA algorithms in two directions: (i) exploiting the internal symmetries of the state being described and (ii) enhancing the computational power of the algorithms using the advanced Monte Carlo sampling techniques.

As we have seen in Chapter 3, due to the particular tensor structure, MERA can reflect the symmetries of the underlying quantum state, i.e. if it is known that a quantum state in question must satisfy certain symmetry properties, then this information can be used to make the algorithm more efficient. These simplifications are helpful in turning difficult problems into more accessible ones. We aim at pushing further the ideas outlined in Chapter 3 and developing new versions of the algorithms which would suit best in a given physical situation in the presence of the symmetries.

On the other hand, in the most general setting (or without any additional knowledge), computations within the MERA algorithm might become complex and time-consuming. One way to overcome this difficulty would be to perform calculations within MERA in an approximate way by means of the Monte Carlo sampling methods. This novel approach can provide a significant progress and it certainly opens new areas of possible applications of the MERA algorithm.

# Appendix A

# Spin wave expansion for the generalized compass model

In this Appendix, we present details of the spin-wave calculation for the generalized compass model and compare the results with the ones obtained by means of MERA in Chapter 4. We consider here the general case of an $L \times L$ square lattice, with $L$ being odd for convenience. Before comparison is drawn, we take thermodynamic limit $L \to \infty$ in these calculations.

Since the spin-wave expansion in powers of $1/S$ becomes exact when the spin $S \to \infty$, we introduce a large-$S$ extension of the generalized OCM Hamiltonian Eq. (4.1) with rescaled spin operators: $\sigma^x \to S^x/S$ and $\sigma^z \to S^z/S$. We consider first the classical energy per site:

$$E_0(\theta, \phi) \equiv \langle \mathcal{H}(\theta) \rangle_\phi = -\frac{1}{2} \left[ 1 + \cos\theta \cos(2\phi) \right] , \tag{A.1}$$

obtained using the mean-field (MF) for the ordered state of classical spins $\vec{S}$, with the magnetization direction given by Eq. (4.18). The classical energy has a minimum at $\phi = 0$ for the entire range of $\theta \in [0°, 90°)$. However, when angle $\theta$ approaches $90°$, the minimum becomes more and more shallow, and finally disappears completely at $\theta = 90°$. Thus, the classical ground state becomes very sensitive to quantum fluctuations in the vicinity of the maximally frustrated interactions in the OCM.



Figure A.1: Mechanism of the QPT in the generalized OCM Eq. (1) for $S = 1/2$ and $\theta = 87° > \theta_c$. The minimum of classical energy $E_0(87°, \phi)$ Eq. (A.1) (dashed line) at $\phi = 0$ is shallow and thus unstable against weak quantum fluctuations which induce two symmetric minima at a finite value of $\pm\phi_{\min}$ obtained from $E_6(87°, \phi)$ derived from Eq. (A.4). For better comparison, $E_0$ and $E_6$ are shifted to have a minimum value of 0.

This behavior of the classical ground state energy provides an explanation of why small energy contributions due to quantum fluctuations may play such a crucial role in the generalized OCM only in the regime of $\theta$, close to $90°$, where they trigger a QPT by splitting the shallow symmetric classical energy minimum at $\phi = 0$ into two symmetry-broken minima at finite values $\pm\phi_{\min}$ – we show an example of this behavior in Fig. A.1
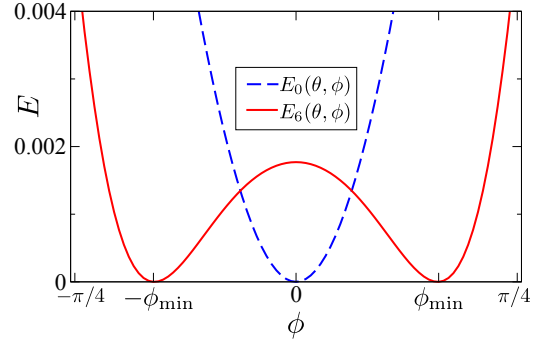
for a particular value of $\theta > \theta_c$. Since here the quantum fluctuations induce the symmetry breaking instead of making the ground state more symmetric, this mechanism goes beyond the Landau functional paradigm.

We analyze the effects of quantum fluctuations and the arising symmetry breaking using the Holstein-Primakoff representation of spin $\{S_{ij}^\alpha\}$ operators via $\{b_{ij}\}$ bosons:

$$\cos\phi \ S_{ij}^x + \sin\phi \ S_{ij}^z \ = \ S - b_{ij}^\dagger b_{ij}\,, \tag{A.2}$$

$$-\sin\phi \ S_{ij}^x + \cos\phi \ S_{ij}^z \ = \ \frac{b_{ij}^\dagger}{2}\sqrt{2S - b_{ij}^\dagger b_{ij}} + \text{H.c.}\,. \tag{A.3}$$

Operators $\{b_{ij}, b_{ij}^\dagger\}$ satisfy standard bosonic commutation relations: $[b_{ij}, b_{i'j'}] = 0$ and $[b_{ij}, b_{i'j'}^\dagger] = \delta_{ii'}\delta_{jj'}$. In this approach, we look for a critical value $\theta_c$, above which it is energetically favorable to change the direction of magnetization $\mathbf{M}$ from symmetric state $\phi = 0$ to a symmetry-broken state with a finite value of $\phi \neq 0$. We expand the square root in Eq. (A.3) in powers of $1/(2S)$ and obtain an expansion of Hamiltonian Eq. (4.1) in powers of operators $\{b_{ij}, b_{ij}^\dagger\}$. As we apply Wick's theorem to reduce the obtained Hamiltonian to an effective quadratic Hamiltonian, the terms proportional to the odd powers of $1/(2S)$ do not contribute and are skipped below. When truncated at the sixth order term, this expansion reads

$$\widetilde{H}_6 \simeq H_0 + (2S)^{-1}H_2 + (2S)^{-2}H_4 + (2S)^{-3}H_6\,. \tag{A.4}$$

Here, $H_{2n}$ is a sum of all terms of the $2n$-th order in the $\{b_{ij}, b_{ij}^\dagger\}$ operators. In a similar way, $\widetilde{H}_4$ and $\widetilde{H}_2$ denote expansions truncated at the fourth and second order terms, respectively. We find a posteriori that the second order expansion $\widetilde{H}_2$ (non-interacting spin waves) does not suffice and higher order terms are necessary. Consequently, we consider below Hamiltonian Eq. (4.1) expanded up to the sixth order.

For given $\theta$ and $\phi$, the ground state of the boson Hamiltonian Eq. (A.4) is approximated by a Bogoliubov vacuum obtained as the ground state of a mean-field quadratic Hamiltonian $\widetilde{H}_2^{\text{MF}}$ (to be derived later on). Terms $H_2$, $H_4$ and $H_6$ in Eq. (A.4) are given by:

$$\begin{aligned}
H_2 \ = \ & 4[1 + \cos\theta\cos(2\phi)]\sum_\mathbf{r} b_\mathbf{r}^\dagger b_\mathbf{r} - \\
& \sin^2\left(\phi - \frac{\theta}{2}\right)\sum_\mathbf{r}\left(b_\mathbf{r}^\dagger b_{\mathbf{r}+\mathbf{e_x}} + b_\mathbf{r} b_{\mathbf{r}+\mathbf{e_x}} + \text{H.c.}\right) - \\
& \sin^2\left(\phi + \frac{\theta}{2}\right)\sum_\mathbf{r}\left(b_\mathbf{r}^\dagger b_{\mathbf{r}+\mathbf{e_y}} + b_\mathbf{r} b_{\mathbf{r}+\mathbf{e_y}} + \text{H.c.}\right)\,, \tag{A.5}
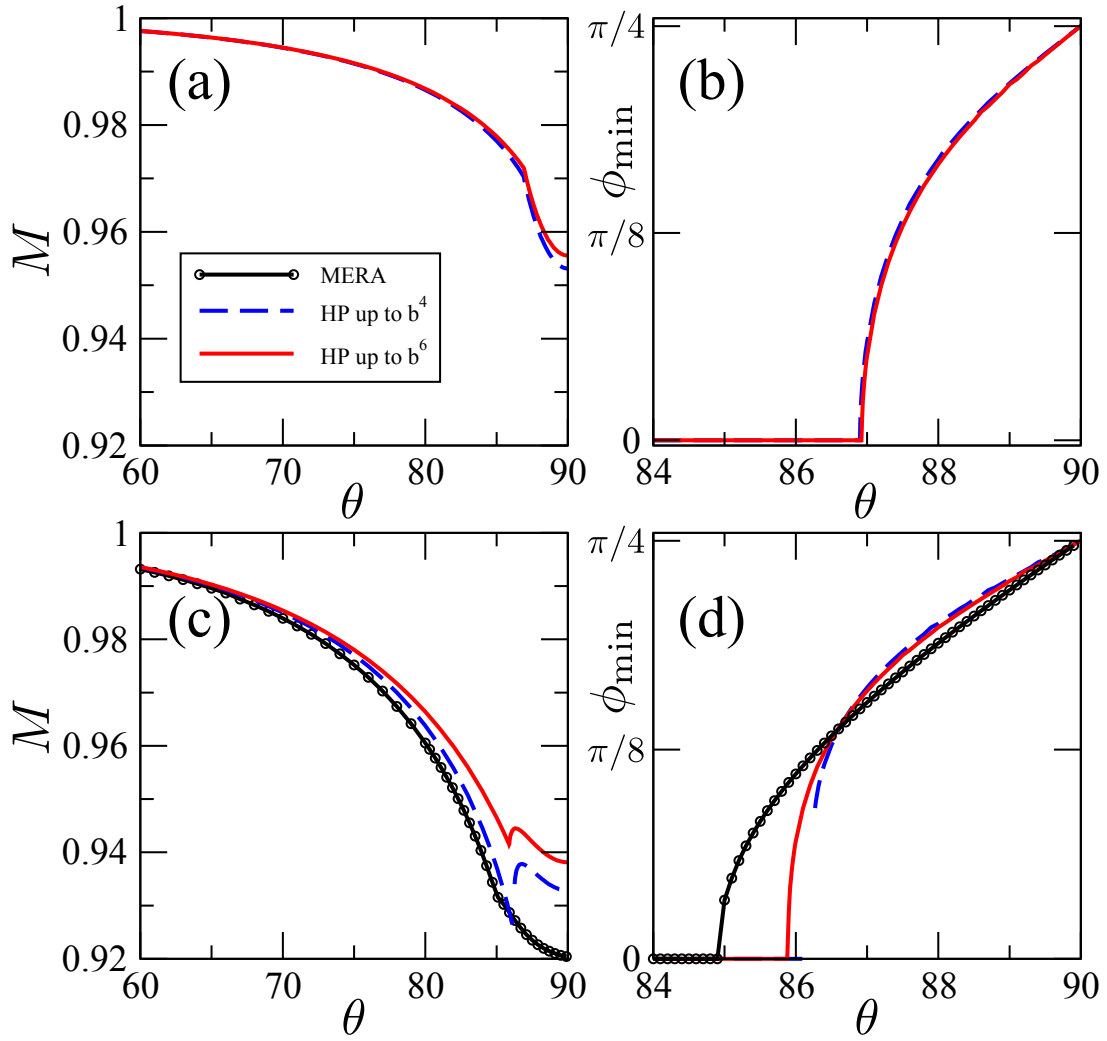\end{aligned}$$

Figure A.2: Symmetry breaking in the ground state as obtained from the boson expansion Eq. (A.4). Panels (a) and (b) show results for $S = 1$, (c) and (d) – for $S = 1/2$; (a) and (c) depict magnetization $M$ Eq. (4.17), (b) and (d) – the value of magnetization angle $\phi$ Eq. (4.18) that minimizes energy. Calculations for $\widetilde{H}_6$ predict the following values of $\theta_c$: $85.89°$, $86.9°$, $88.2°$, and $89.2°$ for $S = 1/2$, $S = 1$, $S = 2$, and $S = 5$, respectively (the last two not presented), and $\theta_c \to 90°$ for $S \to \infty$.

$$
\begin{aligned}
H_4 &= -4\cos^2\left(\phi - \frac{\theta}{2}\right) \sum_{\mathbf{r}} b_{\mathbf{r}}^{\dagger} b_{\mathbf{r}+\mathbf{e_x}}^{\dagger} b_{\mathbf{r}} b_{\mathbf{r}+\mathbf{e_x}} - \\
&\quad 4\cos^2\left(\phi + \frac{\theta}{2}\right) \sum_{\mathbf{r}} b_{\mathbf{r}}^{\dagger} b_{\mathbf{r}+\mathbf{e_y}}^{\dagger} b_{\mathbf{r}} b_{\mathbf{r}+\mathbf{e_y}} + \\
&\quad \frac{1}{2}\sin^2\left(\phi - \frac{\theta}{2}\right) \sum_{\mathbf{r}} \left\{ b_{\mathbf{r}}^{\dagger} b_{\mathbf{r}}^{2} (b_{\mathbf{r}+\mathbf{e_x}} + b_{\mathbf{r}-\mathbf{e_x}} + b_{\mathbf{r}+\mathbf{e_x}}^{\dagger} + b_{\mathbf{r}-\mathbf{e_x}}^{\dagger}) + \text{H.c.} \right\} + \\
&\quad \frac{1}{2}\sin^2\left(\phi + \frac{\theta}{2}\right) \sum_{\mathbf{r}} \left\{ b_{\mathbf{r}}^{\dagger} b_{\mathbf{r}}^{2} (b_{\mathbf{r}+\mathbf{e_y}} + b_{\mathbf{r}-\mathbf{e_y}} + b_{\mathbf{r}+\mathbf{e_y}}^{\dagger} + b_{\mathbf{r}-\mathbf{e_y}}^{\dagger}) + \text{H.c.} \right\}, \quad \text{(A.6)}
\end{aligned}
$$

63

and

$$
\begin{aligned}
H_6 \;=\; & \frac{1}{8}\sin^2\left(\phi-\frac{\theta}{2}\right)\sum_{\mathbf{r}}\Big\{\left(b_{\mathbf{r}}^{\dagger}b_{\mathbf{r}}\right)^2 b_{\mathbf{r}}(b_{\mathbf{r}+\mathbf{e_x}}+b_{\mathbf{r}-\mathbf{e_x}}+b_{\mathbf{r}+\mathbf{e_x}}^{\dagger}+b_{\mathbf{r}-\mathbf{e_x}}^{\dagger})- \\
& 2 b_{\mathbf{r}}^{\dagger}b_{\mathbf{r}+\mathbf{e_x}}^{\dagger}b_{\mathbf{r}}^2(b_{\mathbf{r}+\mathbf{e_x}}+b_{\mathbf{r}+\mathbf{e_x}}^{\dagger})b_{\mathbf{r}+\mathbf{e_x}}+\text{H.c.}\Big\}+ \\
& \frac{1}{8}\sin^2\left(\phi+\frac{\theta}{2}\right)\sum_{\mathbf{r}}\Big\{\left(b_{\mathbf{r}}^{\dagger}b_{\mathbf{r}}\right)^2 b_{\mathbf{r}}(b_{\mathbf{r}+\mathbf{e_y}}+b_{\mathbf{r}-\mathbf{e_y}}+b_{\mathbf{r}+\mathbf{e_y}}^{\dagger}+b_{\mathbf{r}-\mathbf{e_y}}^{\dagger})- \\
& 2 b_{\mathbf{r}}^{\dagger}b_{\mathbf{r}+\mathbf{e_y}}^{\dagger}b_{\mathbf{r}}^2(b_{\mathbf{r}+\mathbf{e_y}}+b_{\mathbf{r}+\mathbf{e_y}}^{\dagger})b_{\mathbf{r}+\mathbf{e_y}}+\text{H.c.}\Big\},
\end{aligned}
\tag{A.7}
$$

where $\mathbf{r}=(i,j)$, $\mathbf{e_x}=(1,0)$ and $\mathbf{e_y}=(0,1)$.

In order to derive quadratic approximation $\widetilde{H}_2^{\mathrm{MF}}$, we replace the boson terms in $H_4$ and $H_6$ with two-boson terms and proper averages by means of the MF approximation and Wick's theorem. This justifies a posteriori why the (A.4) expansion is limited only to the terms with an even number of boson operators. As an example of this approximation, consider one of the contributions to $H_4$ in Eq. (A.6): $b_{\mathbf{r}}^{\dagger}b_{\mathbf{r}}^2 b_{\mathbf{r}+\mathbf{e_x}}$, which is replaced with a quadratic term:

$$
\begin{aligned}
b_{\mathbf{r}}^{\dagger}b_{\mathbf{r}}^2 b_{\mathbf{r}+\mathbf{e_x}} \;\simeq\;& 2\langle b_{\mathbf{r}}^{\dagger}b_{\mathbf{r}}\rangle\, b_{\mathbf{r}}b_{\mathbf{r}+\mathbf{e_x}}+2\langle b_{\mathbf{r}}b_{\mathbf{r}+\mathbf{e_x}}\rangle\, b_{\mathbf{r}}^{\dagger}b_{\mathbf{r}}+ \\
& \langle b_{\mathbf{r}}^{\dagger}b_{\mathbf{r}+\mathbf{e_x}}\rangle\, b_{\mathbf{r}}^2+\langle b_{\mathbf{r}}^2\rangle\, b_{\mathbf{r}}^{\dagger}b_{\mathbf{r}+\mathbf{e_x}}-\langle b_{\mathbf{r}}^{\dagger}b_{\mathbf{r}}^2 b_{\mathbf{r}+\mathbf{e_x}}\rangle\,.
\end{aligned}
\tag{A.8}
$$

The above replacement procedure leads to six MF parameters $\{m_i\}_{i=1}^6$ that should satisfy self-consistency conditions. These are in fact all possible combinations of operators defined on nearest-neighbor sites that cannot be derived one from another by commutation relations and translational invariance of the lattice, i.e. $m_1=\langle b_{\mathbf{r}}^{\dagger}b_{\mathbf{r}}\rangle$, $m_2=\langle b_{\mathbf{r}}^{\dagger}b_{\mathbf{r}+\mathbf{e_x}}\rangle$, $m_3=\langle b_{\mathbf{r}}^{\dagger}b_{\mathbf{r}+\mathbf{e_y}}\rangle$, $m_4=\langle b_{\mathbf{r}}^2\rangle$, $m_5=\langle b_{\mathbf{r}}b_{\mathbf{r}+\mathbf{e_x}}\rangle$, and $m_6=\langle b_{\mathbf{r}}b_{\mathbf{r}+\mathbf{e_y}}\rangle$.

The obtained Hamiltonian $\widetilde{H}_2^{\mathrm{MF}}$ is diagonalized by the Fourier transformation followed by the Bogoliubov transformation. The Fourier transformation which is consistent with periodic boundary conditions $b_{L+1,j}=b_{1,j}$ and $b_{i,L+1}=b_{i,1}$ takes the following form:

$$
b_{\mathbf{r}} \;=\; \frac{1}{L}\sum_{\mathbf{k}}b_{\mathbf{k}}\,e^{i\mathbf{k}\cdot\mathbf{r}},
\tag{A.9}
$$

where $\mathbf{k}=(k_x,k_y)$ is the momentum. In the above sum, momentum components $k_x$ and $k_y$ take the values (for odd $L$ considered here):

$$
k_x,k_y \;\in\; \left\{0\cdot\frac{2\pi}{L},\ \pm1\cdot\frac{2\pi}{L},\ \ldots,\ \pm\frac{L-1}{2}\cdot\frac{2\pi}{L}\right\}.
\tag{A.10}
$$

Diagonalization of $\widetilde{H}_2^{\mathrm{MF}}$ is completed by the Bogoliubov transformation:

$$
b_{\mathbf{k}} \;=\; u_{\mathbf{k}}\gamma_{\mathbf{k}}+v_{-\mathbf{k}}^{*}\gamma_{-\mathbf{k}}^{\dagger},
\tag{A.11}
$$

where modes $u_{\mathbf{k}}$ and $v_{\mathbf{k}}$ are normalized such that $|u_{\mathbf{k}}|^2-|v_{\mathbf{k}}|^2=1$. The obtained modes are used to calculate new values of the MF parameters $\{m_i\}_{i=1}^6$. For instance, one of them reads: $m_2=\langle b_{\mathbf{r}}^{\dagger}b_{\mathbf{r}+\mathbf{e_x}}\rangle=\frac{1}{L^2}\sum_{\mathbf{k}}|v_{\mathbf{k}}|^2\cos k_x$. Starting from random values, the above steps are iteratively applied until full convergence of $\{m_i\}_{i=1}^6$ is reached, which results in satisfying the self-consistency conditions.

Firstly, we perform separate calculations for $\widetilde{H}_2$, $\widetilde{H}_4$ and $\widetilde{H}_6$ for several values of spin $S \geq 1$ when the $1/(2S)$-expansion given in Eq. (A.4) is convergent. Quadratic $\widetilde{H}_2$ fails for large $\theta$, where Bogoliubov frequencies become non-real and magnetization $M$ Eq. (4.17) diverges. In contrast, $\widetilde{H}_4$ and $\widetilde{H}_6$ give only small reduction in $M$ in the entire range of $\theta$, see Fig. A.2(a) and A.2(c). Interestingly, the Bogoliubov spectrum remains gapful at $\theta_c$ in both the fourth and sixth order expansions and, just like in MERA, there are no algebraically decaying spin-spin correlations. Critical angle $\theta_c$ at which the symmetry-breaking QPT occurs, increases toward $90°$



Figure A.3: Energy gap calculated within the spin-wave theory. $\widetilde{H}_2$ fails for large $\theta$ while $\widetilde{H}_4$ and $\widetilde{H}_6$ predict gapful spectrum for all values of $\theta$. The minimum is attained at $\theta_c$. Surprisingly, $\Delta(\theta_c) = 1.52 \neq 0$ (calculated using $\widetilde{H}_6$).

with increasing $S$ when the quantum fluctuations become less significant. Therefore, magnetization $M$ increases with increasing $S$ and it tends to 1 in the classical limit $S \to \infty$.

Encouraged by these results, we also perform similar calculations for the generalized OCM, see Eq. (4.1) with $S = 1/2$, where the convergence of the $1/(2S)$-expansion becomes problematic. Unlike for $S \geq 1$, we find that the fourth order expansion is insufficient as it predicts the first order QPT (Fig. A.2(d)) and does not agree qualitatively with the prediction of MERA, see Section 4.4. Only in the sixth order, one finds a qualitative agreement between the present boson expansion and MERA, both giving the second order QPT at $\theta_c$. A cusp in $M(\theta)$ seen in Fig. A.2(c) shows that even the sixth order expansion is not quite converged for $S = 1/2$. Again, the Bogoliubov spectrum remains gapful at $\theta_c$ in the sixth order expansion, with finite gap $\Delta(\theta_c) = 1.52$, as shown in Fig. A.3. No algebraically decaying spin-spin correlations are found.
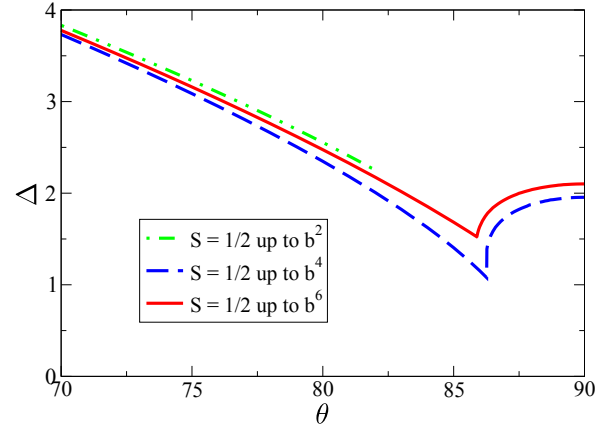
# Bibliography

[1] J. van den Brink, P. Horsch, F. Mack, and A. M. Oleś, Phys. Rev. B **59**, 6795 (1999).

[2] W. Brzezicki, J. Dziarmaga, and A. M. Oleś, Phys. Rev. B **75**, 134415 (2007).

[3] L. Capriotti and S. Sorella, Phys. Rev. Lett. **84**, 3173 (2000).

[4] L. Cincio, J. Dziarmaga, M. M. Rams, and W. H. Zurek, Phys. Rev. A **75**, 052321 (2007).

[5] L. Cincio, J. Dziarmaga, and M. M. Rams, Phys. Rev. Lett. **100**, 240603 (2008).

[6] L. Cincio, J. Dziarmaga, and A. M. Oleś, Phys. Rev. B **82**, 104416 (2010).

[7] L. Cincio, F. M. Cucchietti, J. Dziarmaga, and M. Lewenstein, *in preparation.*

[8] L. Cincio, G. Evenbly, and G. Vidal, *in preparation.*

[9] P. Corboz, G. Evenbly, F. Verstraete, and G. Vidal, Phys. Rev. A, **81**, 010303 (2010).

[10] P. Corboz, G. Vidal, Phys. Rev. B **80**, 165129 (2009).

[11] C. M. Dawson, J. Eisert, and T. J. Osborne, Phys. Rev. Lett. **100**, 130501 (2008).

[12] J. Dorier, F. Becca, and F. Mila, Phys. Rev. B **72**, 024448 (2005).

[13] B. Douçot, M. V. Feigel'man, L. B. Ioffe, and A. S. Ioselevich, Phys. Rev. B **71**, 024505 (2005).

[14] E. Eriksson and H. Johannesson, Phys. Rev. B **79**, 224424 (2009).

[15] G. Evenbly, G. Vidal, Phys. Rev. Lett. **102**, 180406 (2009)

[16] G. Evenbly and G. Vidal, Phys. Rev. B **79**, 144108 (2009).

[17] G. Evenbly, G. Vidal, Phys. Rev. Lett. **104**, 187203 (2010).

[18] L. F. Feiner and A. M. Oleś, Phys. Rev. B **59**, 3295 (1999).

[19] J. Hubbard, Proc. Roy. Soc. (London) A **272**, 238 (1963).

[20] L. P. Kadanov, Physics (Long Island City, N.Y.) **2**, 263 (1966).

[21] D. I. Khomskii and M. V. Mostovoy, J. Phys. A **36**, 9197 (2003).

[22] K. I. Kugel and D. I. Khomskii, Sov. Phys. Usp. **25**, 231 (1982).

[23] P. Milman, W. Maineult, S. Guibal, L. Guidoni, B. Douçot, L. Ioffe, and T. Coudreau, Phys. Rev. Lett **99**, 020503 (2007).

[24] A. Mishra, M. Ma, F.-C. Zhang, S. Guertler, L.-H. Tang, and S. Wan, Phys. Rev. Lett. **93**, 207201 (2004).

[25] Z. Nussinov, M. Biskup, L. Chayes, and J. van den Brink, Europhys. Lett. **67**, 990 (2004).

[26] Z. Nussinov and E. Fradkin, Phys. Rev. B **71**, 195120 (2005).

[27] Z. Nussinov and G. Ortiz, Ann. Phys. (N.Y.) **324**, 977 (2009).

[28] R. Orús, A. C. Doherty, and G. Vidal, Phys. Rev. Lett. **102**, 077203 (2009).

[29] A. W. Sandvik, Phys. Rev. E **68**, 056701 (2003).

[30] O. P. Sushkov, J. Oitmaa, and Z. Weihong , Phys. Rev. B, **63**, 104420 (2001).

[31] G. Vidal, Phys. Rev. Lett. **91**, 147902 (2003).

[32] G. Vidal, Phys. Rev. Lett. **93**, 040502 (2004).

[33] G. Vidal, Phys. Rev. Lett. **98**, 070201 (2007).

[34] G. Vidal, Phys. Rev. Lett. **99**, 220405 (2007).

[35] S. Wenzel and W. Janke, Phys. Rev. B **78**, 064402 (2008).

[36] S. R. White, Phys. Rev. Lett. **69**, 2863 (1992).

[37] K. G. Wilson, Rev. Mod. Phys. **47**, 773 (1975).